Monitoring of deformations and cracks for laser powder bed fusion using gas-borne acoustic emission

Karabo Moore

Dissertation submitted in fulfilment of the
requirements for the degree
Master of Engineering in Mechanical Engineering
in the Department of Mechanical and Mechatronics
Engineering, Faculty of Engineering, Built
Environment and Information Technology at
Central University of Technology, Free State

Supervisor:	**Dr. Dean Kouprianoff, D. Eng.**
Co-supervisors:	**Prof. Ihar Yadroitsau, D. Eng.**
	Prof. Ina Yadroitsava, Ph. D.

Bloemfontein
March 2024

DECLARATION OF INDEPENDENT WORK

I, Karabo Moore, identity number _____________ and student number ________, do hereby declare that this research project submitted to Central University of Technology, Free State, for the Master of Engineering in Mechanical Engineering degree, is my own independent work; and complies with the Code of Academic Integrity, as well as other relevant policies, procedures, rules and regulations of Central University of Technology, Free State; and has not been submitted previously to any institution by myself or any other person in fulfilment of the requirements for the attainment of any qualification.

Signature of student:

Date: 23 March 2024

ACKNOWLEDGEMENTS

Dear Lord, I thank you for the gift of life, as in you We live, We breathe and have Our being.

To my late Father, THANK you for being a Father to me…

I'll forever be Humbled by your Guidance and Teachings.

To my Mother, words cannot even begin to describe
the pillar of strength you are in my life,
as without your Sacrifices, Love, and Care,
this Thesis wouldn't come to life.

To my Sister, You are stronger than you think,
as your belief in me, has always been the fuel I needed.

I would humbly like to thank my supervisors wholeheartedly, as their support, patience and guidance, kept me going through even the toughest of times. To Prof Ina and Prof Igor, it was an honour to work and learn under your guidance, as it has been an experience I'll forever hold and cherish in my life. To Dr Kouprianoff, thank you very much for believing in me, encouraging and motivating me, as your light kept my candle burning all the way. I would also like to gratefully acknowledge the Collaborative Program in Additive Manufacturing (Contract № CSIR-NLC-CPAM-18-MOA-CUT-01) of the Department of Science and Innovation, the South African Research Chairs Initiative of the National Research Foundation of South Africa (Grant № 97994), the Central University of Technology, Free State for the Central Postgraduate Funding Support grant, and CRPM for allowing me to utilise their facilities to complete the work. I would like to end by thanking all my Friends, Family and Colleagues who assisted in their own respective unique ways in the completion of the thesis.

Seek joy, and you'll find peace

Leano la Modimo

ABSTRACT

Additive manufacturing (AM) is a manufacturing technique that involves building parts in a layer-by-layer manner from a computer-aided design model. Laser powder bed fusion (L-PBF) is an AM process that uses metal powders as its manufacturing material where a laser beam is used to melt the powder layer pre-deposited onto the substrate. Solidified single layers form along the laser path resulting in 3D objects being built in a layer-by-layer manner. The quality and resulting material properties of the L-PBF parts depend on many factors, such as the laser parameters, build environment and material properties. Deformation, delaminations and cracks within the material are mainly caused by the residual stresses induced during the L-PBF build process by the rapid heating and cooling cycles.

With the increase in the implementation of AM technology in industry, there has also been a growing need for quality control and assurance measures for the final product. The effective use of modern methods of non-destructive testing (NDT) online monitoring systems, which can detect deformation and delaminations in the L-PBF process, is currently being investigated.

Acoustic emission (AE) is a cost-effective NDT online monitoring method which monitors stress waves propagated by a sudden redistribution of stress in a material. AE has been shown to be effective in monitoring defects such as cracks in pressure vessels and building structures. In this study, cantilever samples, which would crack in an anticipated manner, were designed using simulation techniques from known residual stress phenomena, then built and monitored using gas-borne AE on the EOS M280 system with TI6Al4V(ELI) powder. It was shown that the cracks/delaminations that occur during the metal L-PBF process can be detected and distinguished from other machine noises using their frequency and time-domain AE features. The peaks in the amplitude of the signal emitted in the time domain during the build process could be used to indicate the occurrence of cracks after applying an adequate filter and voltage threshold. The frequency characteristics of the signal could also clearly indicate the occurrence of the cracks and differentiate between the signals from the cracks and the machine noise.

TABLE OF CONTENTS

Declaration of independent work....ii

Acknowledgements.... iii

Abstract....iv

Table of contents....v

List of Figures.... viii

List of Tables....xi

Glossary....xii

Chapter 1: Introduction....1

1.1. Background....1

1.2. The aim of the study....2

1.3. The scope of the study....2

1.4. Objectives....2

1.5. Research methodology....2

1.6. Overview of the dissertation....2

1.7. Expected contributions....3

1.8. Publications and presentations to date....3

Chapter 2: Literature review....5

2.1. Additive manufacturing....5

2.2. Laser powder bed fusion....7

2.2.1. Laser....9

2.2.2. Build chamber conditions for L-PBF processing....10

2.3. Laser beam - powder bed interaction....10

2.3.1. Single track formation....11

2.3.2. Single layer formation....13

2.3.3. 3D object formation....14

2.4. Residual stress and cracking....15

2.4.1. Cracking in L-PBF 19

2.4.2. Cantilevers for residual stress quantification 21

2.5. Non-destructive testing methods in AM 23

2.6. Acoustic emission 25

2.6.1. Sound transmission 25

2.6.2. Microphones 26

2.6.3. Data acquisition 28

2.6.4. Acoustic emission testing 29

Chapter 3: Material and methods 36

3.1. Introduction 36

3.1.1. L-PBF processing 36

3.1.2. Ti6Al4V (ELI) powder 38

3.2. Design of cracking cantilever sample and numerical simulations 38

3.3. Acoustic emission testing 40

3.3.1. AE monitoring 40

3.3.2. AE from machine noise 40

3.3.3. AE from cracks of designed cracking cantilever samples 41

Chapter 4: Results and discussion 43

4.1. Cracking sample: numerical simulations and experimental validation 43

4.1.1. Numerical simulations 43

4.1.2. Validation of cracking sample height 45

4.2. AE signals during L-PBF manufacturing 46

4.2.1 Introduction to L-PBF AE results 47

4.2.3. Frequency-domain AE features of machine noise 49

4.2.4. Time-domain AE features of machine noise 52

4.3. Analysis of crack signals 57

4.4. Voltage threshold as a tool for crack detection 62

Chapter 5: Conclusions 67
  Future work 69
REFERENCES 70
Appendix 78
  A1. Data from AE recordings 78
    A1.1. Machine in idle 78
    A1.2 Dispenser moved down by 0.05 µm 79
    A1.3. Flooding valve opening 80
    A1.4. Flooding 81
    A1.5. Flooding valve closing 82
    A1.6. Build platform moved down by 1 mm 83
    A1.7. Build platform moved up by 1 mm 84
    A1.8. Recoater arm moved left 85
    A1.9. Recoater arm moved right 86
    A1.10. Recirculating fan 87
    A1.11. Laser scanning 88
  A2. Machine noise AE signals 89
  A3. Signal-to-noise ratio of cantilever cracks against noise signals (dB) 90
  A4. Peak amplitudes of cantilever cracks AE signals 91

LIST OF FIGURES

Figure 1: Operational schematic of various AM processes and their critical components (Francis et al., 2018) 6

Figure 2: Schematic of the L-PBF process (Leung et al., 2018) 7

Figure 3: Functional principle of an L-PBF process (RapidDMLS, 2022) 8

Figure 4: Basic components of a laser system (OptoSigma, 2022) 9

Figure 5: Galvano mirrors and lenses used to focus and move the laser spot (Raylase, 2022) 10

Figure 6: Mechanisms of spatter formation (Fedina, 2021) 11

Figure 7: L-PBF single track formation (Yadroitsev, 2009) 12

Figure 8: Denudation zone around a solidifying track (Wischeropp et al., 2019) 13

Figure 9: (a) Contouring with laser beam offset, (b) contouring without laser beam offset (Yadroitsev et al., 2021) 14

Figure 10: L-PBF solid 3D objects with fine features (a) (NSTF, 2023) and lattice structures, (b) (Yadroitsev, 2009) 15

Figure 11:(a) Residual stress profile after adding two layers of molten powder on baseplate, (b) residual stress profile of an L-PBF part after melting all layers forming the part 16

Figure 12: L-PBF residual stress influencing factors (Fang et al., 2020) 17

Figure 13: Residual stress development during L-PBF (Yadroitsev et al., 2021) 18

Figure 14: Relaxation of the residual stress after part removal (left) and resulting stress in the part (right) (Mercelis et al., 2006) 19

Figure 15: L-PBF part with crack induced by thermal stresses (Kruth et al., 2012) 20

Figure 16: Cracking and distortion due to residual stress in L-PBF(a–d); distortion(e–f) (Chen et al., 2022) 20

Figure 17: (a) Part before removal from baseplate, (b) Part after removal from baseplate with deflection due to residual stresses (Kruth et al., 2012) 21

Figure 18: XRD residual stress measurements of Ti6Al4V cantilever attached to substrate with principal stresses (Yadroitsava et al., 2015) 22

Figure 19: Residual stress field with varying bar height of Zr-based cantilevers' thickness (Xing et al., 2018) 22

Figure 20: Simulated residual stress contour of cantilever: (a) with support on substrate, (b) support removed from substrate (Li et al., 2016) 23

Figure 21: (a) Infrared camera online monitoring equipment set-up, and (b) thermogram

showing the HAZ (Krauss et al., 2012)..24
Figure 22: Schematic of ultrasonic testing set-up (Jamil et al., 2019)...................................25
Figure 23: Sound intensity variation with distance over a fixed solid angle (Eargle, 2005)..26
Figure 24: Cross-sectional view of a condenser microphone components (Brüel and Kjær, 1977)...27
Figure 25: (a) Pressure-field, (b) free-field, (c) and random-incidence microphone schematic (National Instruments Corporation, 2022)..28
Figure 26: Adequately sampled signal (top) and an inadequately sampled signal resulting in aliasing (bottom) (National Instruments Corporation, 2022)...29
Figure 27: Time-domain AE signal features (Ghayoomi et al., 2021).....................................30
Figure 28: Examples of air-borne (a) and structure-borne (b) acoustic sensor mounting on L-PBF systems (Yadroitsev et al., 2021)...31
Figure 29: Schematic of structure-borne piezoelectric ICP accelerometer AE sensor (PCB Piezotronics., 2023)..31
Figure 30: AE events vs location during fatigue crack propagation (Strantza et al., 2017)...32
Figure 31: Time-domain AE signal from EOS M280, unfiltered (left) and filtered signal (right) (Kouprianoff et al., 2018)...33
Figure 32: Schematic of experimental setup (top) and M280 chamber with reduced build volume (bottom): recoater arm (a), powder collector (b), build platform (c), powder dispenser (d), and ICP microphone (e)..37
Figure 33: CAD design of cantilever with strut numbers..39
Figure 34: Build plate setup of cantilevers..42
Figure 35: Effective plastic strain (left) and equivalent stress (right) at three possible failure heights for the first strut (see Figure 32)..44
Figure 36: Ti6Al4V powder bed redistribution around tip of cantilevers after failure..........45
Figure 37: Strut failure and deflection..46
Figure 38: Powder bed after failure (a), side view of cracking sample after powder cleaning on the substrate (b)...46
Figure 39 Amplitude-time graph (a) and frequency-time graph (b) of recorded AE signal...48
Figure 40: Unfiltered FFT (left) and STFT (right) of machine in idle (a), inert gas flooding (b), recoater arm movement (c), recirculating fan (d), and laser scanning (e).......................50
Figure 41: FFT (left) and unfiltered STFT (right) of build platform moved up by 1 mm (top),

and the build platform moved down by 1mm (bottom) 51
Figure 42: Peak voltage, RMS voltage and SNR of different L-PBF machine AE features 54
Figure 43: Time-domain AE signals of the machine is idle (a), build platform movement (b), recoater arm movement (c), recirculating fan (d), and laser scanning (e) 56
Figure 44: Unfiltered FFT (left) and filtered STFT (right) of AE from cantilever cracks, crack-S1-C1 (a), crack-S1-C2 (b), crack-S2-C1 (c), crack-S2-C2 (d), crack-S3-C1 (e), crack-S3-C2 (f), and crack-S4-C1 (g)...59
Figure 45: Signal-to-noise ratio of the average cantilever crack signal against the machine noise signals...62
Figure 46: Unfiltered (left) and filtered (right) time-domain AE signals of the cantilever, crack-S1-C1 (a), crack-S1-C2 (b), crack-S3-C1 (c), crack-S3-C2 (d), and crack-S4-C1 (e)..64
Figure 47: Time-domain AE features of cantilever cracks with dotted lines indicating the highest noise-peak amplitude after filtering 65
Figure 48: Amplitude-time graph of cantilever cracks with voltage threshold response of (a) (crack-S2-C2) and (crack-S3-C2), (b) one-second window of the same cracks.....................66

LIST OF TABLES

Table 1: Summary of metal AM processes and typical applications (Zhang et al., 2018) 5
Table 2: Ti6Al4V tensile results (Kouprianoff and du Preez, 2023) 43
Table 3: Cantilever failure heights 47
Table 4: Machine noise signals frequency response 52
Table 5: RMS of noise and laser signals 53
Table 6: Peak amplitudes of the L-PBF machine AE signals 55
Table 7: Cantilever crack signals frequency responses 60
Table 8: RMS of crack signals 61

GLOSSARY

AE	Acoustic emission
AM	Additive manufacturing
CAD	Computer-aided design
CRPM	Centre for Rapid Prototyping and Manufacturing
DAQ	Data acquisition
EOS	Electro Optical Systems
FFT	Fast Fourier transform
ISO	International Organization for Standardization
ICP	Integrated Circuit Piezoelectric
L-PBF	Laser powder bed fusion
ML	Machine learning
NDT	Non-destructive testing
RMS	Root-mean-square
SNR	Signal-to-noise ratio
SPL	Sound pressure level
STFT	Short-time Fourier transform)
STL	Standard Triangle Language
UT	Ultrasonic testing
UTS	Ultimate tensile strength
XRD	X-Ray diffraction

CHAPTER 1: INTRODUCTION

1.1. Background

Additive manufacturing (AM) is defined as “the process of joining materials to make parts from 3D model data, usually layer upon layer, as opposed to subtractive manufacturing and formative manufacturing methodologies” by the ISO/ASTM 52900 standard (2021). Laser powder bed fusion (L-PBF) is an AM process commonly used for both rapid prototyping and the production of metal parts. The L-PBF process is a complex and sensitive one where the quality and resulting material properties depend on various process parameters such as the laser power, scanning strategy, hatch spacing, build environment conditions and powder material properties. The high-temperature gradients during the heating and cooling cycles induce residual stresses in the built part which often leads to deformations and the formation of cracks. These defects hinder the quality assurance of the built part, resulting in the need for quality control measures. The quality monitoring systems currently available, such as that of the EOS GmbH optical tomography system, which uses imaging techniques that measure the temperatures during the build process, can be complemented by other methods, such as acoustic emission (AE), which monitors the stress waves propagated by a sudden redistribution of stress in a material. The use of AE can be dated as far back as 1933 by Kishinoue and has been applied to examine flaws in pressure vessels and stress corrosion cracking, among others, and is more sensitive in detecting crack growth compared to other non-destructive testing (NDT) methods. During L-PBF, AE can be divided into gas- and structure-borne emissions originating from the stress waves induced by changes in the internal structure of the part being processed. Structure-borne AE monitoring refers to an AE monitoring technique where an AE sensor is attached directly to the body of the object to monitor the elastic stress waves emitted by the object, mainly for defect analysis. In gas-borne AE monitoring, the elastic stress waves (sound), which are emitted by the monitored object, travel through a medium (air) and are measured with an AE sensor such as a microphone. AE is a relatively cost-effective online monitoring method which is easy to implement and has a high signal-to-noise ratio, fast response, and lower data rate than imaging systems (Shevchik et al., 2018; Schumacher et al., 2022).

1.2. The aim of the study

The aim of the study is to investigate whether gas-borne AE can reliably be used to detect cracks during an L-PBF Ti6Al4V process and to investigate what factors influence the type and minimum size of cracks that can be detected.

1.3. The scope of the study

This research study is concerned with creating an understanding of the applicability of monitoring the L-PBF build process for defects such as cracks using non-destructive techniques such as gas-borne AE for Ti6Al4V(ELI) objects, which can be applied not only to Ti6AL4V powder but also other L-PBF powders.

1.4. Objectives

- Understand the nature of L-PBF and gas-borne AE during the L-PBF process.
- Distinguish between sound emitted during the L-PBF process and that of cracks.
- Show that AE can detect cracks, more specifically for titanium alloys such as Ti6Al4V(ELI), which is used for medical implants and the aerospace industry.
- Based on the knowledge gained, propose a possible way to detect cracks in real time using AE.

1.5. Research methodology

- Design, develop and build a Ti6Al4V(ELI) 3D “cracking” sample.
- Record gas-borne AE signals of the entire building process of the sample.
- Analyse the relationship between AE and cracks.
- Distinguish between AE signals from different sources during L-PBF processing (laser scanning, re-coating, other noise and cracks).
- Characterisation of different crack signals for Ti6Al4V, which can, in turn, be used for feedback on the process quality and/or terminate the building process if a crack is detected.

1.6. Overview of the dissertation

The following outline defines the dissertation structure:

- Chapter 1: Introduction: A brief background on AM, L-PBF and AE is described. The aim, scope, objective, and research methodology of the study are also presented in the chapter.
- Chapter 2: Literature review: An in-depth study of the L-PBF process, residual stress and causes of cracking in L-PBF, along with investigations of NDT methods, such as the use of AE in L-PBF, is conducted in the chapter.
- Chapter 3: Materials and methods: The equipment and materials selected to conduct the experiments are described, and the methods used in designing and developing the "cracking cantilever sample".
- Chapter 4: Results and discussion: The validation of the 'cracking cantilever sample' is presented in the chapter, as well as the time and frequency domain AE features of the characterised machine noise and crack AE signals.
- Chapter 5: Conclusions: Conclusions are drawn from the study and presented in the chapter based on the results obtained.

1.7. Expected contributions

The presence of cracks and delaminations is undesirable during L-PBF since cracks and delaminations affect the mechanical properties and quality of the final L-PBF product. Parts with defects which are identified during the production process will significantly reduce the production costs due to reduced consumption of powder materials required for the build. In this work, AE is utilised to detect and characterise the signals of these defects to add to the existing body of knowledge for in situ monitoring using AE as a quality control method.

1.8. Publications and presentations to date

- Moore, K., Louw, D., Kouprianoff, D., 2022. Developing a Ti6AL4V specimen to induce residual stress deformations and cracks for use in metal additive manufacturing online monitoring. RAPDASA 23rd International Conference, 9–11 November 2022, Somerset West, Cape Town, South Africa.
- Kouprianoff, D., Moore, K., 2022. Effect of design and tensile testing specimen geometry on final properties of powder bed fusion plastic. RAPDASA 23rd International Conference, 9–11 November 2022, Somerset West, Cape Town, South Africa.
- Moore, K., Kouprianoff, D., Louw, D., Yadroitsava, I., Yadroitsev, I., 2023. Monitoring for cracks in metal L-PBF using gas-borne acoustic emission. South African Journal of Industrial Engineering, 34(4), pp.147-154. https://doi.org/10.7166/34-4-2981

- Moore, K., Kouprianoff, D., Yadroitsava, I., Yadroitsev, I., 2024. Characterization of machine signals during L-PBF for online monitoring using gas-borne acoustic emission. RAPDASA 25th International Conference, 28–31 October 2024, Gqeberha, Eastern Cape, South Africa. (Submitted) Chapter 2: Literature review.

CHAPTER 2: LITERATURE REVIEW

2.1. Additive manufacturing

Additive manufacturing (AM), also known as 3D printing, is a manufacturing technique that first emerged in the 1980s with one of the first 3D printing machines manufactured by a company named 3D Systems, founded by Charles Hull (de Beer et al., 2016). The AM technology then evolved over the years into various types of manufacturing techniques such as powder bed fusion (L-PBF), fused deposition melting (FDM), direct energy deposition, etc. Table 1 shows a summary of some of these metal AM processes and their applications.

Table 1: Summary of metal AM processes and typical applications (Zhang et al., 2018)

AM process	**Typical applications**
Binder jetting	Prototyping, investment casting
Material jetting	Visual prototyping
Powder bed fusion	Functional prototyping, engineering functional parts
Sheet lamination	Prototyping
Direct energy deposition	Prototyping, functional parts, repairing metal parts and fixtures

In AM, the parts are built in a layer-by-layer manner, where material is deposited on a build plate or extruded from a nozzle and fused, melted or solidified according to the computer-aided design (CAD) model. Each successive layer bonds to the preceding layer of melted or partially melted material to form a 3D part. In contrast to traditional methods of manufacturing, which use subtractive manufacturing, where it is often necessary to remove material through milling, machining, carving, or other means, AM adds material to create an object. Various materials, such as metals, plastics and composite materials, can be used for the process. Figure 1 illustrates the various AM processes and their critical components.

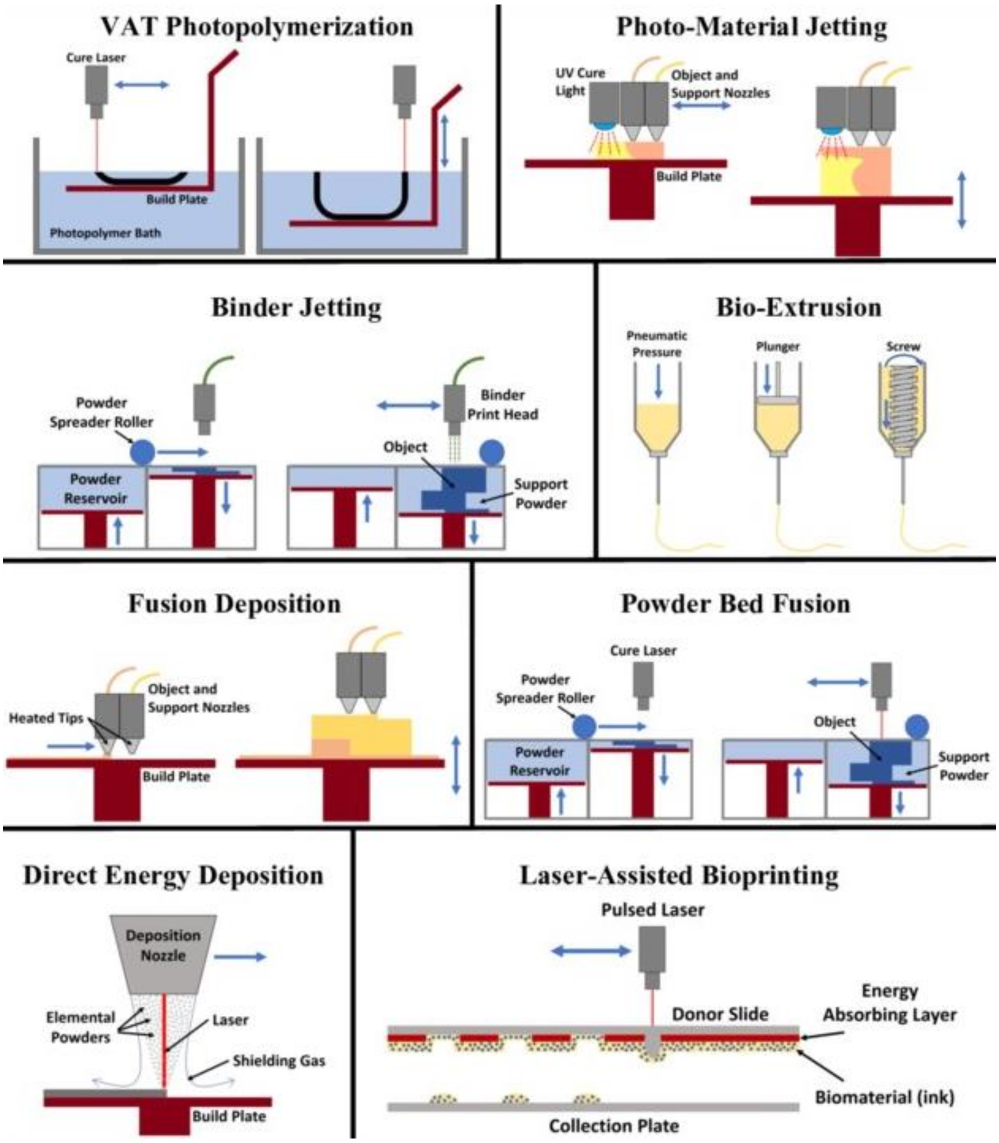

Figure 1: Operational schematic of various AM processes and their critical components (Francis et al., 2018)

One prominent advantage of using AM is that it gives engineers/designers the freedom to design any object with complex shapes, as the method builds the entire object as a single body (EOS GmbH, 2022).

2.2. Laser powder bed fusion

L-PBF is an AM method commonly used for both rapid prototyping and mass production of metal and plastic parts where an inert atmosphere, usually nitrogen or argon, is required. The components and process of the L-PBF are shown in Figure 2. A CAD model is processed (sliced) by software and supplied to the 3D printer. The build process begins with an adequate layer of powder being deposited onto the build platform by the recoater arm, which forms a single layer of powder. A laser is then used to selectively melt the powder material according to the CAD model (Jhabvala et al., 2010). When the single layer is completed, the building platform is lowered, a new layer of powder is applied, and the process is repeated until the 3D part is completed (Everton et al., 2016). Upon completion, the part is left to cool, and the surrounding loose metal powder is removed from the machine. Post-processing such as heat treatment, support removal, machining or surface finishing may be required.

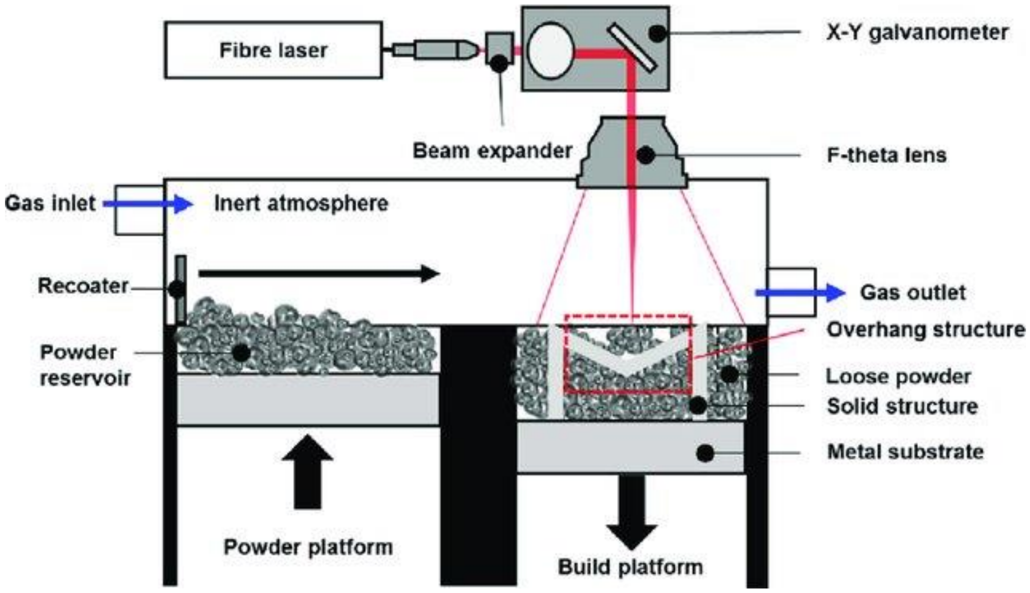

Figure 2: Schematic of the L-PBF process (Leung et al., 2018)

The functional principle of an L-PBF process is shown in the flow diagram in Figure 3.

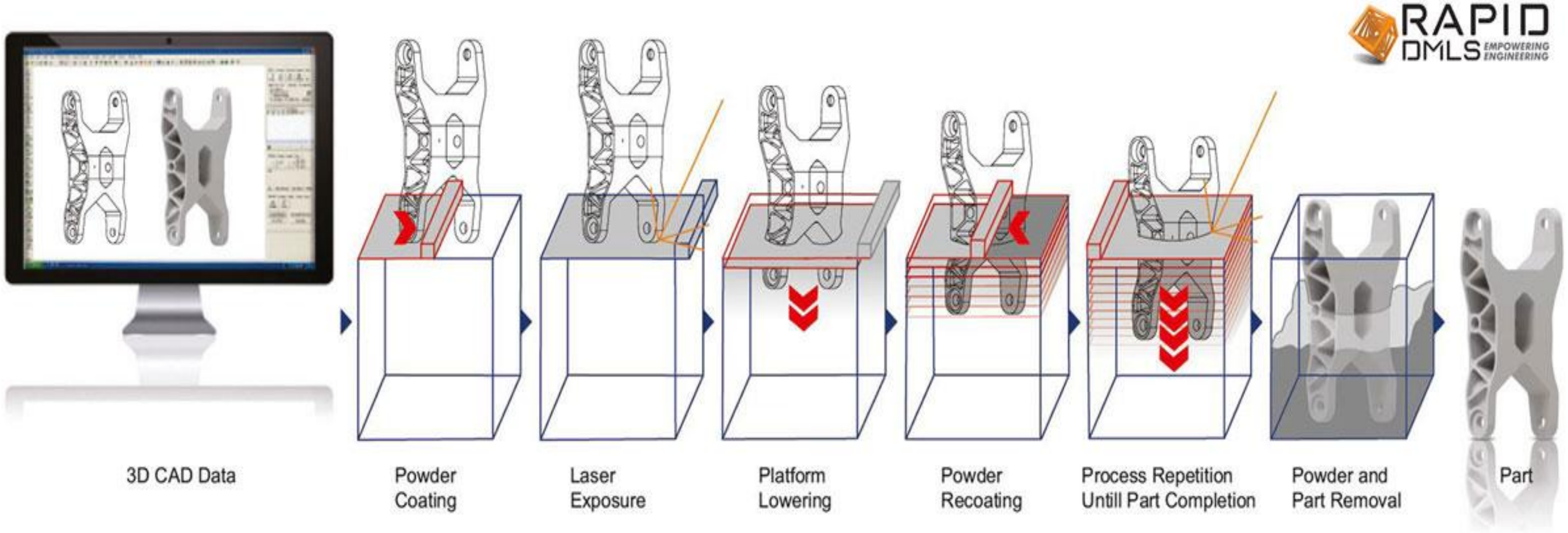

Figure 3: Functional principle of an L-PBF process (RapidDMLS, 2022)

2.2.1. Laser

A laser is a device that emits light through a process of optical amplification based on the stimulated emission of electromagnetic radiation. The word laser is an acronym for "light amplification by stimulated emission of radiation" (NASA Science, 2022). There are various types of lasers, namely gas, fibre, solid state, dye, diode, and excimer lasers. Figure 4 illustrates the basic components of a laser system.

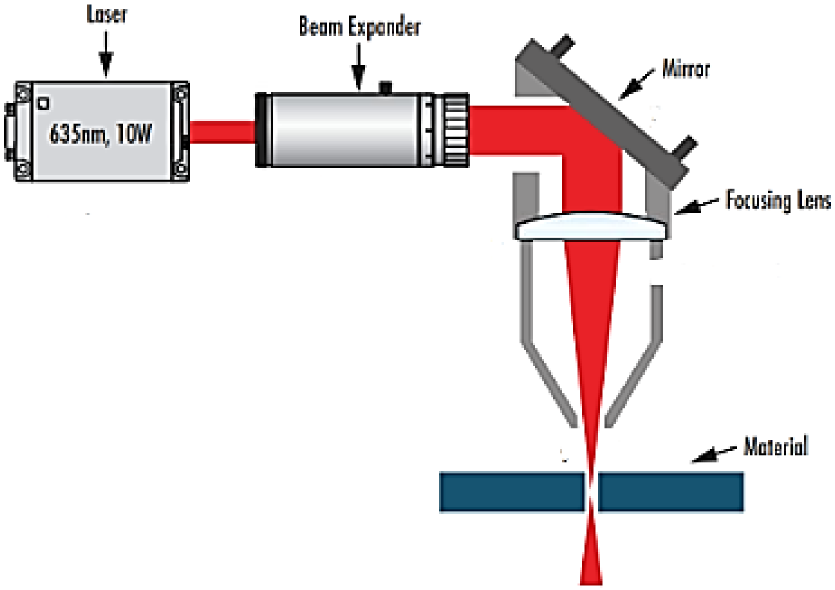

Figure 4: Basic components of a laser system (OptoSigma, 2022)

The neodymium-doped yttrium aluminium garnet (Nd:YAG) and carbon dioxide (CO_2) industrial lasers are historically the two most-used lasers in L-PBF processing of metallic powders. In recent years, the ytterbium (Yb)-doped fibre lasers have been used as substitutes for Nd:YAG lasers in most L-PBF applications (Cobbinah et al., 2021).

Yb-fibre lasers offer various advantages, such as high electrical to optical efficiency, excellent beam quality, and system compactness. The light transmission of the Yb-fibre laser beam is permitted through optical fibre cables, rather than being transmitted through the articulated mirror delivery system employed by CO_2 lasers. This leads to the Yb-fibre laser beam being able to be more easily manipulated onto the building bed. The focusing and positioning of the laser is accomplished by an F-theta lens and two galvanometer scan mirrors, as seen in Figure 5 (Gögelein et al., 2018).

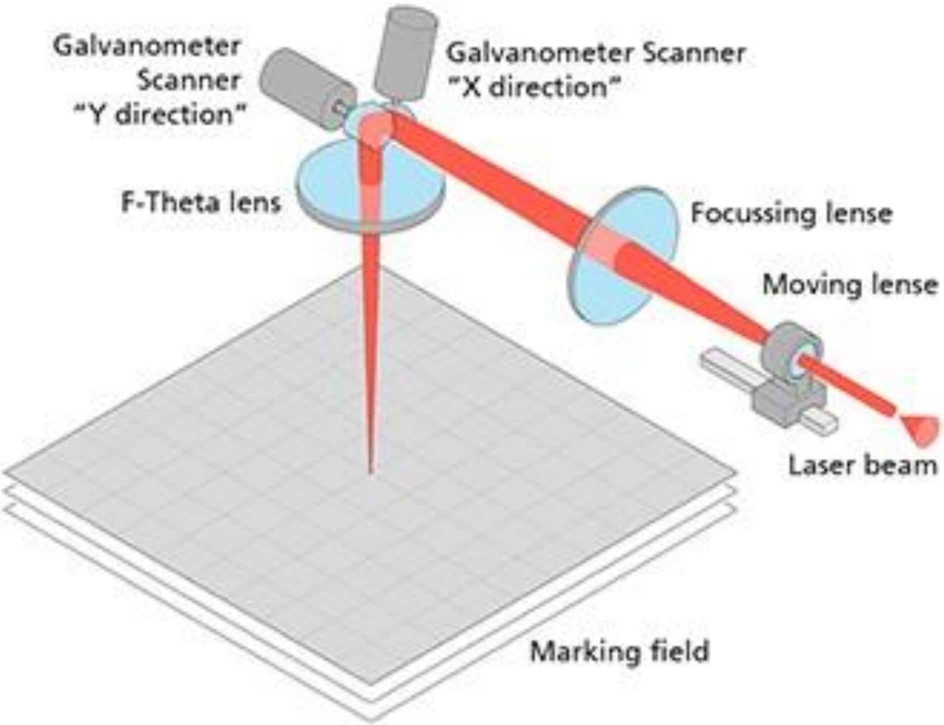

Figure 5: Galvano mirrors and lenses used to focus and move the laser spot (Raylase, 2022)

2.2.2. Build chamber conditions for L-PBF processing

One of the challenges in metal AM is to build components in a controlled environment that minimises the introduction of any possible impurities such as fumes generated at the melt pool which would interfere with the laser. The slightest variations in the oxygen content in the build chamber can impair the mechanical properties of alloys such as titanium and aluminium, resulting in oxidation of the alloys. The use of inert gases, such as argon and nitrogen, in the build chamber prevents the oxidation of these materials (Linde, 2018).

2.3. Laser beam - powder bed interaction

During the time that the laser beam makes contact with the powder bed or substrate, a phenomenon named spattering occurs, where small metal droplets or powder particles are ejected at the interaction area, as shown in Figure 6. Spattering is mainly caused by two fundamentals, namely the recoil pressure coupled with the Marangoni effect, and the vapour-driven particle entrainment by an induced gas flow *(*Ly et al., 2017*)*. It has been shown by Matthews et al. (2017) that the vapour-driven particle entrainment by an induced gas flow may be the dominant contributor to the formation of spattering during the L-PBF process.

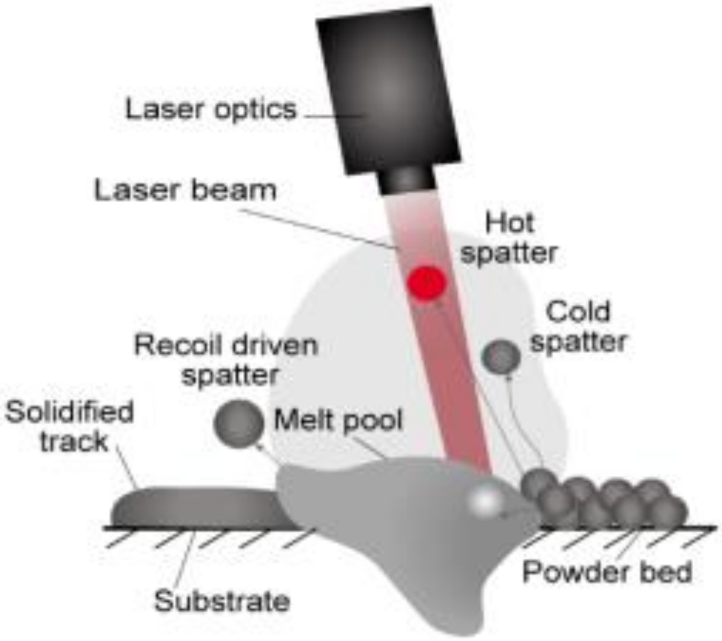

Figure 6: Mechanisms of spatter formation (Fedina, 2021)

Spattering is a common phenomenon in L-PBF and is generally considered to be a detrimental process which leads to a decrease in part quality. Dal et al. (2017) has shown that the laser power and scanning speed has a large impact on the degree of spattering, whereas the chamber pressure influences the spattering behaviour by controlling the divergence angle of the vapour jet and the inert gas flow.

2.3.1. Single track formation

In L-PBF, a single track is formed when the laser beam interacts with the metal powder pre-deposited on a build plate in a single line, melting the powder fully from the thermal energy received from the laser. A melt pool is formed, which then solidifies along the scanning direction of the laser beam, forming a solidified single line of material, namely a single track (Yadroitsev, 2009; Shrestha et al., 2018). The final properties of the part being built in an L-PBF process depend on the quality of the single track. A microscopic image of an L-PBF single-track scanning direction and properties is shown in Figure 7.

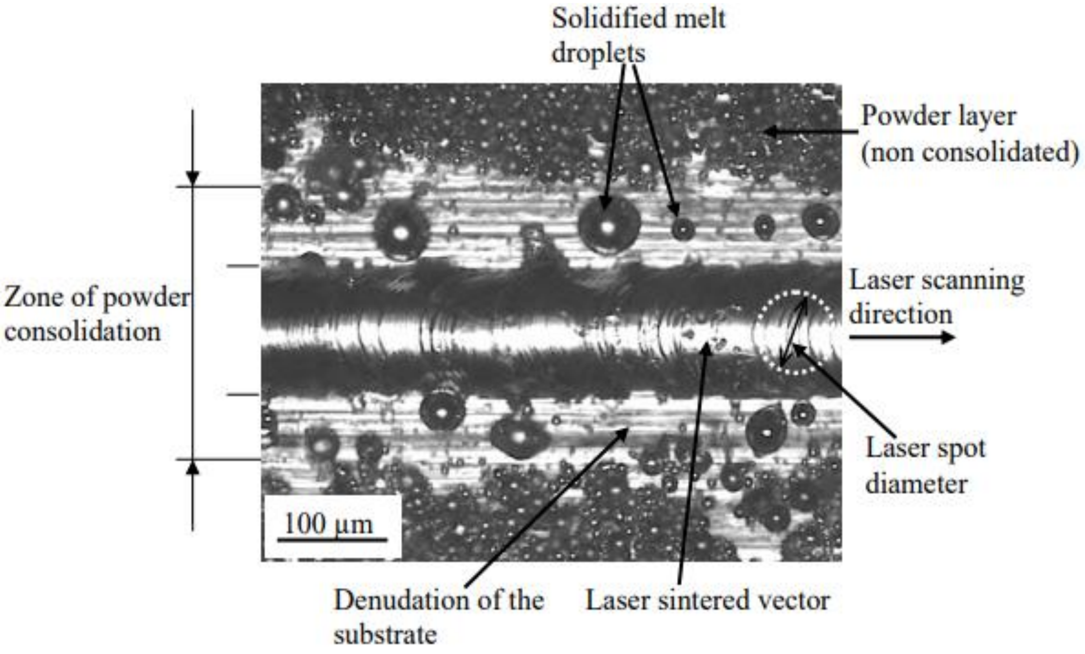

Figure 7: L-PBF single track formation (Yadroitsev, 2009)

Factors such as laser power, laser path, scanning speed and powder layer thickness have a significant influence on the quality of the single track, and for the formation of stable continuous tracks, which have a metallurgical bond with the substrate, the hierarchy of those process parameters range in order of importance from laser power density, powder layer thickness, scanning speed, and powder particle size (Yadroitsev et al., 2015). The laser-related parameters, such as the laser power, spot size diameter and coefficient of absorption of the material, have been suggested to have a great effect on the geometrical characteristics of the single track.

At high scanning speeds, a phenomenon called balling can occur. Balling occurs when the viscosity of the melt pool is too high and penetration into the substrate is too low (Yadroitsev et al., 2010; Mutke et al., 2018).

Another result of laser beam-powder interaction in L-PBF is the denudation phenomenon that was described first by Yadroitsev et al. in 2007. Denudation describes a particle depletion area observed near the laser scan path as a result of the interaction between the laser beam and the powder bed, as shown in Figure 8. The denudated area around the scanned path, which is also called the denudation zone, varies depending on the process parameters and ambient gas pressure. The gas flow has an impact on the degree of denudation which, in turn, will directly affect the resulting quality of AM components (Martin et al., 2019).

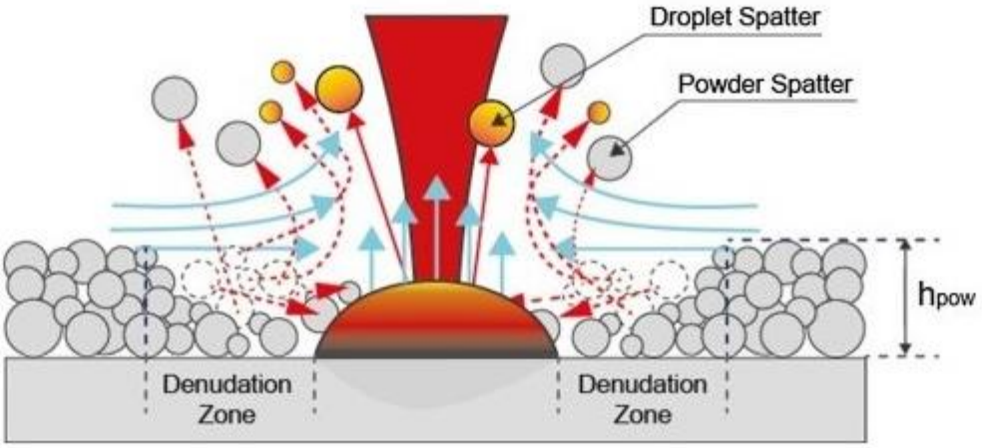

Figure 8: Denudation zone around a solidifying track (Wischeropp et al., 2019)

2.3.2. Single layer formation

A single layer in an L-PBF process is formed from a series of single tracks. The surface finish of the single layer is dependent on the geometric characteristics of the single track, the powder layer thickness and the process parameters, such as the scanning strategy and hatch distance. The hatch distance is the distance between the centre of one single track to another. The high hatch distance leads to gaps (pores) being formed between the solidified tracks, resulting in a surface finish that is not continuous (Yadroitsev, 2009). Various hatching patterns are used in L-PBF with the most frequent being the stripes and island (chessboard) scanning method. The scanning strategy refers to how the laser scans a specific cross-section. To maintain the dimensional accuracy of the single layer, the laser beam must be offset from the edges of the scanned cross-section as the melt pool is generally larger than the laser spot size (Figure 9). The formation of a single layer consists of multiple interconnected physical phenomena which are case sensitive, as by merely altering one of these phenomena, such as the scanning strategy or process parameters, this can result in defects within the layer such as porosity, inaccurate dimension, or high surface roughness, etc.

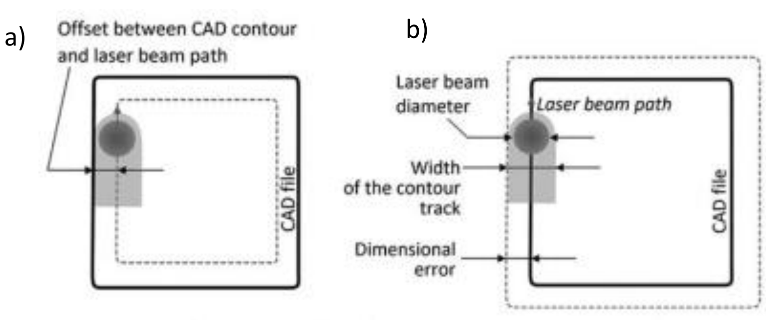

Figure 9: (a) Contouring with laser beam offset, (b) contouring without laser beam offset (Yadroitsev et al., 2021)

2.3.3. 3D object formation

A 3D object in an L-BPF process is formed from a series of single layers as a layer is added onto the preceding layer and can be divided into three parts, namely the core, upskin, and downskin areas. The skin is the area of the 3D object that has no upper solidified layers, and the down skin is the area with no underlying solidified layers. The core of the 3D object is defined as the inner region of the object. The layer-by-layer nature of the L-PBF process often results in different surface qualities between the layers in the Z direction and the horizontal XY direction. The downskin of the 3D object is usually rougher and has a poorer surface finish than the upskin. The mechanical properties of the 3D object are determined by the solidification microstructure, where the solidification structure depends on the local solidification (Zhang et al., 2007). When the build of the 3D object is complete, the part is left to cool in the machine as the induced residual stresses may cause defects such as cracks or warping if the object is removed before cooling down.

To clean off the powder on the surface of the 3D object, compressed air and an ultrasonic bath are used. A heat-treatment cycle is used to remove residual stress in the L-PBF object and to change its microstructure and mechanical and fatigue properties. To improve the surface finish of the L-PBF parts, surface finishing procedures such as surface polishing may be required. In Figure 10(a), a solid 3D object is shown, and Figure 10(b) shows a thin-walled (lattice) 3D object. Due to their thickness, thin-walled structures are formed from a series of single tracks that are formed onto each other in the Z-direction. They are mainly used for lightweight, high-strength applications, such as in the aerospace industry.

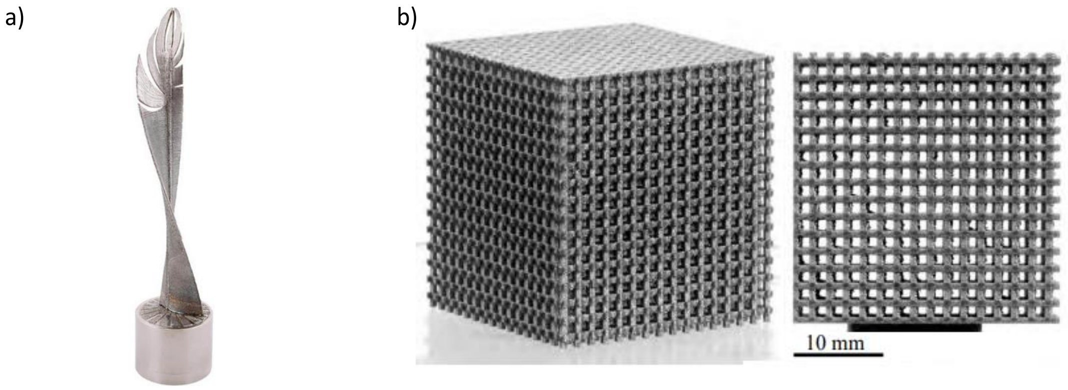

Figure 10: L-PBF solid 3D objects with fine features (a) (NSTF, 2023) and lattice structures, (b) (Yadroitsev, 2009)

2.4. Residual stress and cracking

Residual stress in a material or object is those stresses that exist in the object without any application of external loads. In general, residual stresses are not considered a negative phenomenon all the time, as in some processes, such as the manufacturing of glass plates, these stresses are needed to introduce compressive stresses in the surface area of the plate by rapidly cooling it to prevent crack growth and to increase the overall loading resistance (Mercelis et al., 2006). Residual stresses present a quality challenge in L-PBF, negatively affecting factors such as mechanical properties, surface integrity, shape, and dimensional accuracy, as well as inducing cracking and affecting fatigue life (Mugwagwa et al., 2019). Residual stresses are caused by the localised thermal heating and melting of the material by the laser during the L-PBF process, which generates rapid heating and cooling cycles. These cycles result in induced thermal stresses and residual stresses in the built part due to the volume of the part not being able to expand and contract freely in response to these temperature fluctuations (Kruth et al., 2012). Residual stresses have mechanical, chemical and thermal origins and exist in an object with the presence of tensile stresses (positive in sign) and compressive stresses (negative in sign (Mugwagwa et al., 2021).

Mercelis and Kruth (2006) described two mechanisms to explain L-PBF residual stresses, the first one being the temperature gradient in which, during heating, the exposed layer expands due to the high temperatures but is restricted by the cold underlying substrate, as seen in Figure *13*. The second mechanism is the cool-down mechanism, which occurs when the irradiating laser beam is removed and the top surface shrinks. However, this shrinkage is restricted by the underlying layers, which cause residual stresses. In Figure 11, a simplified model used by Kruth et al. (2012) to model the thermal stresses in an L-PBF process is shown. The model quantifies the cool-down phase mechanism by using the equilibrium of forces and assuming that the residual stress in the last layer is equal to the yield strength of the material. This assumption results in high tensile stresses being formed in the part and compressive stresses being formed in the upper point of the baseplate with lower tensile stresses in the lower point of the base plate.

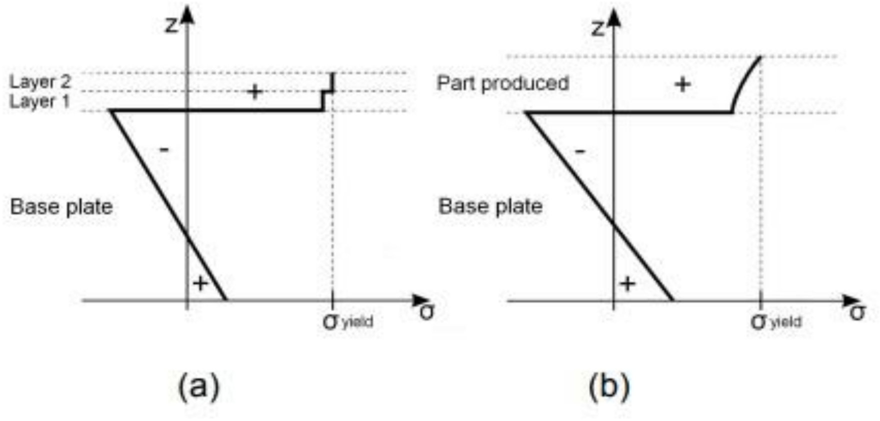

Figure 11:(a) Residual stress profile after adding two layers of molten powder on baseplate, (b) residual stress profile of an L-PBF part after melting all layers forming the part (Kruth et al., 2012)

Various methods are used to measure these residual stresses, such as X-ray diffraction, the crack compliance method, the strain gauge hole drilling method, and the contour method etc. Vrancken et al. (2014) used the contour method to study residual stress in compact tension specimens produced by L-PBF and found that the major contributing factor in the anisotropic behaviour of materials is residual stress. Yadroitsava et al. (2015) measured the residual stresses of square 316L L-PBF samples at the centre using the sin2 ψ method and found that the stresses perpendicular and along the scanning direction were tensile. The maximum residual stresses were found near the substrate, which exceeded the yield strength of wrought material.

The inherent strain method, which was initially used for numerical predictions of deformations for welded structures, is now a common method used in the prediction of deformations and distortions in L-PBF manufactured parts (Keller et al., 2014). The inherent strain method only considers mechanical strain and assumes that each laser scan has the same thermo-mechanical properties. Inherent strains are dependent on the material properties and process parameters and can either be simulated or determined experimentally by measuring the inherent deformations due to the release of the residual stresses. Furumoto et al. (2010) studied the influence of the thickness of the baseplate and the height of the structure separating the build plate and the baseplate on the residual stresses by attaching a strain gauge at the bottom of the baseplate and found that the consolidation structure consisted of tensile stresses in each position measured. The residual stresses at the top layer of the separating structure and at the point between the base plate and the separating structure were very high.

Factors such as the geometry of the part, the building orientation, support structures, powder layer thickness and process parameters, etc., have all been shown to have an influence on the residual stresses experienced by a specimen, see Figure 12. Mercelis et al. (2006) showed that increasing the number of layers (the thickness/height of the specimen) is accompanied by a steady increase in deformation and residual stresses. Van Zyl et al. (2016) indicated that at selected process parameters, the direction of the major stresses in L-PBF Ti6Al4V samples was coaxial with the scanning direction.

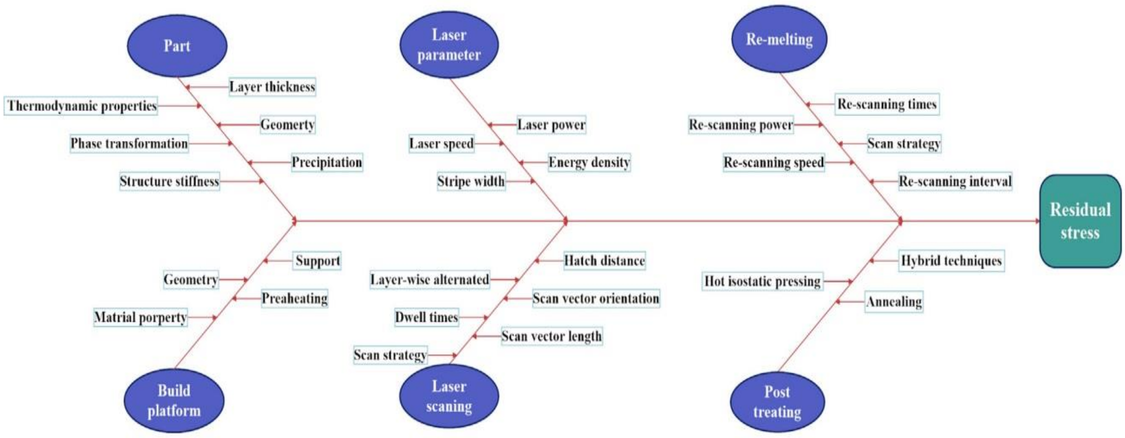

Figure 12: L-PBF residual stress influencing factors (Fang et al., 2020)

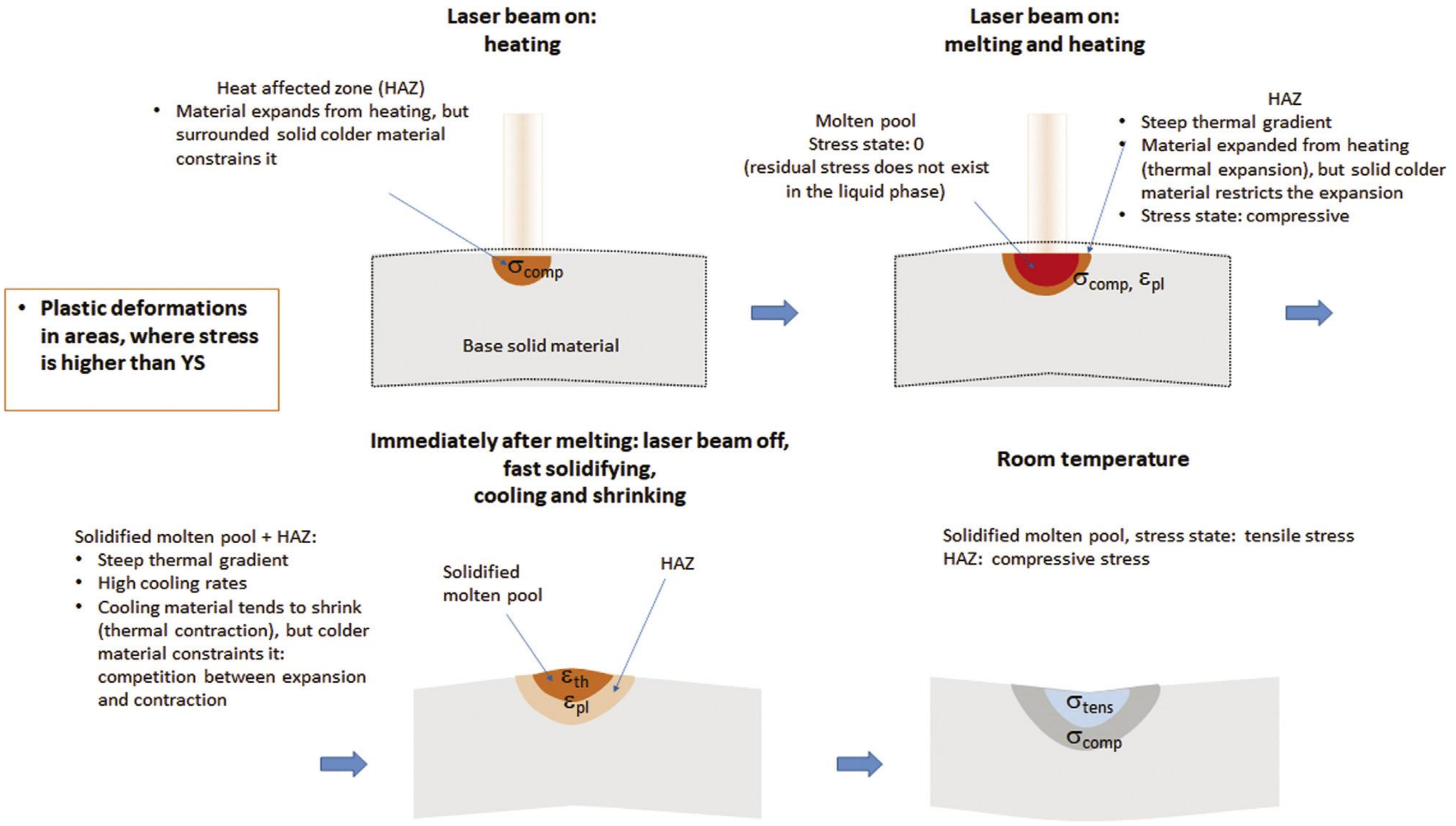

Figure 13: Residual stress development during L-PBF (Yadroitsev et al., 2021)

Mercelis et al. (2006) showed a presence of tensile stresses at the upper layers of the part with compressive stresses in between (Figure 14).

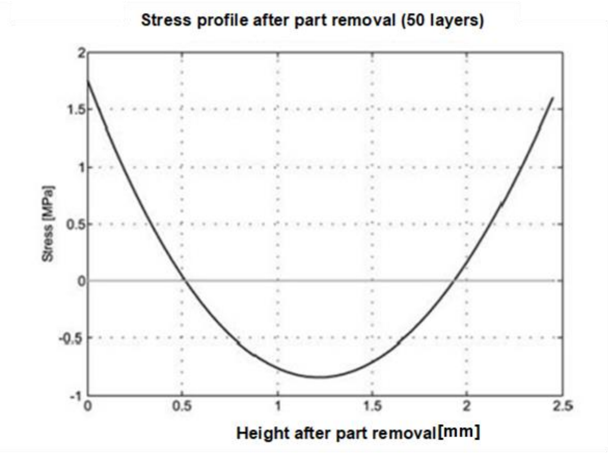

Figure 14: Relaxation of the residual stress after part removal (left) and resulting stress in the part (right) (Mercelis et al., 2006)

2.4.1. Cracking in L-PBF

Cracks are considered detrimental effects in L-PBF, which can affect the performance of the component for the desired application. Excessive thermal residual stresses in a component can lead to surface or subsurface cracking, as shown in Figure 15. These cracks occur mainly due to the thermal gradients, which induce residual stresses that exceed the local rupture resistance of the material due to the quick cooling rates experienced. The internal pores, sharp edges and interface between the build plate and part are also the possible cause of crack initiation (Platl et al., 2022). To understand the crack growth of metal alloys, a variety of thermomechanical models have been developed to get a better understanding of how the thermal gradients, thermal transient stresses and residual stresses develop in an L-PBF component (Li et al., 2004; Soundararajan et al., 2021). However, most of these models do require a substantial amount of computational time and power to simulate the L-PBF process due to the complex nature of the thermal fields.

In the work of Li et al. (2004), the maximum tensile stress was shown to determine the cracking behaviour of the ceramics while the critical tensile hydrostatic stress criterion depicted crack initiation and altered the crack direction. In 2013, Leuders et al. studied the fatigue resistance and crack growth performance in Ti6Al4V samples and found that in contrast to crack initiation, which is influenced primarily by the pores, the main influencing factor on crack growth is the residual stress.

Figure 15: L-PBF part with crack induced by thermal stresses (Kruth et al., 2012)

In Figure 16(e–f), warping due to the residual stresses can be seen. In Figure 16(e), the cantilever has been bent upward and has failed with the build plate. Slight distortion/warping of the parts will not affect the build process, but significant warping, which is more than the deposited layer thickness coupled with the separation of the part from the substrate, can lead to damage to the recoater blade due to impact with the distorted part. Recoater blade impact can also lead to possible displacement of the part (Yadroitsava et al., 2015).

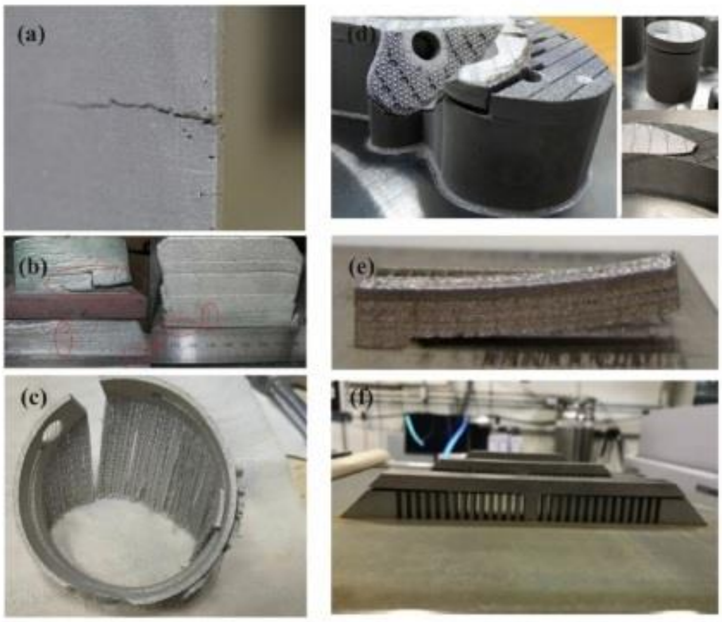

Figure 16: Cracking and distortion due to residual stress in L-PBF(a–d); distortion(e–f) (Chen et al., 2022)

The literature shows techniques such as baseplate pre-heating, including support structures, rescanning the layers, and using higher laser power and lower scan speeds, among others, to reduce the possibility of crack formation in L-PBF metal alloys (Levkulich et al. 2019; Böhm et al., 2022).

2.4.2. Cantilevers for residual stress quantification

The National Institute of Standards and Technology (NIST) developed an experimental program named AM-Bench (AMB2018-01) to provide a measurement benchmark for all AM materials and methods. Within the program, an L-PBF cantilever with 12 supporting legs and varying thicknesses was built (National Institute of Standards and Technology, 2023). Cantilevers are used as a quick and reliable method to quantify the residual stress in a component and to optimise the process parameters accordingly in an attempt to reduce these stresses. The concept was initially proposed by Kruth et al. (2012) using the bridge curvature method, which is shown in Figure 17. The method is used in order to simply and accurately analyse possible scanning strategies to reduce residual stresses during L-PBF. The method consists of building bridge-like structures on a baseplate and after removal, the amount of curvature is used as a measure of the magnitude of the residual stress within the part.

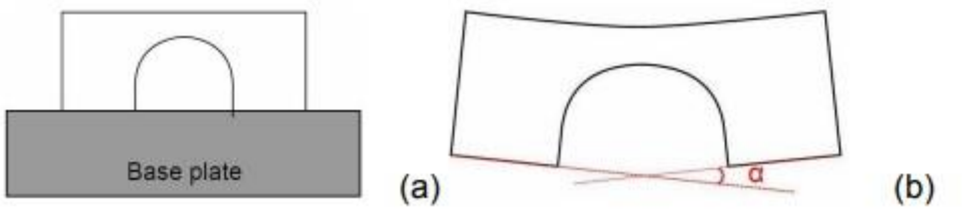

Figure 17: (a) Part before removal from baseplate, (b) Part after removal from baseplate with deflection due to residual stresses (Kruth et al., 2012)

In 2015, Yadroitsava et al. built cantilevers with thin walls as support structures and measured the residual stresses near the surface using the XRD method, as shown in Figure 18. It was found that the principal residual stresses varied greatly, and the maximum values obtained were higher than the residual stresses in the Ti6Al4V samples that were manufactured without support structures. When the cantilevers were cut off the substrate, they deformed by bending upward. But after they were stress-relieved, the cantilevers did not deform or bend upward.

Currently, methods such as pre-heating the substrate, re-scanning each layer, and post-processing, i.e. furnace heat treatment, are being utilised to reduce the residual stresses in L-PBF manufactured parts (Ali et al., 2017; Karimi et al., 2021; Teixeira et al., 2020). Although some of these methods are more effective than others, as seen in work done by Kruth et al. (2012), post-processing thermal treatment resulted in less deflection of the bridge structure than optimising the process parameters such as laser scanning strategies.

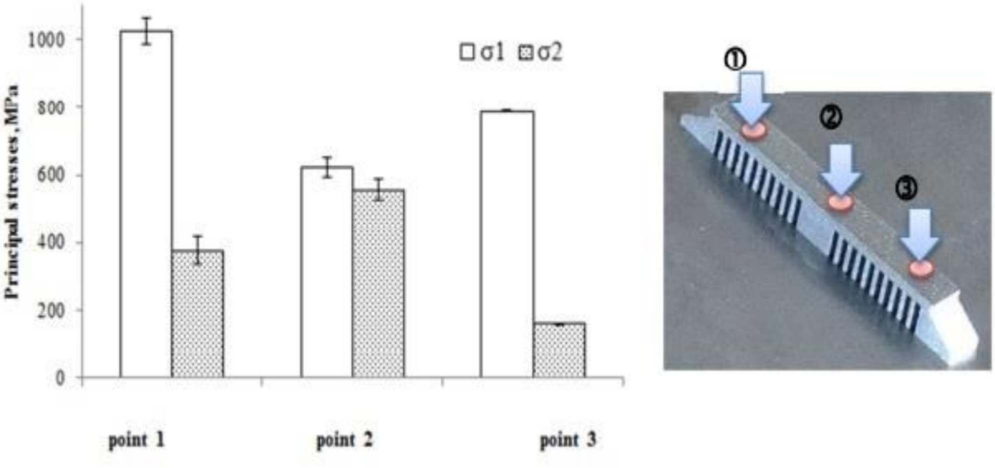

Figure 18: XRD residual stress measurements of Ti6Al4V cantilever attached to substrate with principal stresses (Yadroitsava et al., 2015)

Xing et al. (2018) used a cantilever simulation model in an attempt to estimate the residual stresses in a Zr-based L-PBF amorphous alloy and found that the residual stress of the cantilever was dependent on the height of the horizontal bar, as shown in Figure 19, and the XY cross-scanning strategy yielded relatively lower residual stress results than the X and Y scanning strategies. The residual stresses at the interface between the cantilever and the substrate were found to be the largest and increased as the height of the bar was increased.

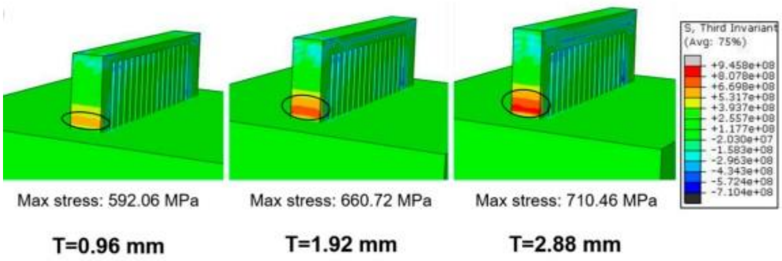

Figure 19: Residual stress field with varying bar height of Zr-based cantilevers' thickness (Xing et al., 2018)

Li et al. (2016) used the temperature thread multiscale modelling approach to predict the part distortion of twin cantilevers. The simulation results of the predicted von Mises and principal stresses are shown in Figure 20. The results showed that the maximum von Mises stresses were found on the top layer of the cantilever and on the interface between the substrate and the cantilever, which exceeded the yield strength of the material. The principal stress S_{11}, which was perpendicular to the part building direction, consisted of large tensile stresses, which could be explained by the temperature gradient mechanism, whereas the principal stress S_{22} consisted of mainly compressive stresses. When the cantilever support was removed from the substrate, the principal stress S_{11} on the top layer became compressive, which is caused by the layers beneath elastically deforming the cantilever to a point of equilibrium.

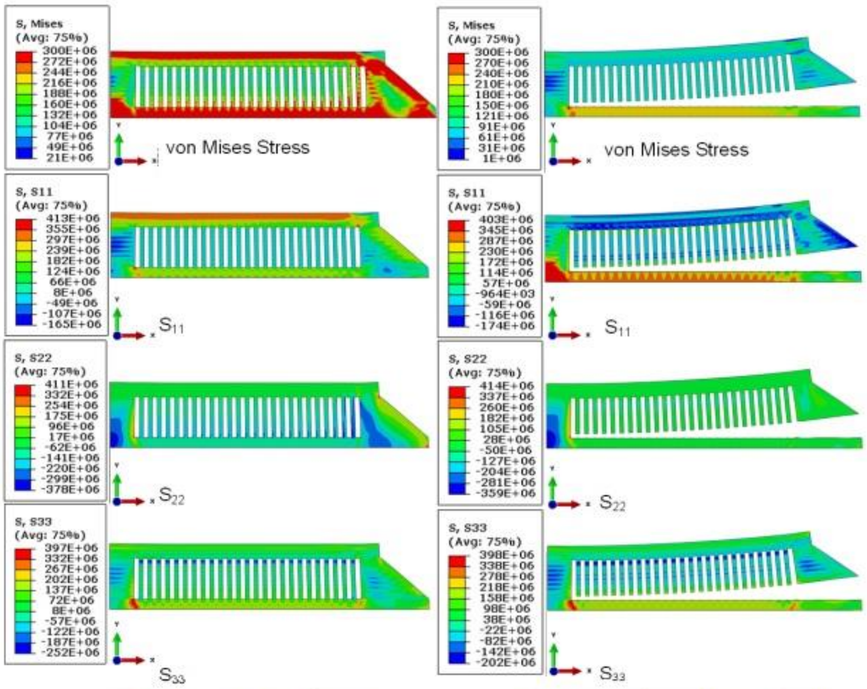

(a) With support on substrate (b) Support released from substrate

Figure 20: Simulated residual stress contour of cantilever: (a) with support on substrate, (b) support removed from substrate (Li et al., 2016)

2.5. Non-destructive testing methods in AM

Non-destructive testing (NDT) is a method which involves monitoring and analysing the characteristics of an object or system without causing any damage to it. Various NDT methods for quality control measures in L-PBF are available, such as radiographic, ultrasonic, and optical testing methods, etc. (Bartlett et al., 2018; du Plessis et al., 2021). Unlike destructive testing methods, which can be costly and time-consuming due to sample parts which need to be built and destroyed, NDT methods are the complete opposite, with capabilities of online monitoring systems that can monitor the L-PBF build process in detail (Krauss et al., 2012).

Everton et al. (2016) describe various studies that focus on methods for online monitoring systems which are used in different metal AM processes, such as the EOS GmbH system, which utilises optical tomography to measure the temperatures during the building process on the EOS M290 (EOS GmbH, 2022). Other in situ NDT monitoring methods, such as displacement sensors, acoustic methods and the use of synchrotron radiation-based scanning, can measure residual stresses at the micro and nanoscale and detect defects such as deformations and cracks during the build process are currently being investigated with an aim to improve the L-PBF process (Zhou et al., 2018; Lu et al., 2019).

In Figure 21, an example of an optical NDT method is shown where an infrared camera was used to investigate the limits for detecting artificial flaws and other irregularities caused by insufficient heat dissipation during the L-PBF process. Figure 21 (b) shows the thermogram of the heat-affected zone (HAZ) in a sample with an artificial flaw. One setback during this investigation was that only 30% of the build area could be monitored due to the external set up of the camera. Optical methods are effective in monitoring the melt pool of the build process though they lack accuracy due to gas or particles that reduce the temperature signal in the optical path. Optical systems also utilise large amounts of data as compared to AE systems, which can be as high as 75.1 GB (Köhler et al., 2013; Purtonen et al., 2014).

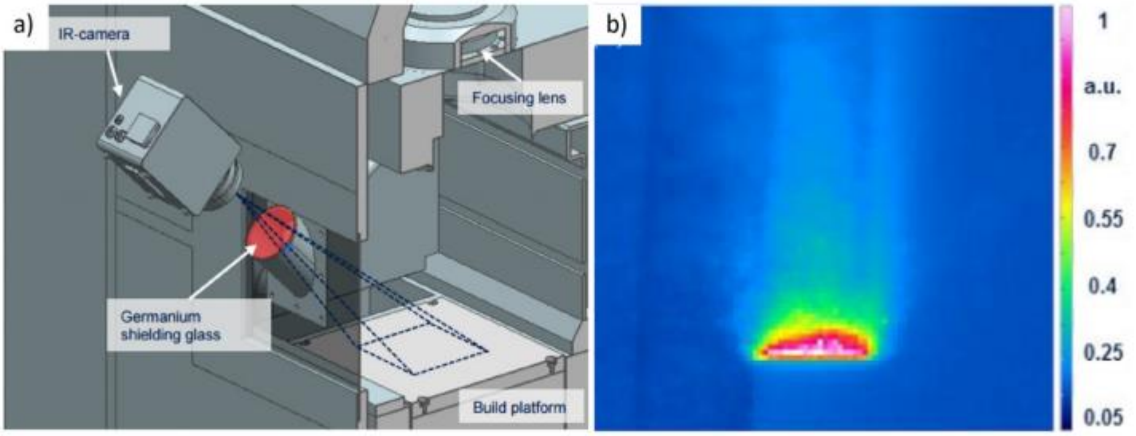

Figure 21: (a) Infrared camera online monitoring equipment set-up, and (b) thermogram showing the HAZ (Krauss et al., 2012)

Ultrasonic testing is used to measure the high-frequency sound waves in an object, where a wave is transmitted from one flat surface to the opposite parallel surface, and the reflected signal is then measured (Figure 22). This signal can be altered by defects such as cracks or pores present within the measured object (du Plessis et al., 2021).

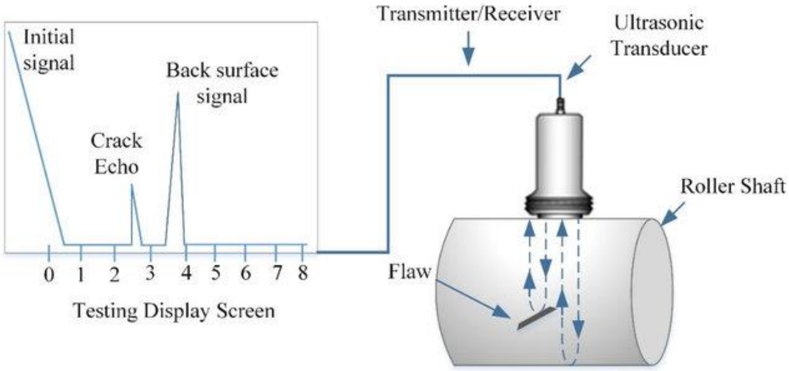

Figure 22: Schematic of ultrasonic testing set-up (Jamil et al., 2019)

2.6. Acoustic emission

Acoustic emission (AE) is an NDT method that is based on analysing elastic stress waves that are propagated by a sudden redistribution of stress in a material instigated by external forces (such as the thermal-driven phase transformations in metals). The use of AE can be dated as far back as 1933 to Kishinoue, who used a wooden device to record the AE signals from a needle inserted into the tension side of a beam under bending stress to study the fracture of the earth’s crust (Grosse et al., 2008). The term “AE” was first introduced by Shcofielde in the re-examined work of Kaiser in 1961, who discovered the Kaiser effect, which states that when a specimen is stressed, then relaxed and stressed again, no AE will be emitted until the previous maximum stress is exceeded.

2.6.1. Sound transmission

Sound intensity (I) is defined as the power per unit area (W/m), or the rate of energy flow per unit area. Figure 23 shows a sound source originating from the left reference point with an acoustical signal intensity of I_0 radiating uniformly into free space. Following the law of conservation of energy, a ¼ of I_0 will pass through the 1 m^2 area at 10 m compared to the 4 m^2 at 20 m. The relationship between the intensity and distance in a free sound field is known as the inverse square law (Eargle, 2005).

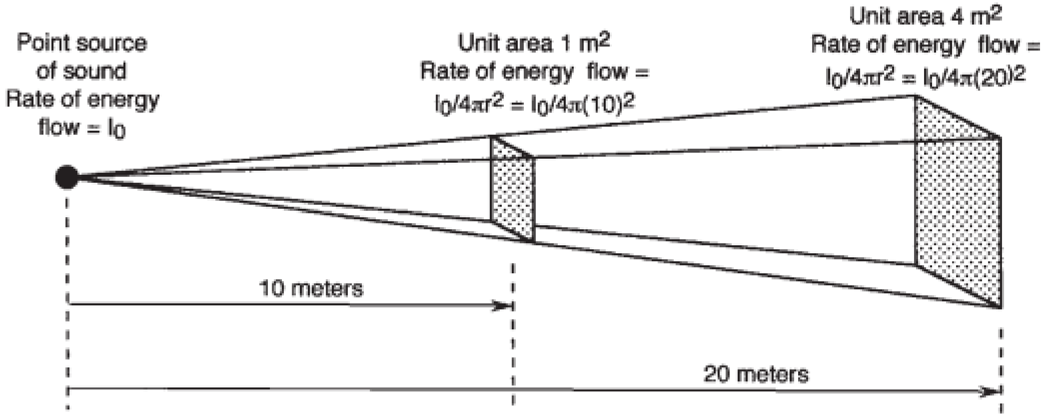

Figure 23: Sound intensity variation with distance over a fixed solid angle (Eargle, 2005)

The intensity at any distance r from a sound source in (W/m^2), where W is the acoustical power of the signal, is expressed by Equation 1 below.

$$I = W/4\pi r^2 \ldots\ldots\ldots\ldots\ldots\ldots\ldots\ldots\ldots\ldots\ldots\ldots\ldots \textit{Equation 1}$$

The effective sound pressure in pascals at that distance is expressed by Equation 2, where p_0c is the specific acoustical impedance of air (405 rayls).

$$P = \sqrt{I_{p_0 c}} \ \ldots\ldots\ldots\ldots\ldots\ldots\ldots\ldots\ldots\ldots\ldots\ldots\ldots \textit{Equation 2}$$

Normally, the acoustical intensity of a sound source is not measured but the sound pressure level (SPL) is. Acoustic pressures encountered in daily life normally vary from 20µPa to 100Pa. Equation 3 shows the relationship between the SPL measured in Pa and dB where the reference value p_0 is 20 µPa (Eargle, 2005).

$$Level\ dB = 10\ log(p/p_0)^2 = 20\ log(p/p_0) \ldots\ldots\ldots \textit{Equation 3}$$

The relationship between the speed of sound (m/s), wavelength (m), and frequency (1/s) is shown by Equation 4 below:

$$c\ (speed) = f\ (frequency) \times \lambda\ (wavelength) \ldots\ldots\ldots \textit{Equation 4}$$

2.6.2. Microphones

A microphone is a device that converts sound waves into electrical signals that can be amplified as analog signals or converted to digital signals which can then be processed by computers and digital audio devices (TechTerms, 2022). A condenser-type microphone is typically used for the audio recording in industrial applications such as architectural acoustics, and acoustical response and noise measurement in industrial workplaces, as shown in Figure 24. These microphones are well known for their sensitivity and flat frequency response.

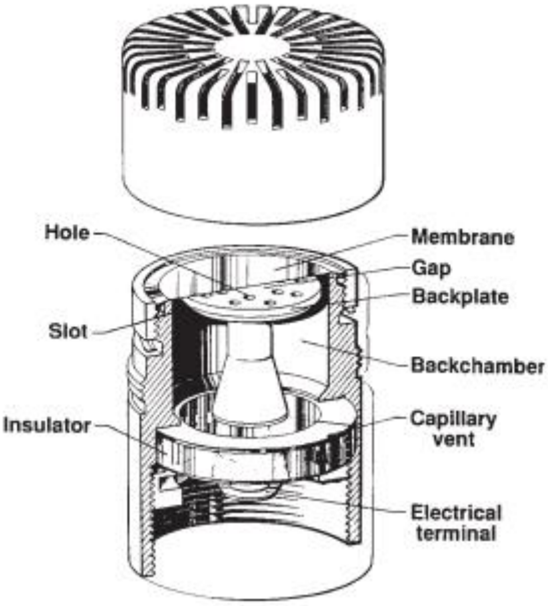

Figure 24: Cross-sectional view of a condenser microphone components (Brüel and Kjær, 1977)

To choose an appropriate microphone for the specific application field, the sensitivity of the microphone and the microphone's response field must be considered (National Instruments Corporation., 2022). There are three main types of microphones: the pressure-field, the random-incidence, and the free-field microphone, the latter being the most used.

The pressure-field microphone, shown in Figure 25(a), measures the pressure in front of the diaphragm and is normally used in enclosures or cavities with small openings in applications such as airplane wings or inside of structures. A free-field microphone, shown in Figure 25(b), measures the sound pressure from a single source directly at the diaphragm of the microphone, and the sound pressure is measured as it is emitted from the source. Applications of this type of microphone can be found in open areas which are free of hard or reflective surfaces. A random-incidence microphone, shown in Figure 25(c), is used to measure sound, which is not emitted from a single source, and responds uniformly to sounds arriving simultaneously from all angles. The applications of this type of microphone can be found in churches, or areas with hard and reflective walls (National Instruments Corporation, 2022).

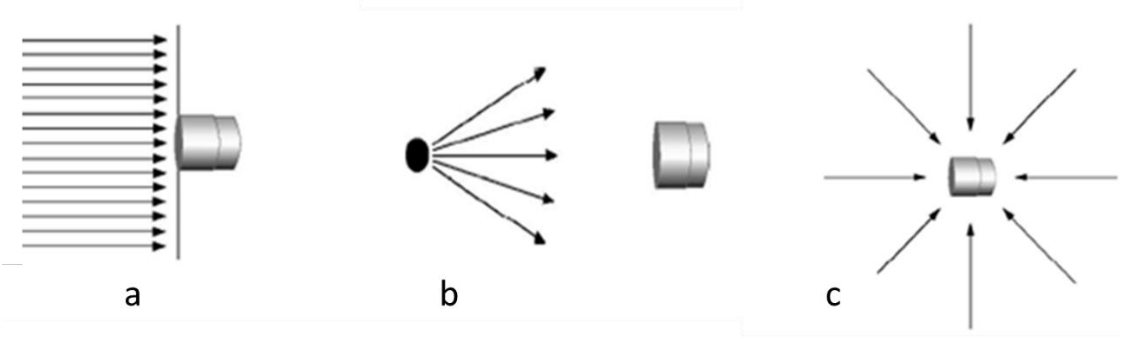

Figure 25: (a) Pressure-field, (b) free-field, (c) and random-incidence microphone schematic (National Instruments Corporation, 2022)

The microphone sensitivity is the ratio between the analog/digital output value to the input pressure and is generally measured with a 1kHz sine wave at a 94dB sound pressure level (Lewis, 2012). An analog microphone sensitivity is expressed in logarithmic units of dBV, as shown in Equation 5, which expresses how many volts the output signal will be for a given SPL.

$$Sensitivity_{dBV} = 20 \times log_{10} \left(\frac{Sensitivity_{\ mV/Pa}}{Output_{AREF}}\right) \ldots\ldots\ldots\ldots \text{ Equation 5}$$

2.6.3. Data acquisition

Data Acquisition (DAQ) systems convert analog signals from sensors to digital signals and vice versa. They acquire and sample signals for a broad range of measurement applications, from pressure measurement to acceleration and sound sampling (Dewesoft, 2022).

DAQ system sensors come in numerous shapes, sizes, and specifications. They connect the measured physical phenomena to the signal conditioner’s input. Signal conditioners generally compensate for nonlinear responses caused by noise disturbances from environmental factors by amplifying, filtering, and isolating the signal.

One of the important parameters at the signal converter input is the frequency at which the DAQ system samples the incoming signal. The sampling frequency determines how often a measurement takes place, where sampling a signal too slowly can result in an aliased signal. In Figure 26, the inadequately sampled signal appears to have a lower frequency than the actual signal, indicating two cycles instead of ten cycles of the original signal. An aliased signal provides a poor representation of the actual signal, causing a false lower-frequency component to appear in the signal (National Instruments Corporation, 2022).

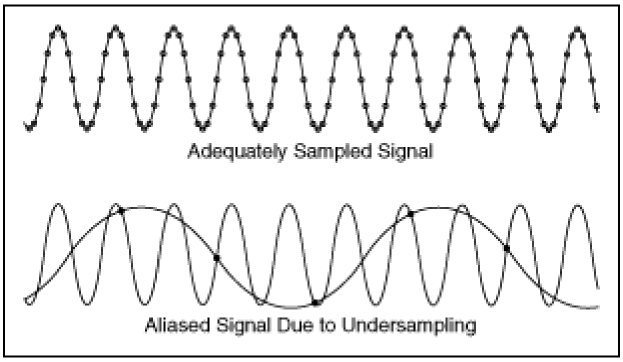

Figure 26: Adequately sampled signal (top) and an inadequately sampled signal resulting in aliasing (bottom) (National Instruments Corporation, 2022)

Increasing the sampling frequency increases the number of data points acquired in a given time period. Often, a fast-sampling frequency provides a better representation of the original signal at increased equipment cost and higher data rates. For a given sampling frequency, the minimum sampling frequency required to accurately represent the signal without aliasing is called the Nyquist frequency and equals one-half the sampling frequency, as shown in Equation 6.

$$f_N = \frac{f_S}{2} \ldots\ldots\ldots\ldots\ldots\ldots\ldots\ldots\ldots\ldots\ldots\ldots\ldots. \textit{ Equation 6}$$

- where f_N is the Nyquist frequency, and f_S is the sampling frequency.

2.6.4. Acoustic emission testing

The capabilities of acoustic-based monitoring to identify welding defects, such as phase transformation, crack formations, and surface defects, have been indicated in previous studies (Jolly, 1969; Sun et al., 1999). In modern-day industry, AE is used as an online monitoring tool to monitor the health of industrial equipment such as bearings in production lines, pipes and pressure vessels, and structures which are subjected to loading for certain defects like stress corrosion cracking. AE has been shown to be more sensitive in detecting crack growth compared to ultrasonic and X-ray testing (Boyes et al., 2009).

The two methods which are generally used to record AE signals are transient and continuous. For transient analysis, only the AE signals which exceed a set amplitude threshold are captured and used to assess the service condition of the monitored body, and in the latter, the entire AE signal within a certain duration is captured and analysed. In Figure 27, an example of a time-domain signal with its features can be seen. A high amplitude, above a set threshold in the signal, can indicate that a defect has occurred in the region. Factors such as the rise time, duration and number of AE events can also be used to identify and characterise the defects (Ghayoomi et al., 2021).

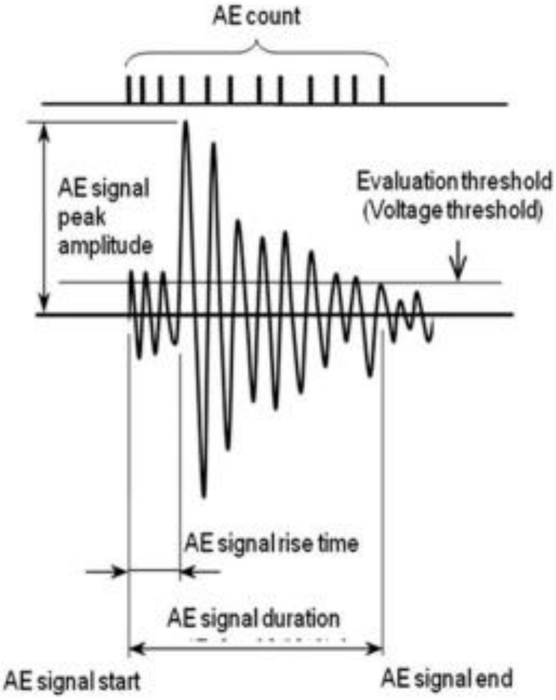

Figure 27: Time-domain AE signal features (Ghayoomi et al., 2021)

The ability of AE monitoring to detect and differentiate AE events within a recorded signal is promising. Similar to the AE during the welding process, AE during L-PBF can be divided into gas- and structure-borne emissions originating from the stress waves induced by changes in the internal structure of the part being processed (Figure 28). AE has also been seen to have a high signal-to-noise ratio and fast response.

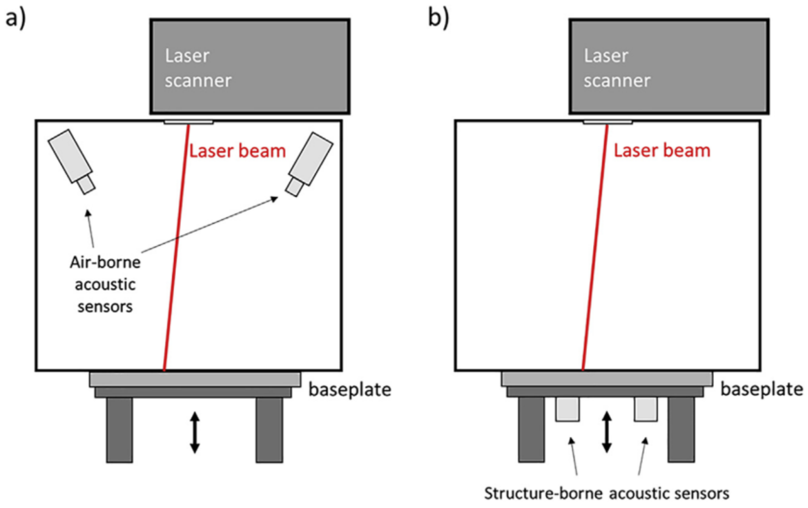

Figure 28: Examples of air-borne (a) and structure-borne (b) acoustic sensor mounting on L-PBF systems (Yadroitsev et al., 2021)

Structure-borne AE

Structure-borne AE monitoring refers to an AE monitoring technique where an AE sensor is attached directly to the body of the object to monitor the elastic stress waves emitted by the object and is generally used for defect analysis. The AE sensors operate by converting the elastic stress waves (sound) through a transducer into an electrical signal, as shown in Figure 29. The transducers are classified according to their principle of operation (chemical, mutual induction, and piezoelectric transducers).

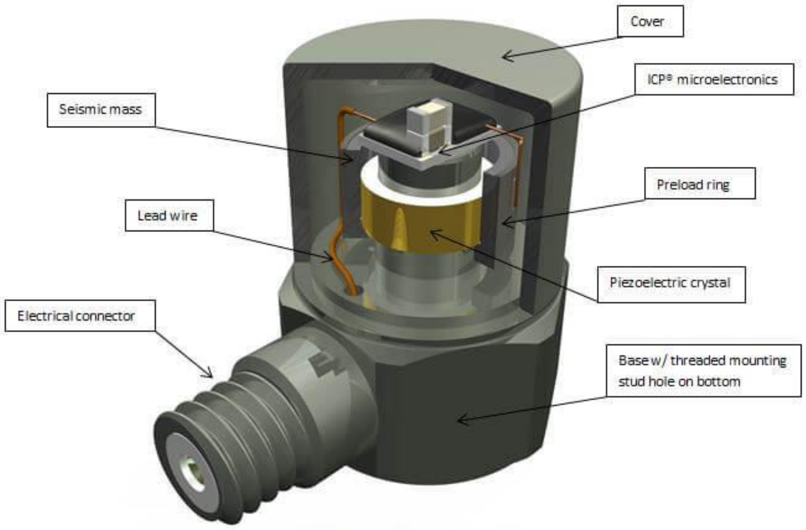

Figure 29: Schematic of structure-borne piezoelectric ICP accelerometer AE sensor (PCB Piezotronics., 2023)

Strantza et al. (2017) used two AE sensors to determine crack growth in notched and unnotched specimens during a four-point bending test. The crack location was determined based on the time delay between the two registered AE signals and the velocity of the wave in the material.

Figure 30 shows the AE events localisation within the specimen's specified length at the different cyclic loading intervals. The AE events clearly indicate the crack location and propagation with the increase in peaks at the centre of the notched specimen.

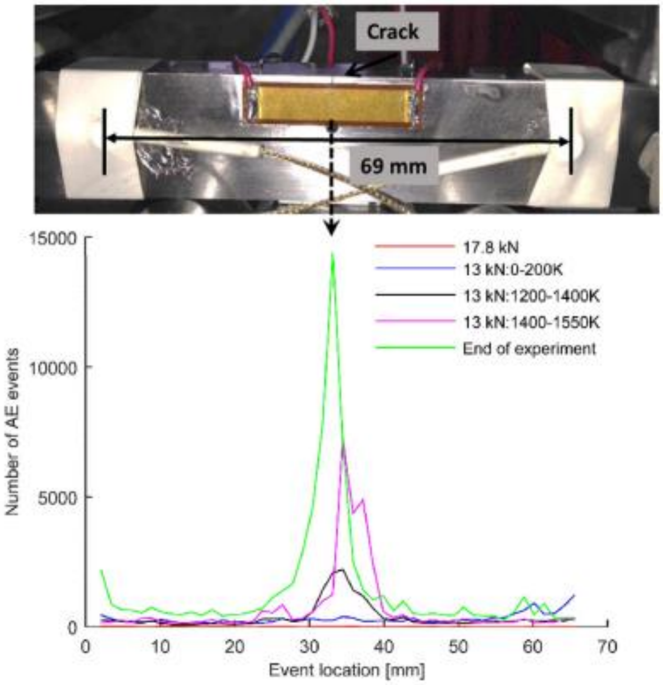

Figure 30: AE events vs location during fatigue crack propagation (Strantza et al., 2017)

Eschner et al. (2018) attached a piezoelectric transducer to the bottom of an L-PBF build plate and investigated the quality levels of different cubes built with varying process parameters and found that the AE method used to monitor the build process yielded results within 76–86% accuracy. Similarly, Seleznev et al. (2022) used a high-frequency structure-borne AE sensor to monitor for cracks during the L-PBF process with a set detection threshold and found that even though there was a lot of noise within the signal due to AE signals, such as the recirculating fan operating, it was still possible to distinguish the AE events related to cracking and noise within the signal.

Although structure-borne AE sensors have proved promising in monitoring the L-PBF process in the literature, they pose two limiting factors. The sensors must be attached directly to the test specimen to be monitored, and they are location-sensitive, meaning that if they are placed at a non-optimal location with respect to the AE event, some desired AE signals may not be detected.

Gas-borne AE

In gas-borne AE monitoring, the elastic stress waves (sound), which are emitted by the monitored object, travel through a medium (air) and are measured with an AE sensor such as a microphone. The possibilities of gas-borne AE to monitor the L-PBF process have been indicated in recent studies, such as the use of a fibre Bragg grating AE sensor, which was utilised by Wasmer et al. (2017). The sensor was placed at the internal wall of the build chamber and used to identify the gas-borne AE signals. Similarly, Kouprianoff et al. (2018) used a microphone to identify balling effects in single tracks of maraging steel. The signal was filtered to remove the effect of ambient operating noise that does not pertain to the actual laser scanning. The entire signal of the process for the optimal scanned tracks in the time domain before filtering and processing is shown in Figure 31 (left), which consists of machine noise from the L-PBF process. The time-domain signal of the filtered and processed signal is shown in Figure 31 (right) and clearly distinguishes the three different tracks, T1 to T3. Kouprianoff et al. (2021) also investigated different AE signals during various L-PBF operating process modes using an ICP microphone, finding that an inverse relationship existed between the sound pressure level and the contact zone, which is the interaction area between the laser and the powder bed.

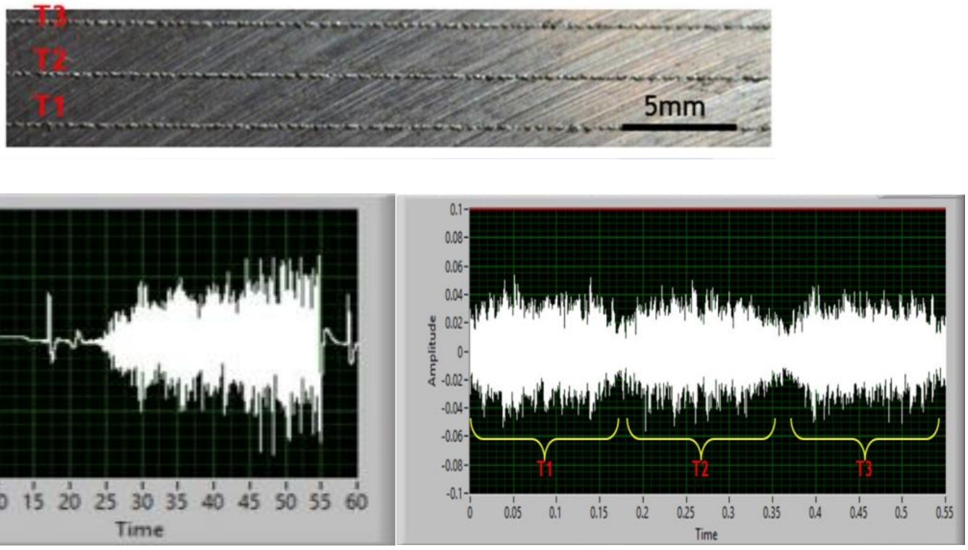

Figure 31: Time-domain AE signal from EOS M280, unfiltered (left) and filtered signal (right) (Kouprianoff et al., 2018)

The use of gas-borne AE monitoring for in situ detection of defects such as cracks, pores, balling and keyhole phenomena during metal AM and other similar AM methods has been investigated by other authors in the literature. Tempelman et al. (2022) successfully used a microphone to monitor for signals which correlated with pore and keyhole formation during the L-PBF process; the location of the pores was identified by the recorded time series of the laser position and acoustic pressure of the AE signals. Chen et al. (2023) also used a similar method with a microphone during a laser direct energy deposition manufacturing process to monitor for defects. In both cases, the challenge was retrieving the desired signal from the background noise in the raw signal. The Fast Fourier Transform and other signal processing methods had to be applied to retrieve the desired signals.

The advantage of using gas-borne AE sensors is that no physical contact is required with the measured object. A possible disadvantage of using the AE sensor is that it can be difficult to retrieve the desired signal from the background noise. For crack detection in an L-PBF process, AE could be used by filtering the noise signals and analysing the amplitude in the time domain with similar methods described above.

Machine-learning-based methods for AE

Machine learning (ML) is regarded as a subset of artificial intelligence and computer sciences where the systems used are provided with the capacity to learn and improve themselves from experiences encountered, as humans would, with the aid of algorithms and historical data. These computerised systems provide solutions to complex problems with the use of predictable patterns based on the data provided. ML can be categorised into four methods namely supervised learning, unsupervised learning, semi-supervised learning, and reinforcement learning (TechTarget, 2023). The promising capabilities of integrating AE with ML for in situ monitoring were shown in the work of Wasmer et al. (2018). Ghayoomi et al. (2021) investigated several ML techniques for the purpose of online defect detection during the L-PBF process by using AE. Three ML approaches were used, the first being the hierarchal K-Means clustering method, which was used to train the deep learning classifier to detect and label specific L-PBF defects using the unsupervised learning method. The results obtained using the method showed a success rate of above 90%. The second approach included the supervised learning method where the principal component analysis gaussian mixture model (PCA-GMM) was used as an alternative simple and fast ML approach for defect detection. The last approach included the variational auto-encoder method which was used to obtain the general signal features to be used as the input variables for the classifier. In similar work, Ye et al. (2018) also used a variety of ML algorithms to classify various AE signals during the L-PBF process by using the time and frequency domain features of the signal and to classify the AE signatures of 316L samples built using L-PBF. The frequency domain features of the AE signal were used by Eschner et al. (2020) as an input to the artificial neural network algorithm. The work of Fu et al. (2022) includes detailed applications, specifications, and accuracy levels for various ML algorithms used to monitor defects in metal AM.

CHAPTER 3: MATERIAL AND METHODS

3.1. Introduction

The objective of the current work is to investigate the L-PBF cracks caused by residual stresses during the build process by using AE online monitoring techniques. The experiments were conducted as shown below and divided into two parts:

- In the first experiment, it is shown how the sample referred to as the "cracking sample" was designed and developed to record the cracking sounds produced by the sample as it failed during the build process.
- In the second experiment, the AE monitoring and analysis of the cracks produced by the "cracking sample" was conducted.

3.1.1. L-PBF processing

The EOS M290 metal L-PBF machine using a Yb fibre laser was used to conduct the first part of the experiments, which included the build and validation of the "cracking cantilever" designed to fail in situ. The EOS M280, which is the predecessor of the EOS M290, was used for the second part of the experiments, which included the AE analysis of the cracks. The M280 is a machine dedicated for research purposes at the CRPM facilities and has open process parameters settings. Standard pre-set EOS material process parameters for Ti6Al4V (ELI) were used for the first and second experiments (where a total number of 8 cantilever specimen were manufactured for all experiments, with 4 specimen used for the validation phase, and the other 4 specimen used for the AE monitoring phase). On the EOS M280, a build volume reduction module with build dimensions length and width 50 x 50 mm was used, as shown in Figure 32. For manufacturing the cantilever specimen in an argon gas atmosphere, a 170 W laser power, 1.25 m/s scanning speed, 80 µm laser spot size and a back-and-forth scanning strategy using strips (5 mm) with a hatch distance of 100 µm and a 40 µm powder layer thickness was applied

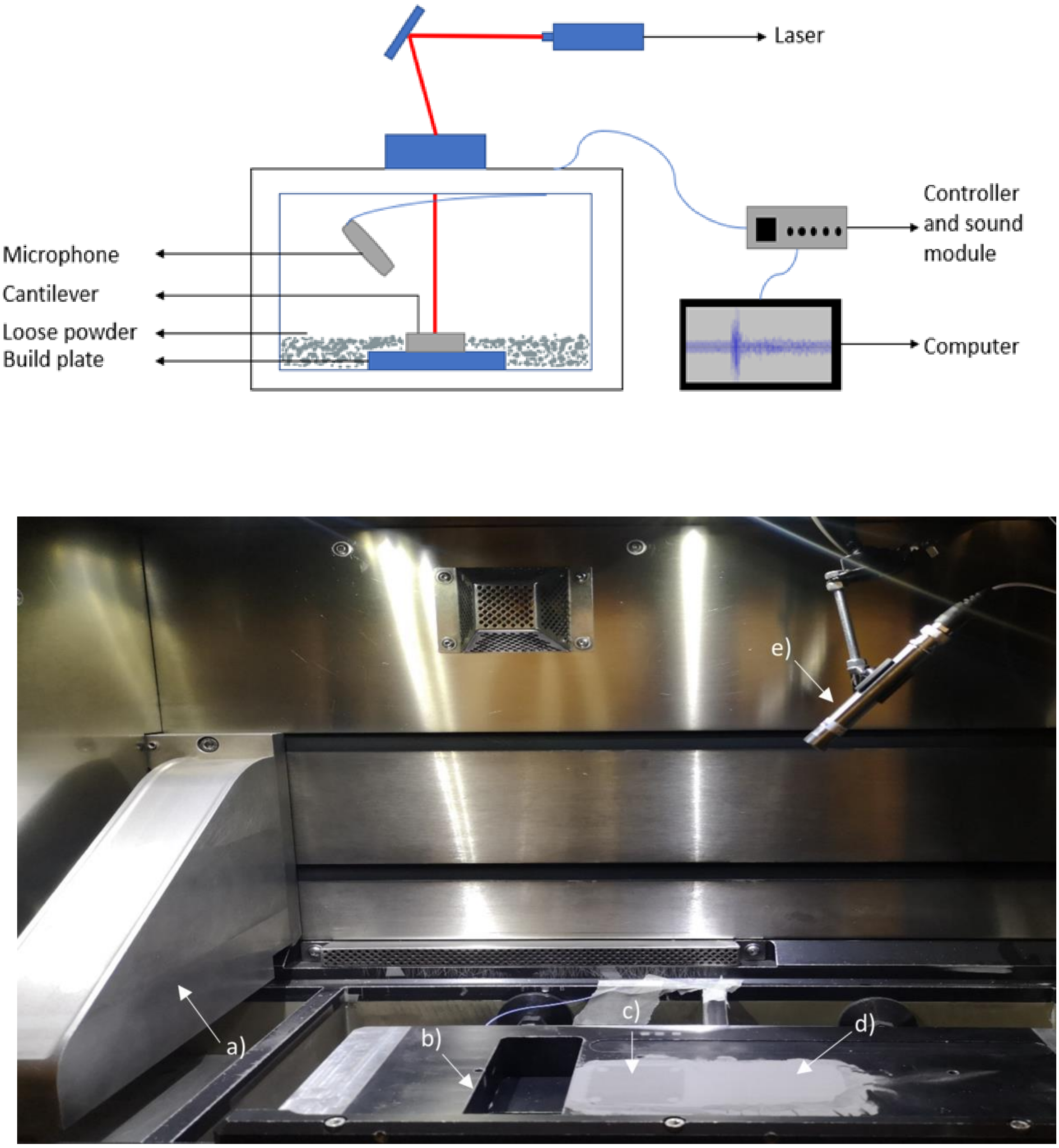

Figure 32: Schematic of experimental setup (top) and M280 chamber with reduced build volume (bottom): recoater arm (a), powder collector (b), build platform (c), powder dispenser (d), and ICP microphone (e)

To validate the designed cracking cantilever sample (Figure 33), two identical cantilevers were built next to each other on the same build plate, where the samples were visually monitored during processing. After failure was observed when the powder was being dispersed at the tip of the samples, the building process was stopped. For the purpose of repeatability, another build was performed with two more identical samples on the same build plate.

A similar experimental setup was conducted for the AE testing phase of the experiments. The only difference in the setup was the addition of an acoustic sensor where an ICP microphone was placed in the building chamber, pointing directly at the centre of the build plate to record the gas-borne AE signals of the building process. The DAQ equipment was externally connected to the microphone, as shown in Figure 32.

3.1.2. Ti6Al4V (ELI) powder

All the cracking cantilever specimens were manufactured using titanium Ti6Al4V(ELI) powder – a pre-alloyed gas-atomized powder with chemical composition (weight%): Ti – balance, Al – 6.34%, V – 3.94%, O – 0.082%, N – 0.006%, H – 0.001%, Fe – 0.25%, C – 0.006%. The equivalent diameters, as weighed by volume of the spherical powder particles for the 10th, 50th and 90th percentiles, were d_{10} = 21.9 µm, d_{50} = 31.9 µm, and d_{90} = 48.8 µm, respectively.

3.2. Design of cracking cantilever sample and numerical simulations

The geometry (shape, height and width) of the designed cracking cantilever sample was determined based on the localised rapid heating and cooling thermal cycles of the L-PBF process from literature, which induce tensile and compressive stresses during the build process. The overall design of the shape was based on a cantilever sample that is cut post-process to measure the deflection caused by the residual stresses, as seen in previous studies (Zaeh et al., 2010; Kruth et al., 2012; Papadakis et al., 2014; van Zyl et al., 2016*)*.

The attachment points, which are numbered in Figure 33, were designed with the expectation that the first strut (1) would fail due to exceeded stresses and strains. The shaded area of the cantilever was designed to prompt the build-up of residual stresses. The expected deflection due to the failure of the struts before the simulations is also shown in Figure 33. The height (h) was varied to determine the failure height of the designed cracking cantilever sample from the simulations, as the literature found that as the height of a sample increases, so do the residual stresses.

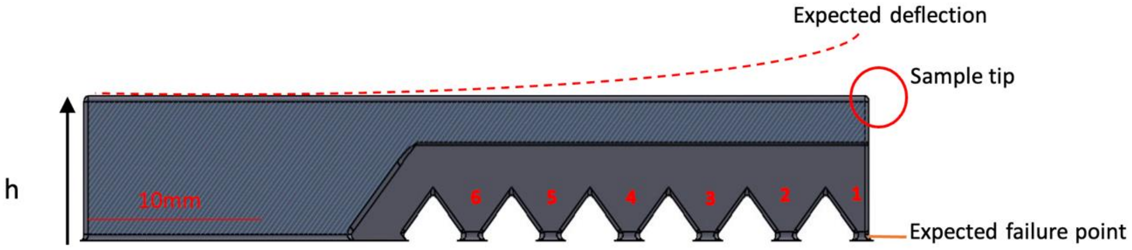

Figure 33: CAD design of cantilever with strut numbers

The initial height of the cracking cantilever sample was chosen with the intent to save as much material as possible in a sample that would fail in a reasonable time for the purpose of in situ monitoring while also keeping in mind to prompt the build-up of residual stresses within the layers.

The CAD model of the cracking cantilever sample was designed using SolidWorks 2021. Its length and width were 45 mm and 5 mm, respectively. Eight different CAD models with 0.25 mm increments from a height (h) of 4 mm to 6 mm were modelled to determine the failure height from the numerical simulations.

The eight CAD models were converted to STEP files and simulated using the inherent strain method with Simufact Additive 2020 to determine the possible failure height based on the resulting stresses and strains. Simufact Additive is a scalable simulation software for metal-based AM designed to predict and compensate for distortion, residual stresses, and temperature distributions digitally during the build before the part is physically manufactured. For the accuracy of the simulations, three traditional cantilevers were built on the EOS M290 (using standard EOS Ti6Al4V (ELI) M290 material process parameters) and cut in the as-built condition and the deflections measured to calibrate the inherent strains. A voxel size of 0.25 mm was used for both the simulations and calibrations. The cracking sample’s design was then modified based on simulation results so that the upward curling of the designed cantilever would tend to break at the attachment points.

3.3. Acoustic emission testing

3.3.1. AE monitoring

The AE testing phase of the experiments was conducted using the EOSINT M280 L-PBF machine with pre-assigned EOS Ti6Al4V(ELI) powder process parameters and a 30 µm layer thickness. A model 378B02 ICP microphone with an optimal frequency range of 3.75–20 000 Hz (± 2dB) was placed 240 mm above the substrate in the build chamber pointing directly at the centre of the build plate, as seen in Figure 32**.** A NI9250 DAQ soundcard and LabVIEW 2022 software were used to record and analyse the gas-borne AE signals during the build process of the cracking cantilever sample designed to fail in situ (Moore et al., 2022). The cantilevers were built on a reduced grade 5 Ti build plate with dimensions of length and width 50 x 50 mm. A sampling frequency of 102.4 kHz was used to acquire the AE data , as this frequency was indicated to be in accordance with the Nyquist criterion (Kouprianoff et al., 2021).

3.3.2. AE from machine noise

The build chamber of the EOS M280 with the reduction unit is shown in Figure 32. To characterise the AE signals emitted by the machine, various AE recordings from different AE sources within the build chamber were conducted and categorised as noise, such as that of the laser scanning and the recirculating fan running. The noise signals time-domain features, such as the root mean square (RMS), peak amplitude, and signal-to-noise ratio (SNR), were analysed. The SNR ratio for the noise signals was between the filtered RMS as the desired signal and the unfiltered RMS as the noise signal, shown in Equation 7. The SNR was then expressed in decibels, as shown in Equation 8.

$$SNR_{voltage} = \frac{RMS_{signal\ voltage}}{RMS_{noise\ voltage}} \ldots\ldots\ldots\ldots\ldots\ldots\ldots\ldots \textit{Equation 7}$$

And $SNR_{dB} = 20\ log_{10}(SNR_{voltage})$ .... *Equation 8*

Appendix A1 contains the noise signals respective frequency and time-domain responses before and after applying the 2kHz high-pass filter. Data from the AE recordings of (1) the machine in idle, (2) the powder dispenser moved down by 0.05µm, (3) the flooding valve opening, (4) the machine flooding, (5) the flooding valve closing, (6) the build platform moved down by 1 mm, (7) the build platform moved up by 1mm, (8) the recoater arm moved left, (9) the recoater arm moved right, (10) the recirculating fan running, (11) the laser scanning, and the occurrence of the cracks on each cantilever specimen where (12) the laser was scanning with the occurrence of crack(s), and (13) where there was an event where the occurrence of the crack(s) only, were analysed.

3.3.3. AE from cracks of designed cracking cantilever samples

To investigate the capabilities of the AE equipment to detect the cracking during the build process, four cracking cantilever samples were placed at the centre of the build plate, as shown in Figure 34. The expected failure tip in Figure 33 of the cantilever specimen was placed facing opposite the recoater arm direction to avoid damage to the recoater when the specimen failed with the build plate. The entire build process was recorded until all four specimens had failed with the build plate, which was indicated by powder being dispersed at the tip of the specimen and the failure height noted (as from the machine current layer height). The cool-down process was also recorded after the build process had been stopped. Only two cracks were considered per cantilever specimen: the crack which occurred during the build stages of the cantilever when the laser was scanning and the recirculating fan was operating, and the crack which occurred when the build process had been stopped in the cool-down phase of the cantilevers when the laser was not scanning, and the recirculating fan was not operating. The occurrence of these cracks was then labelled according to the specimen number and sequence of the cracks. i.e. (crack-S1-C2 denotes the second crack which had occurred in specimen 1). Both the time and frequency domain features of the signal were analysed, where a 2 kHz high-pass filter was applied to filter out some of the machine noise (Kouprianoff et al., 2021).

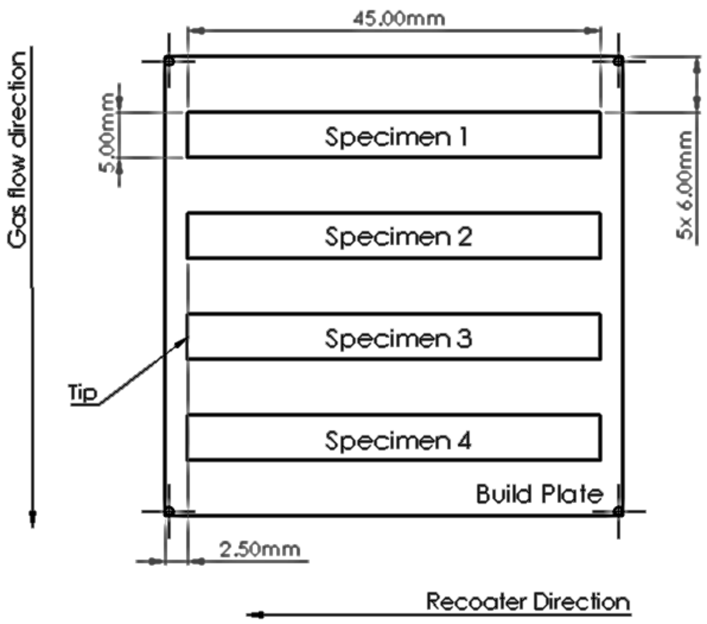

Figure 34: Build plate setup of cantilevers

CHAPTER 4: RESULTS AND DISCUSSION

4.1. Cracking sample: numerical simulations and experimental validation

4.1.1. Numerical simulations

As described in the materials and methods section in Chapter 3, eight different sample heights of the designed cracking cantilever sample were simulated to determine the possible failure height. The tensile material properties, such as the yield stress, ultimate tensile strength (UTS) and elongation of the sample in the as-built condition, are shown in Table 2. The table shows that for the first strut to fail completely with the build plate, an effective plastic strain of around 8% and equivalent stress of around 1 280 MPa would be required.

Table 2: Ti6Al4V tensile results (Kouprianoff and du Preez, 2023)

	Yield stress (MPa)	UTS (MPa)	Elongation (%)
As built material	1 198	1 282	7.7

The equivalent stress and effective plastic strain fields for the first strut of the initial three possible failure heights are shown in Figure 35. It can be seen from the figure that the effective stress of all three possible failure heights is above that of the material in the as-built condition, with a UTS of ~ 1 299 MPa when the sample failure height was 4.5 mm. Furthermore, the equivalent stress for the same failure height was found to be above that of the materials yield stress of ~ 1 120 MPa. The effective plastic strain of the first strut reached the strain at failure when the sample height was 4.75 mm, which is ~ 8% for the material in this condition. Considering the mechanical properties of the sample and the simulation results, failure of the first strut could be expected at a build height of around 4.5 mm.

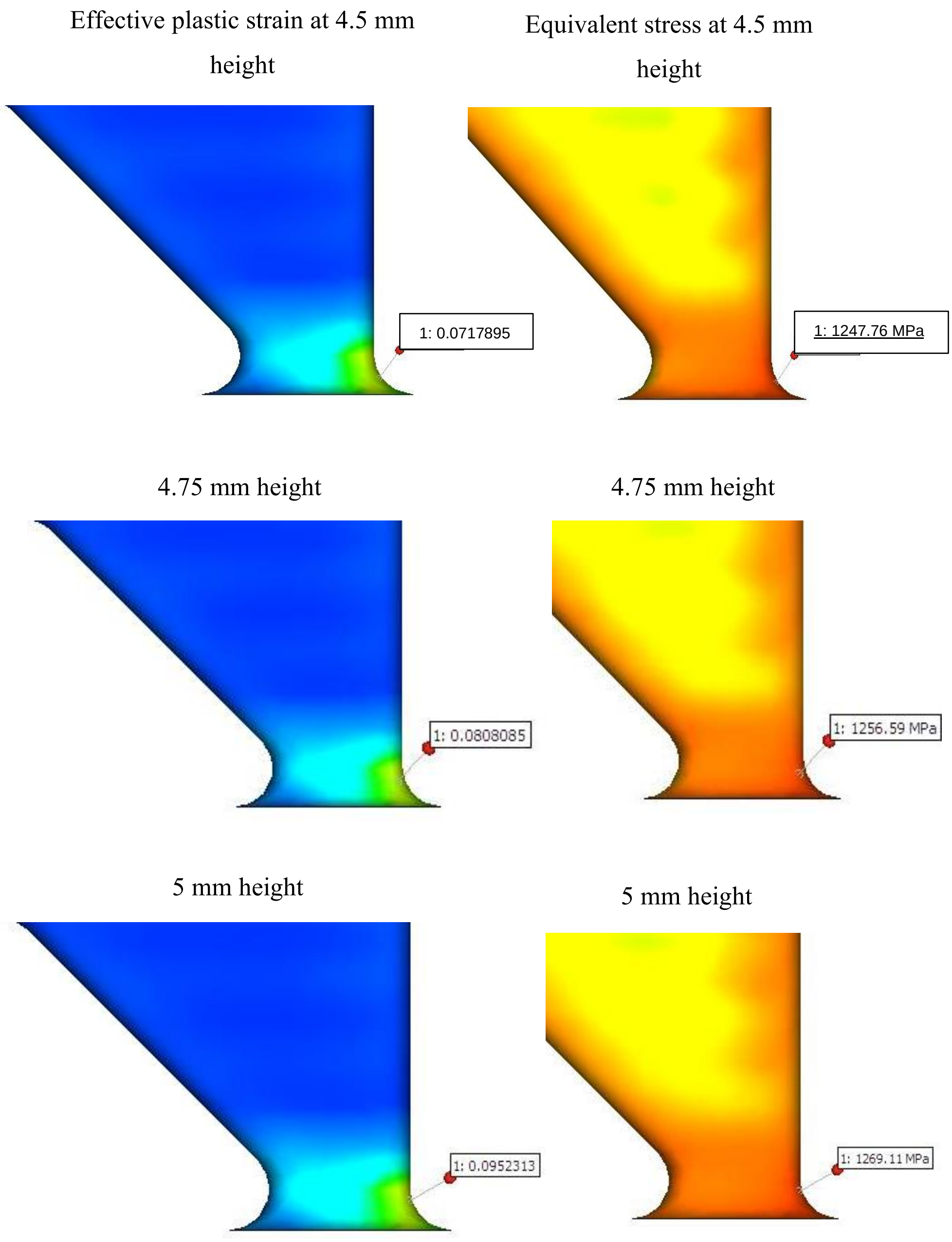

Figure 35: Effective plastic strain (left) and equivalent stress (right) at three possible failure heights for the first strut (see Figure 33)

4.1.2. Validation of cracking sample height

The two samples in the first build on the EOS M290 failed simultaneously at a height of 4.8mm. While interestingly, in the second build one sample failed at a height of 4.7 mm, while the second sample failed at a height of 5.3 mm. This deviation could be due to the gas flow dynamics in the chamber and slight cracking at the struts, which caused local plastic deformation and, in turn, a reduction in stresses or due to the thermal complexity of the L-PBF process. The sudden movement of the sample as it cracked disturbed the surrounding powder, as shown in Figure 36. The sample height at which this powder redistribution occurred was taken as the height at which failure had occurred. Both the manufactured and simulated samples proved that predictions were accurate, and a design height of ~ 6 mm would be sufficient to ensure the struts' failure.

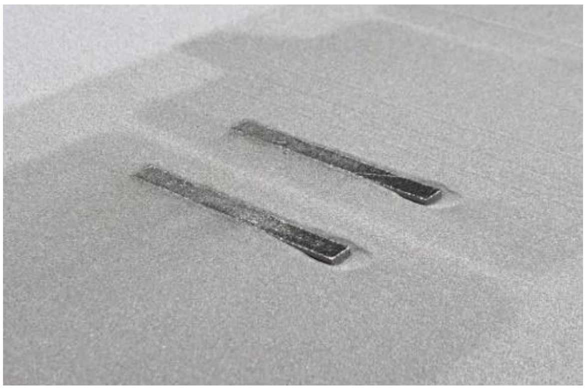

Figure 36: Ti6Al4V powder bed redistribution around tip of cantilevers after failure

The upward deflection of samples due to the failure at the interface between the struts and the base plate from the propagated cracks is shown in Figure 37. In the enlarged section of the struts (Figure 37 (b)), it can be seen that the last two struts (5 and 6) did not fail, although strut 5 does have propagated cracks (Figure 37 (c)).

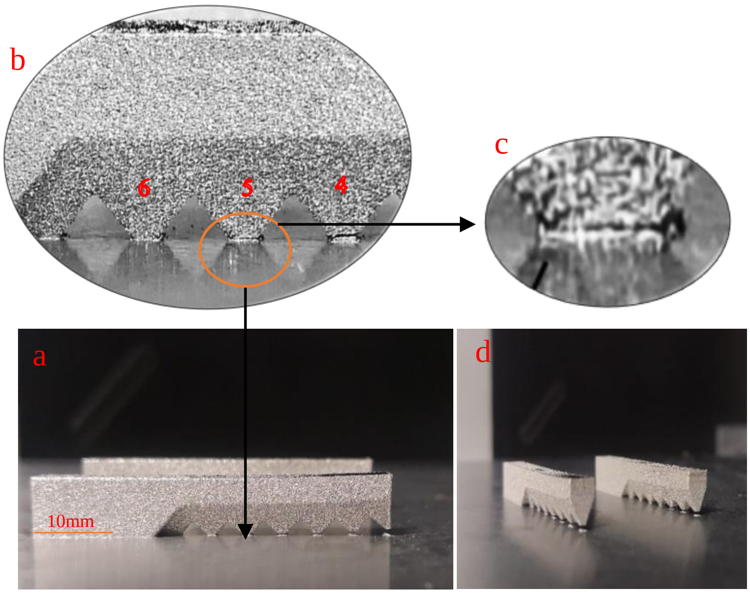

Figure 37: Strut failure and deflection

4.2. AE signals during L-PBF manufacturing

During the AE monitoring build phase of the cantilevers, four cracking samples were manufactured on the reduced build volume module of the EOS M280. The failure of the cracking samples with the build plate was visually observed and noticed by the powder being dispersed due to the progression of the cracks, and the failure layer height recorded (Figure 38). The samples failed twice during processing, once during the build process, and again during the cool-down phase after the build process had been stopped. Their respective frequency and time-domain responses before and after applying the 2 kHz high-pass filter can be found in Figure 44 and Figure 46.

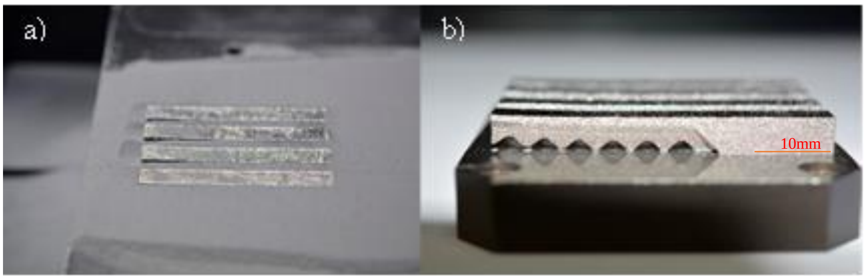

Figure 38: Powder bed after failure (a), side view of cracking sample after powder cleaning on the substrate (b)

An analysis was done of the cantilever crack signals of all four specimens during and after the build process had been stopped, i.e. recorded during the cool-down phase. Their respective initial failure heights during the build process are shown in Table 3. and were very similar, with the significant difference between the first and last failure being only five layers. Specimen 4 was the first sample to fail, initially at a height of 3.48 mm and then again during the build process at a height of 4.92 mm. The other three specimens' second failure was observed at a height of 5.19 mm during the cool-down phase after the build process had been stopped (Figure 39 on page 46). As a reminder, the cracks were labelled according to the specimen number and sequence of the cracks. i.e. (crack-S1-C2 denotes the second crack which had occurred in specimen 1).

Table 3: Cantilever failure heights

Specimen No.	Failure height (mm)	Failure layer
Specimen 1 (crack-S1-C1)	3.63	121
Specimen 2 (crack-S2-C1)	3.66	122
Specimen 3 (crack-S3-C1)	3.54	118
Specimen 4 (crack-S4-C1)	3.48	116

4.2.1 Introduction to L-PBF AE results

The extracted segments for the last two layers of the AE recording in the time domain are shown in Figure 39(a). The corresponding STFT can be seen in Figure 39(b). The AE signals from the recoater arm movement, laser scanning, the recirculating fan running and the two cracks which occurred when the recirculating fan was off due to the build process being stopped, are shown and labelled. Looking at amplitudes of the signal in the time domain, the machine-related noise, such as the laser scanning, recoater arm movement and the recirculating fan running was difficult to identify and differentiate. The only noticeable AE signals in this domain were that of the recirculating fan switching off and the cantilever cracks (crack-S2-C2 and crack-S3-C2). The aforementioned cracks occurred when the laser was not scanning (cool-down phase), where the internal stresses were in excess of the yield and ultimate tensile strength of the L-PBF material.

When looking at the STFT of the extracted segment of the AE signals in Figure 39(b), the duration and frequency content of the recoater arm movement, laser scanning, recirculating fan on/off and the two cracks can clearly be seen and differentiated from each other in detail. The second-last layer was initiated by the recoater arm movement with frequencies ranging up to

35 kHz and lasting for a period of six seconds, followed by the laser scanning with slightly higher frequencies ranging up to 45 kHz and the process repeated for the last layer. The recirculating fan was constant throughout the entire build process until it switched off at approximately 33 seconds. Towards the end of the extracted segment of the signal, at approximately 46 seconds, the two cracks have frequencies ranging up to 47 kHz.

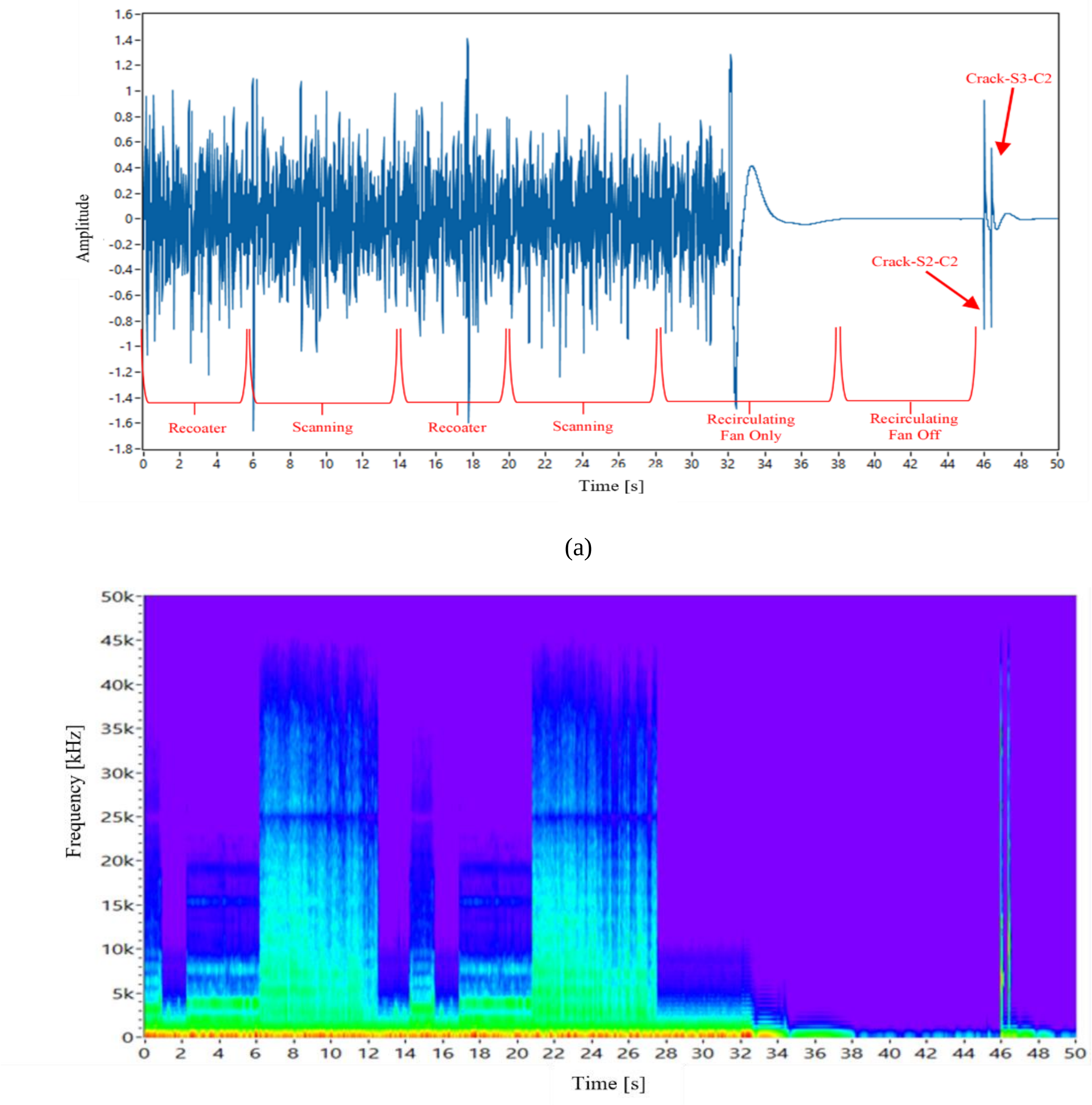

(a)

(b)

Figure 39 Amplitude-time graph (a) and frequency-time graph (b) of recorded AE signal

4.2.3. Frequency-domain AE features of machine noise

The FFT (fast Fourier transform) of the noise signals is shown in Figure 40 (left) where the frequency contents of the signals were analysed and used to apply an appropriate filter which would filter the undesired noise signals. The STFT (short-time Fourier transform) in Figure 40 (right), was used to indicate the occurrences of different events within the signal by analysing the respective frequencies with time.

a) Machine in idle	
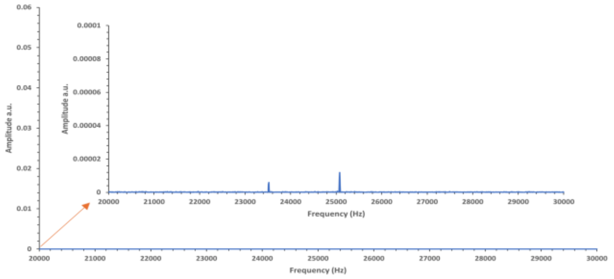	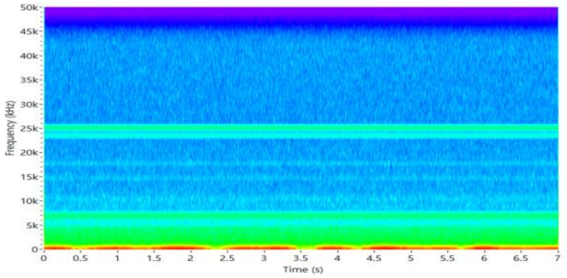
b) Inert gas flooding	
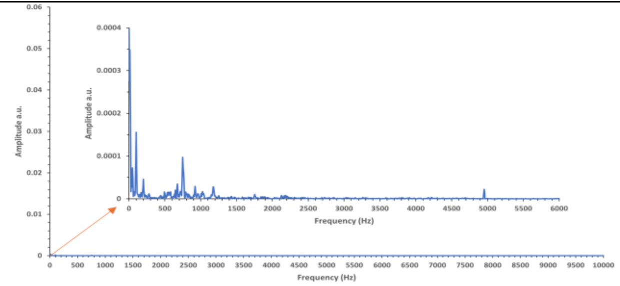	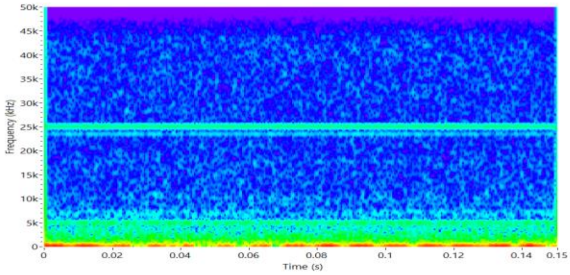
c) Recoater arm movement right	
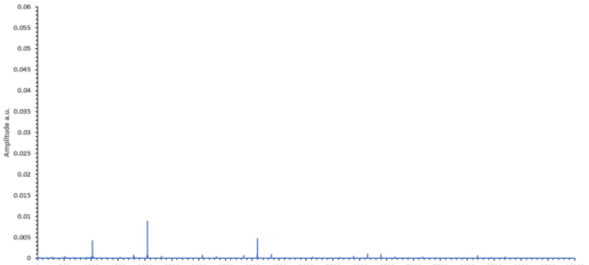	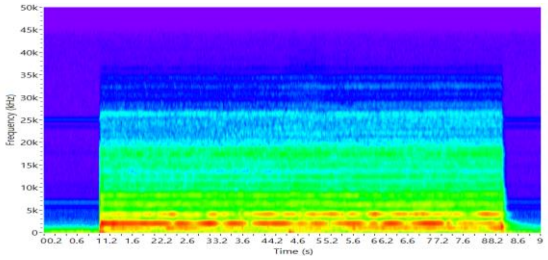
d) Recirculating fan	
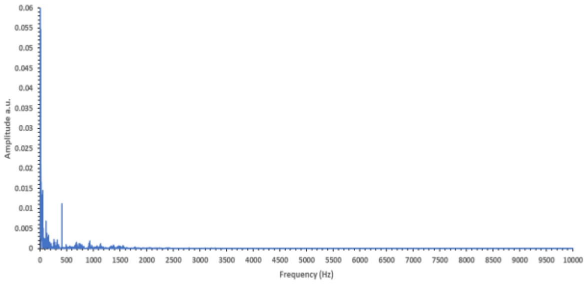	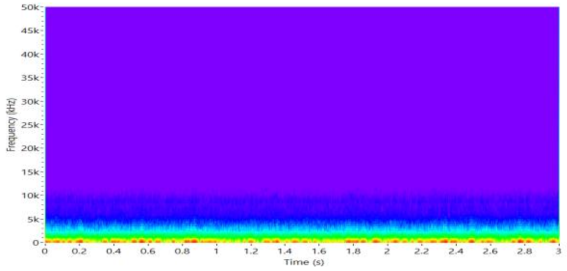

e) Laser scanning	
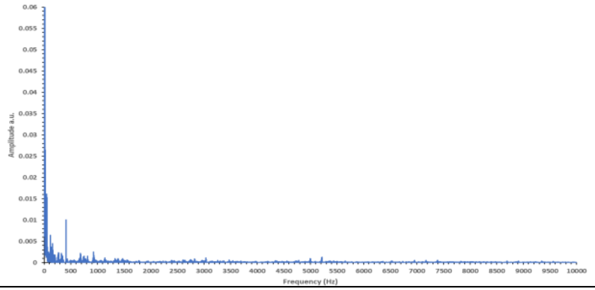	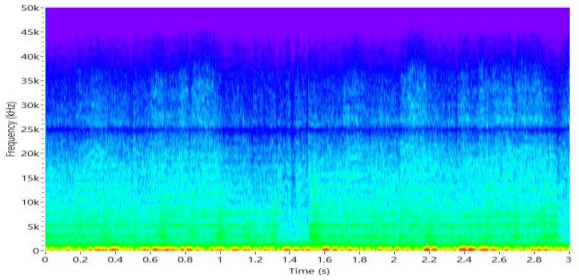

Figure 40: Unfiltered FFT (left) and STFT (right) of machine in idle (a), inert gas flooding (b), recoater arm movement (c), recirculating fan (d), and laser scanning (e)

Initially, the AE signal of the machine in idle was analysed where the FFT low-intensity frequencies were observed with a peak frequency of 25 kHz, as shown in Figure 40(a) (left). In the STFT of the same signal, these frequencies ranged from 0–25 kHz and were constant throughout the considered duration. When the machine was flooding, as in Figure 40(b), the same 25 kHz frequency was seen, although the peak frequency was now lower at 100 Hz, similar to the peak frequency when the flooding valve was opening and closing. The only noticeable difference between the flooding valve opening/closing signals and the flooding-only signal was a 750 Hz frequency that could possibly be attributed to when the argon gas was flowing through the build chamber. When the recoater arm was moved to the right, a peak frequency of 2 050 Hz was seen with its possible harmonic at 4 100 Hz in Figure 40(c) (left). The initial movement of the recoater arm can be seen in the STFT, which is initiated from the first second and lasts for 7.4 seconds, with the high-intensity frequencies being below 5 kHz and the other frequencies present within the signal ranging up to 38 kHz. When the recoater arm was moved in the opposite direction, similar frequencies were seen within the signal. The recirculating fan had a peak frequency of 413 Hz on the FFT in Figure 40(d) with the high-intensity frequencies being below 2 kHz on the STFT. When the laser was scanning, a peak frequency of 413 Hz was seen on the FFT of Figure 40 (e), which was similar to that of when the recirculating fan was running. Analysing the frequency contents of both signals, it was found that all the frequencies below 2 kHz were similar to that of when the recirculating fan was running. This indicated that the frequencies below 2 kHz while the laser was scanning could be attributed to that of the recirculating fan only, and frequencies above 2 kHz in the same signal could be attributed to that of the laser scanning only, ranging up to 47 kHz on the STFT.

When the build platform was moved up by a millimetre, a peak frequency of 215 Hz was seen on the FFT of Figure 41(a); this same frequency was also seen when the build platform was moved down by the same distance, although the intensity of the frequency had decreased by 33.3% in Figure 41(b). Looking at the STFT of when the build platform was moved upwards, a single movement of the build platform can be seen, which initiates at 0.48 seconds and lasts for approximately 0.5 seconds. In comparison with the single movement of the build platform in the latter case, when the build platform was moved down, two distinct movements can be seen in Figure 41(b), wherein the initial movement from 0.4–0.95 seconds, the build platform moves slightly past the set point, and then for the remainder of the signal, the build platform adjusts itself by moving upward to remove the slack from the motion screw.

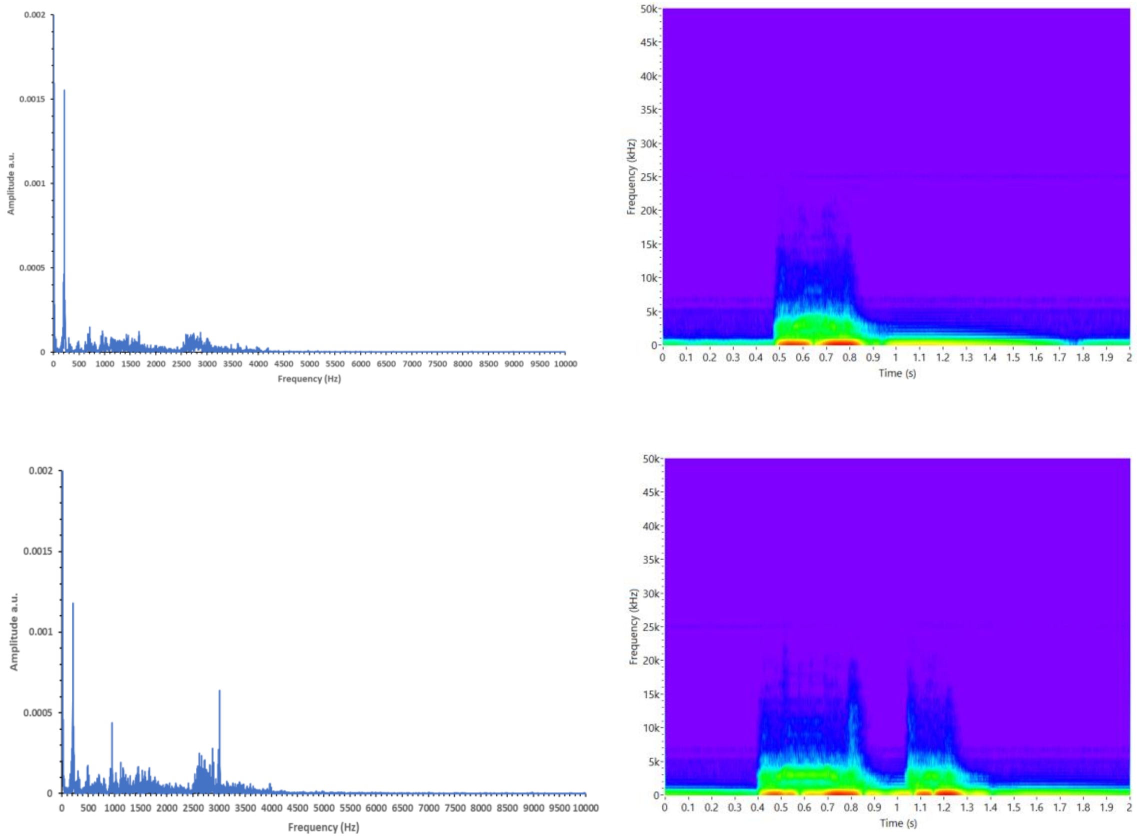

Figure 41: FFT (left) and unfiltered STFT (right) of build platform moved up by 1 mm (top), and the build platform moved down by 1mm (bottom)

In all the categorised machine-related noise signals, the peak frequencies did not exceed 2 kHz apart from the signals of the machine in idle, which had a very weak peak frequency of 25 kHz, and the recoater arm movement with a peak frequency of 2 050 kHz. Because of this, both these signals were considered to be possible signals of concern when monitoring for the cantilever cracks after applying a 2 kHz high-pass filter. However, after analysis of the intensities of the frequencies, it was found that due to the low intensity of the peak frequency of the machine in idle, the recoater arm movement would be the only possible signal of concern.

Table 4: Machine noise signals frequency response

Event	Peak frequencies from FFT	Occurrence from STFT
Machine in idle	25 000 Hz	Signal peak frequency constant throughout considered duration.
Inert gas flooding	100 Hz	Gas flow through build chamber indicated by high-intensity low frequencies.
Recoater arm movement right	2 050 Hz	Movement of the recoater arm occurred for a duration of 7.4 seconds.
Recirculating fan	413 Hz	Signal constant throughout considered duration with high presence of low frequencies.
Laser scanning	413 Hz	Frequencies below 2 kHz similar to that of the recirculating fan running.
Build platform moved up by 1 mm	215 Hz	Single movement of build platform observed with high-intensity low frequencies.
Build platform moved down by 1 mm	215 Hz	Double movement of build platform observed with high intensity low frequencies.

4.2.4. Time-domain AE features of machine noise

4.2.4.1. Root mean square (RMS) of machine noise signals

The RMS of the noise signals was analysed in the time domain before and after applying a 2 kHz high-pass filter and was used to indicate the average loudness of the signals. The RMS values in Table 5 show that before applying the high-pass filter, as expected, the machine in idle signal had the lowest RMS intensity, indicating that this signal would be the least loud of all. The signal of the recirculating fan running had an RMS intensity which was almost 270 times that of the machine in idle signal, being the loudest signal of all characterised noise signals within the machine build chamber. After applying a 2 kHz high-pass filter, the RMS value of the machine in idle signal dropped by 93.2% while that of the recirculating fan running decreased slightly more by 98.9%. This significant decrease in the RMS value of the recirculating fan now meant that the loudest noise signal in the build chamber after applying the high-pass filter was that of the recoater arm movement with an RMS value of 0.0165, followed by that of the laser scanning with an RMS value of 0.0164.

Table 5: RMS of noise and laser signals

AE Signal	Unfiltered noise signal RMS	Filtered noise signal RMS	Decrease in percentage of RMS
Machine in idle	0.0011	0.00003	97.3%
Dispenser moved down by 0.05 µm	0.014	0.0005	96.4%
Flooding valve opening	0.028	0.00005	99.8%
Build chamber flooding	0.0013	0.00005	96.2%
Flooding valve closing	0.0129	0.00004	99.7%
Build platform moved down by 1 mm	0.0415	0.0022	94.7%
Build platform moved up by 1 mm	0.0349	0.0012	64.5%
Recoater arm moved left	0.0221	0.0165	25.3%
Recoater arm moved right	0.0219	0.0158	27.8%
Recirculating fan	0.294	0.0031	98.9%
Laser scanning	0.2903	0.0164	94.4%

In all the characterised noise signals, the RMS value dropped by an average percentage decrease of 80.1% on the filtered signal, with the largest decrease in percentage being that of the flooding valve opening. This decrease in percentage indicated the effectiveness of the applied high-pass filter in filtering out the undesired noise.

4.2.4.2. Signal-to-noise ratio of the machine AE signals

The SNR (signal=filtered & noise=unfiltered) was similar to the percentage decrease of the RMS values after filtering; in this case, the SNR was used as a measure to indicate the effectiveness of the applied filter. Figure 42 indicates the various AE features of the noise signals, where all the characterised noise signals had a negative SNR. In general, a negative SNR ratio is undesirable as it indicates that the noise in the signal is greater than the desired signal itself, but in the current scenario, this outcome is actually desirable as it indicates that the 2 kHz high-pass filter was effective in filtering away the noise signals considering that the desired signal, in this instance, was actually the filtered noise signal.

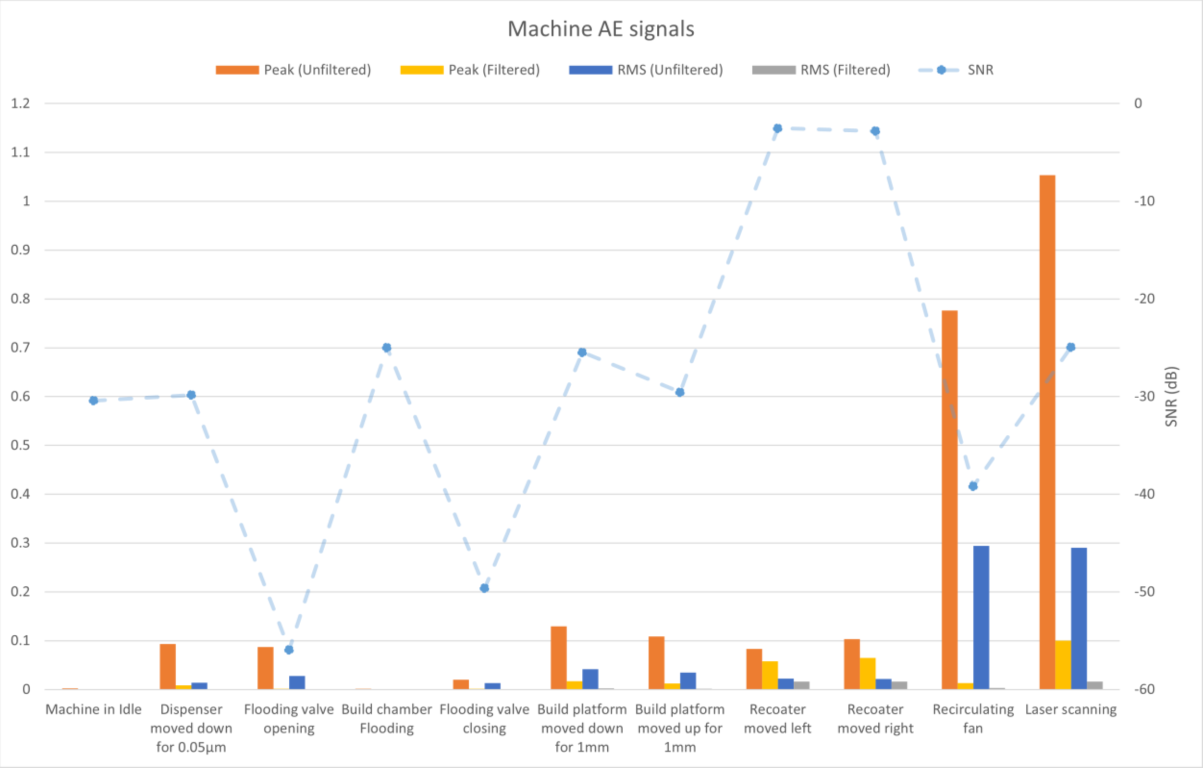

Figure 42: Peak voltage, RMS voltage and SNR of different L-PBF machine AE features

4.2.4.3. Peak amplitudes of machine noise signals

The peak voltage amplitudes in the time domain were analysed to assist in selecting an appropriate voltage threshold that would be able to distinguish the crack signals from that of the noise signals. In Table 6, various machine noise signals with their respective filtered and unfiltered peak amplitudes are shown. As expected, the unfiltered peak amplitude of the machine in idle signal was the least of all noise signals, although a high-peak frequency was present. The laser scanning signal had the highest peak amplitude of all the characterised noise signals before applying the 2 kHz high-pass filter. After applying the high-pass filter, the signal of the laser scanning was still found to have the highest peak amplitude, followed by the recoater arm movement. The lowest peak amplitude was that of the machine in idle, followed by the build chamber flooding. The average decrease in percentage of the peak amplitudes after applying the 2 kHz high-pass filter across all categorised noise signals was 77.5%. This decrease in percentage of the peak amplitudes also indicated the effectiveness of the applied filter.

Table 6: Peak amplitudes of the L-PBF machine AE signals

Noise Signal	Unfiltered noise signal peak amplitude (V)	Filtered noise signal peak amplitude (V)	Decrease in percentage of peak amplitude
Machine in idle	0.002	0.00015	93.2%
Dispenser moved down by 0.05 µm	0.093	0.0086	90.8%
Flooding valve opening	0.087	0.0012	98.6%
Build chamber flooding	0.002	0.0010	44.4%
Flooding valve closing	0.020	0.0014	93.1%
Build platform moved down by 1mm	0.130	0.0167	87.1%
Build platform moved up by 1 mm	0.108	0.0124	88.6%
Recoater arm moved left	0.084	0.0578	30.9%
Recoater arm moved right	0.103	0.0646	37.3%
Recirculating fan	0.776	0.0130	98.3%
Laser scanning	1.054	0.0999	90.5%

The raw waveforms of the loud signals are shown in Figure 43. The double movement of the build platform moving down can be seen in the time domain (Figure 43(b)), with the peak amplitude of the signal decreasing by 87.1% after applying the high-pass filter. The recoater arm movement in the unfiltered time domain (Figure 43(c)) starts its motion at 0.3 seconds and lasts for 7.5 seconds. The percentage decrease of the peak amplitude of this signal was found to be the lowest of all signals with a decrease of 30.9%. The laser scanning had the highest peak amplitude both in the filtered and unfiltered time domains (Figure 43(e)), with a percentage decrease of 90.5%, resulting in a filtered peak amplitude of 0.1V. Carefully analysing the filtered time-domain peak amplitudes of all the noise signals it was found that a voltage threshold, which was not below 0.1 V, would be sufficient in supressing all the noise signals which were characterised.

Unfiltered	Filtered
a) Machine in idle	
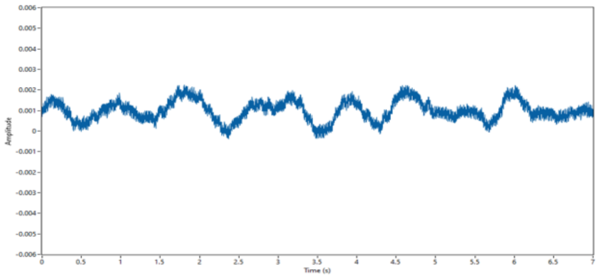	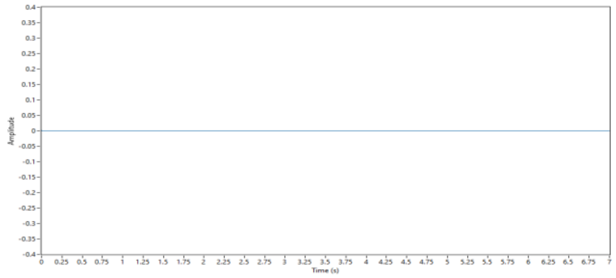
b) Build platform moved down by 1mm	
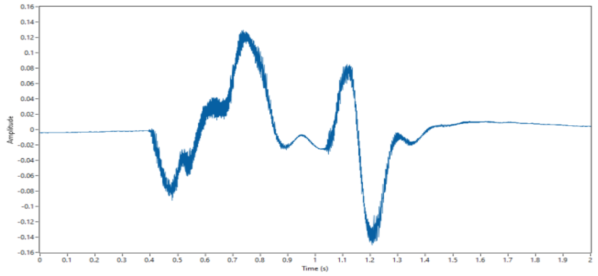	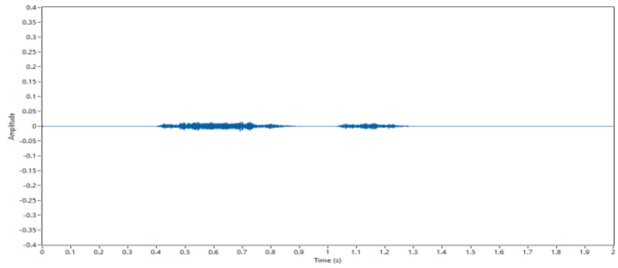
c) Recoater arm movement right	
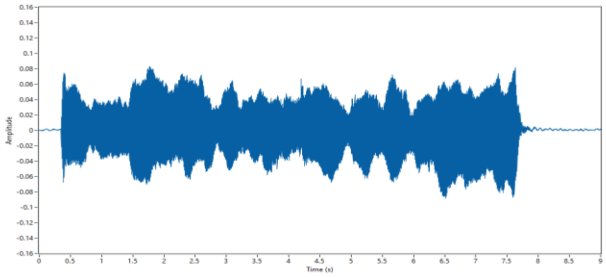	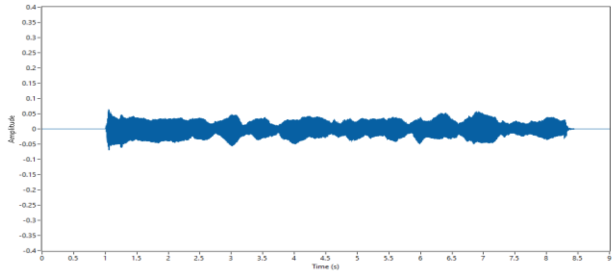
d) Recirculating fan	
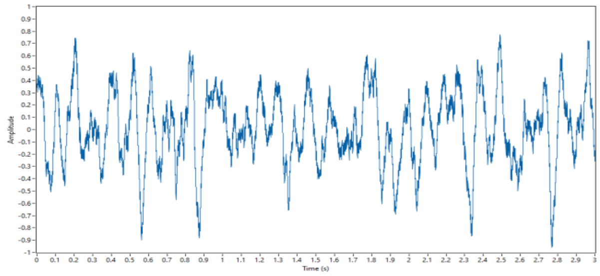	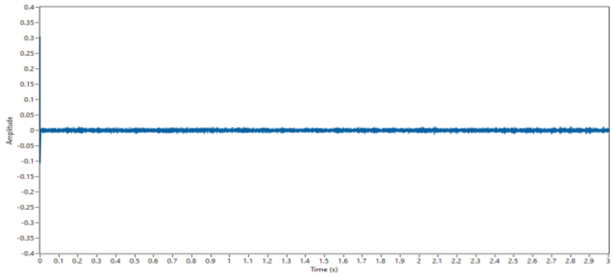
e) Laser scanning	
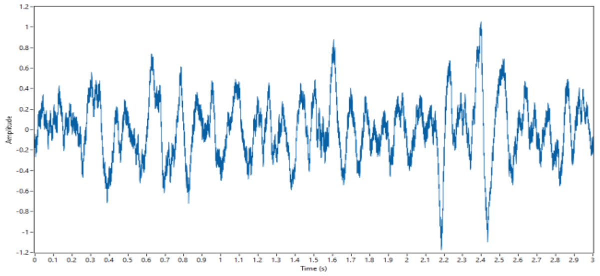	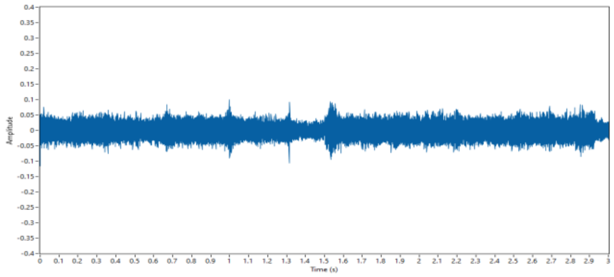

Figure 43: Time-domain AE signals of the machine is idle (a), build platform movement (b), recoater arm movement (c), recirculating fan (d), and laser scanning (e)

4.2.4.4. Summary of machine noise signals

When considering only the frequencies of the noise signals, it was found that all the characterised signals had peak frequencies below 2 kHz, apart from the signal of the recoater arm movement. The loudest signal before applying the 2 kHz high-pass filter was that of the recirculating fan running, although after applying the filter, the loudest signal was that of the recoater arm movement. The SNR was used to indicate the effectiveness of the applied filter and the values indicated that the filter selection was suitable. The signal which had the highest peak amplitude after applying the 2 kHz high-pass filter was the laser scanning, followed by that of the recoater arm movement. In conclusion, the filtered signals in the time domain which were identified as of possible concern when monitoring for cracks after applying the high-pass filter, were that of the build platform moving up/down, the recoater arm movement, the recirculating fan running, and the laser scanning, due to their high-peak amplitudes compared to the other noise signals. Their peak amplitudes, in comparison to other noise signals, can be seen in Figure 42, where a graphical representation of all the time-domain AE features of the machine noise is shown. Through careful analysis of the filtered time-domain peak amplitudes of all the noise signals, it was found that a voltage threshold of ~ 0.1 V would be sufficient to suppress all the noise signals which were characterised. More discussion regarding the applied voltage thresholding follows in section 4.4.

4.3. Analysis of crack signals

4.3.1. Frequency-domain AE features of cantilever cracks

The FFT of the different crack signals is shown in Figure 44 (left) where the frequency contents of the crack signals were analysed. The STFT, in Figure 44 (right), was used to indicate the crack signals profile by analysing the respective frequencies with time.

a) Crack-S1-C1	
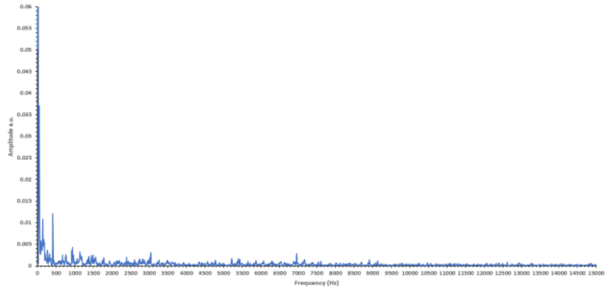	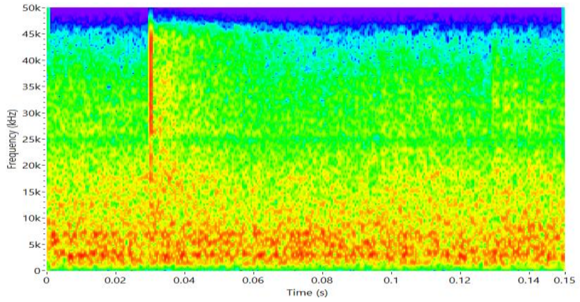

b) Crack-S1-C2	
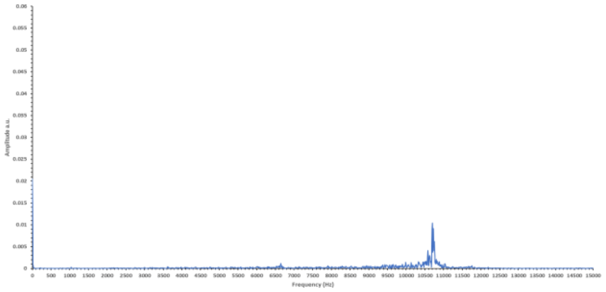	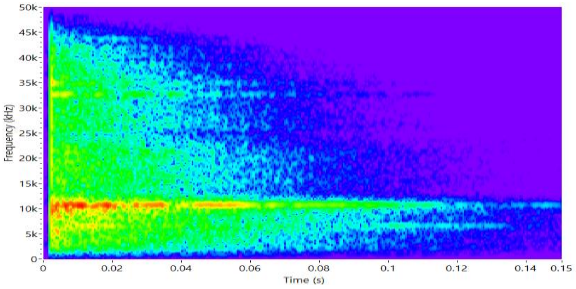
c) Crack-S2-C1	
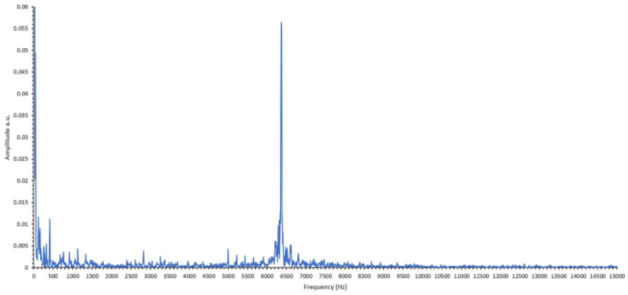	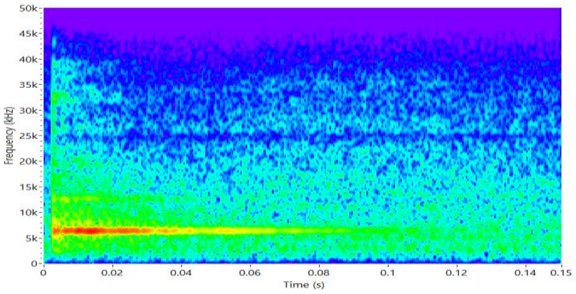
d) Crack-S2-C2	
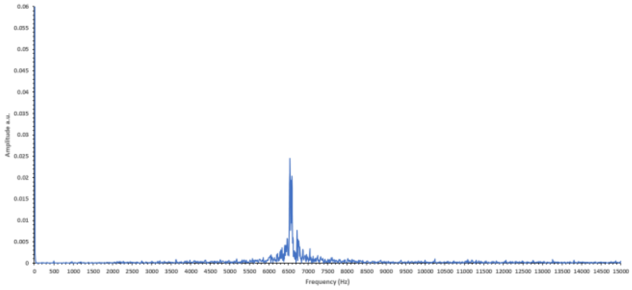	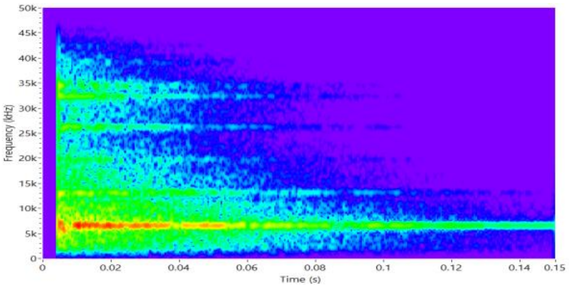
e) Crack-S3-C1	
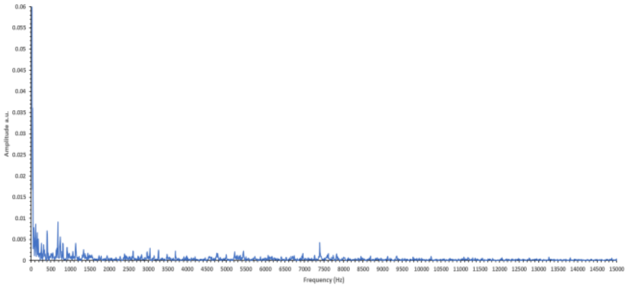	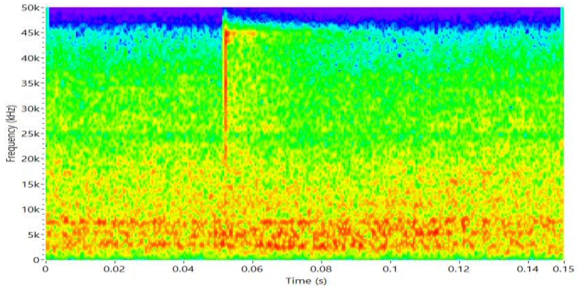
f) Crack-S3-C2	
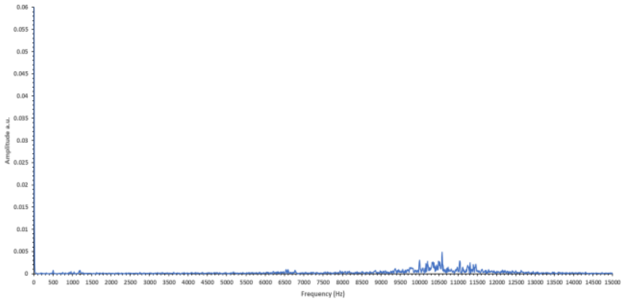	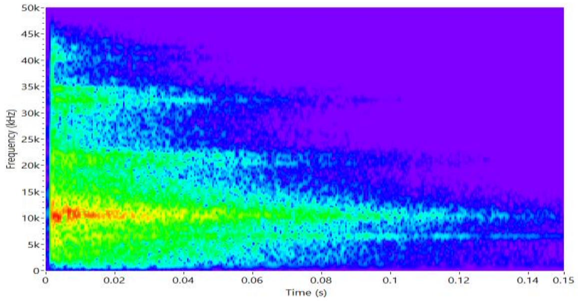

g) Crack-S4-C1	
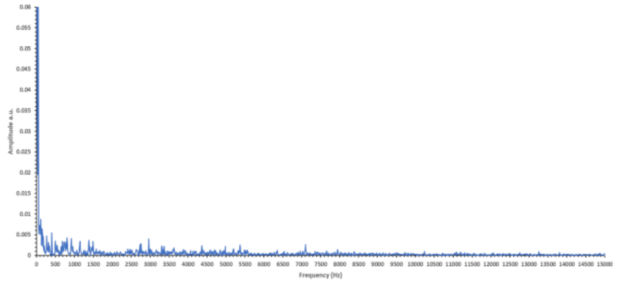	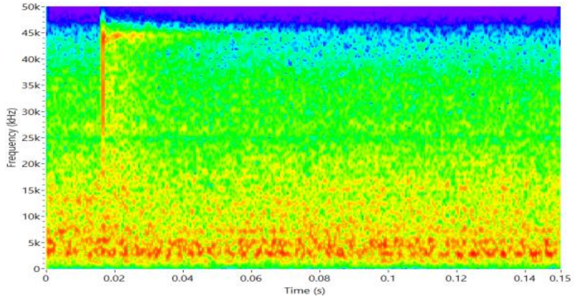

Figure 44: Unfiltered FFT (left) and filtered STFT (right) of AE from cantilever cracks, crack-S1-C1 (a), crack-S1-C2 (b), crack-S2-C1 (c), crack-S2-C2 (d), crack-S3-C1 (e), crack-S3-C2 (f), and crack-S4-C1 (g)

The cantilever cracks which occurred initially during the build process in Figure 44 (a), (e) and (g) had similar frequency profiles (see STFT in Figure 44) even though machine noise signals were present, such as that of the laser scanning, within the signal. As expected, these initial cracks were identified by the sudden impulse and increase in the intensities at the higher frequencies, which were above 25 kHz and had a very short duration. As in Figure 44 (e), the initial crack which occurred in specimen 3 (crack-S3-C1) can be seen initiating at approximately 0.05 seconds and only lasting for 0.01 seconds. The FFT of the same crack had a peak frequency of 7.4 kHz, which was accompanied by the frequencies of the laser scanning and other noise signals and ranged up to 47 kHz. The peak frequency of this crack (crack-S3-C1) was also in the same range as the other cracks which occurred in the same conditions during the build process (Table 7). When analysing the peak frequencies of the cracks which occurred during the build phase while the laser was scanning, it was found that the peak frequency which had the highest intensity of all the crack signals was that of the crack which occurred initially in specimen 2 (crack-S2-C1). This could be due to specimen 2 being the last specimen to fail during the build process, which would have prompted the build-up of additional residual stresses. The crack signal profile of this crack on the STFT was also altered compared to that of the cracks which occurred in similar conditions (Figure 44 (c)).

Considering the cantilever cracks in Figure 44 (b), (d) and (f), which occurred during the cool-down phase when the build had been stopped and the laser was not scanning. As expected, the crack signal profile of these cracks was different to the ones which occurred during the build process while the laser was scanning but was similar when compared to each other. Since these cracks occurred when the build process had stopped and there was no machine noise, the duration of these cracks was used as the sampling window for FFT and STFT. The peak frequencies of the cracks which occurred in specimen 1 (crack-S1-C2) and specimen 3 (crack-

S3-C2) were found to be the highest, with peak frequencies of 10.7 kHz and 10.6 kHz, respectively (Table 7). This change in the peak frequencies was expected as these cracks occurred in the cool-down phase when the cracking cantilever samples had already failed with the build plate and deformed, i.e. different shapes, hence different resonant frequencies.

Table 7: Cantilever crack signals frequency responses

Event	Peak frequencies from FFT	Occurrence from STFT
Crack-S1-C1	6 960 Hz	Crack observed by spike in intensity of higher frequencies occurring at 0.03 seconds and lasting for a short period.
Crack-S1-C2	10 700 Hz	Crack observed by burst of frequencies initially which decay with time and lasting for 0.15 seconds.
Crack-S2-C1	6 374 Hz	Crack observed by the peak frequency intensity which decays with time from 0.002 seconds.
Crack-S2-C2	6 540 Hz	Crack observed by burst of frequencies initially which decay with time and lasting for 0.15 seconds.
Crack-S3-C1	7 400 Hz	Crack observed by spike in intensity of higher frequencies occurring at 0.052 seconds and lasting for a short period.
Crack-S3-C2	10 587 Hz	Crack observed by burst of frequencies initially which decay with time and lasting for 0.15 seconds.
Crack-S4-C1	7 100Hz	Crack observed by spike in intensity of higher frequencies occurring at 0.015 seconds and lasting for a short period.

4.3.2. Time-domain AE features of cantilever cracks

In this section, the time-domain AE features of the crack signals, such as the RMS, SNR, and peak amplitudes, were analysed and compared to those of the characterised noise signals to determine the effect of the applied high-pass filter and assist in selecting an appropriate voltage threshold that would distinguish the signals of the cracks from those of the noise during the build process.

4.3.2.1 RMS of the cantilever crack signals

The RMS values of the cantilever crack signals were used to indicate the average loudness of the cracks, compare the loudness of the cracks with that of the noise signals, and determine how the loudness of the cracks was affected by the applied high-pass filter. In Table 8, the loudest crack signal before applying the high-pass filter occurred initially in specimen 3 (crack-S3-C1). After applying the 2 kHz high-pass filter, the loudest crack signal was now that of specimen 2 (crack-S2-C1). These two cracks occurred during the build process and might indicate that the machine noise, such as the laser scanning, had an effect on the high RMS values. The RMS which was affected the most by the high-pass filter was that of the initial cracks on specimen 1 (crack-S1-C1), specimen 3 (crack-S3-C1) and specimen 4 (crack-S4-C1). This high decrease in the loudness was concerning as it indicated that the applied filter might be negatively affecting the crack signals. However, comparing the RMS values of the noise signals in Table 5 on page 51 to the crack signals, the loudest machine noise signal after filtering was the recoater arm movement with an RMS value of 0.0165, which is below the lowest crack RMS of 0.0169 (Crack-S1-C1).

Table 8: RMS of crack signals

AE signal	Unfiltered crack signal RMS	Filtered crack signal RMS	% Decrease of RMS
Crack-S1-C1	0.2955	0.0169	94.3%
Crack-S1-C2	0.0502	0.0454	9.6%
Crack-S2-C1	0.2851	0.2263	20.6%
Crack-S2-C2	0.1558	0.1210	22.3%
Crack-S3-C1	0.3427	0.0199	94.2%
Crack-S3-C2	0.0880	0.0619	29.7%
Crack-S4-C1	0.2863	0.0207	92.8%

4.3.2.2 Signal-to-noise ratio (SNR) of cantilever crack signals

The SNR of the crack signals expressed in decibels is shown in Figure 45. The average of the crack signals was used to calculate the SNR, as shown in Equation 9. When analysing the figure, it was found that all the investigated crack signals had an SNR response of above 0 dB, which indicated that the signal of the cracks exceeded that of all the characterised machine noise signals. However, some noise signals, like the recoater arm movement and the laser scanning, had low SNR values (see A3 in the appendix on page 90).

$$SNR_{voltage} = \frac{RMS_{average\ crack\ signal\ voltage}}{RMS_{machine\ noise\ voltage}} \ldots\ldots\ldots\ldots\ldots\ldots\ldots\ldots \textit{Equation 9}$$

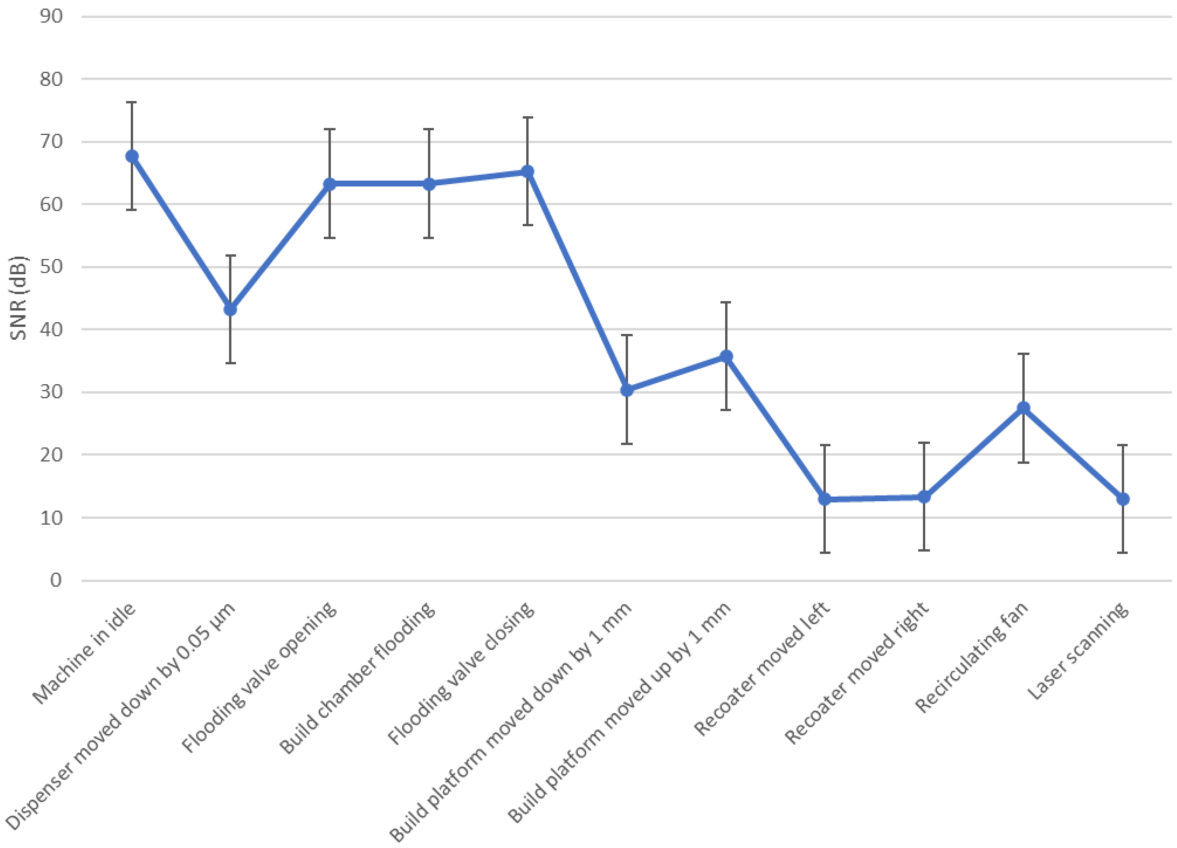

Figure 45: Signal-to-noise ratio of the average cantilever crack signal against the machine noise signals

4.4. Voltage threshold as a tool for crack detection

The peak amplitudes of the crack signals were analysed to consider if the minimum required voltage threshold from the machine noise peak amplitudes would be sufficient when monitoring for cracks. The crack signal profiles of the cracking cantilevers in the time domain are shown in Figure 46.

a) Crack-S1-C1	
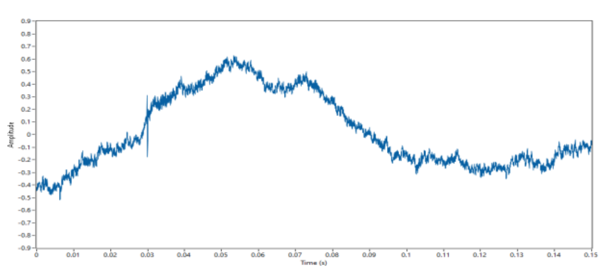	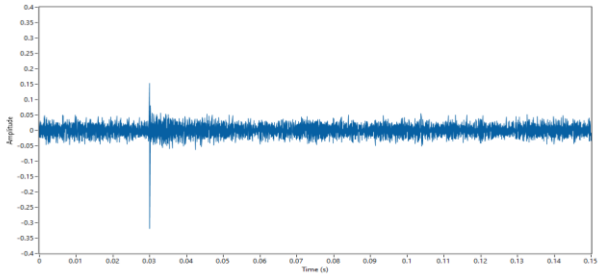
b) Crack-S1-C2	
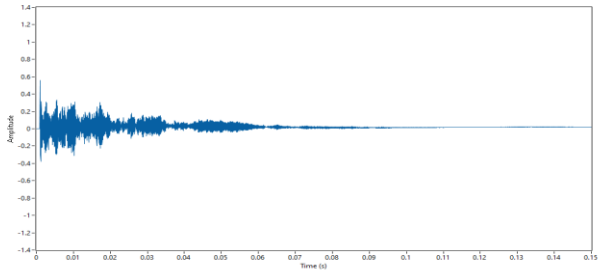	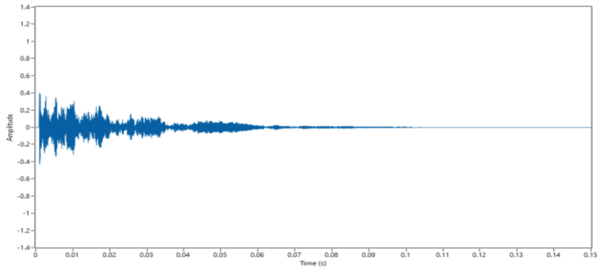
c) Crack-S2-C1	
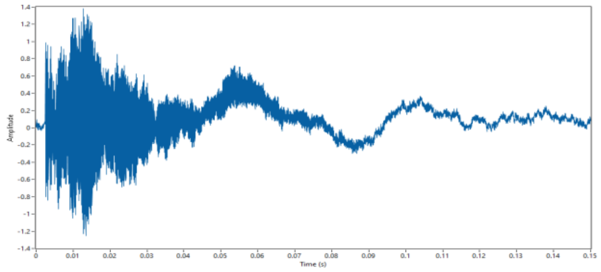	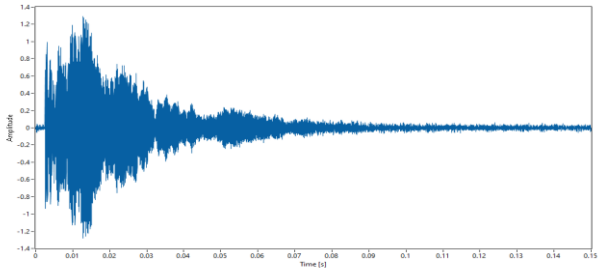
d) Crack-S2-C2	
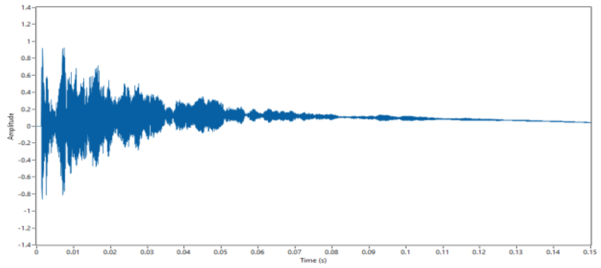	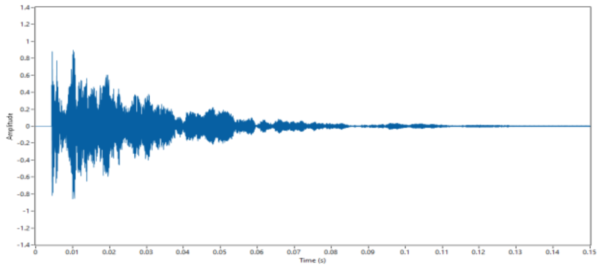
e) Crack-S3-C1	
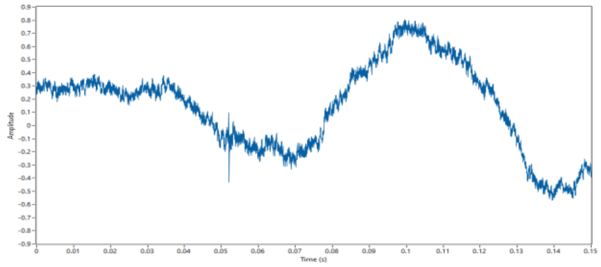	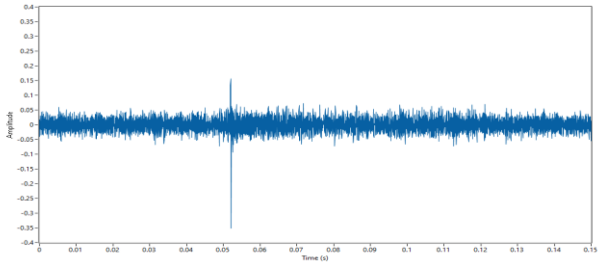

f) Crack-S3-C2	
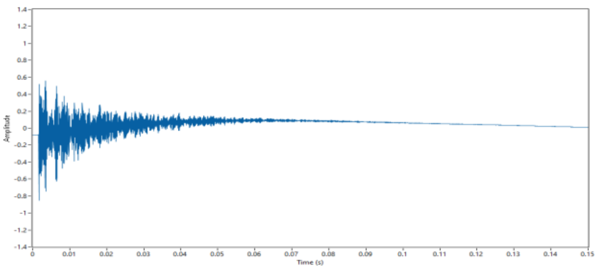	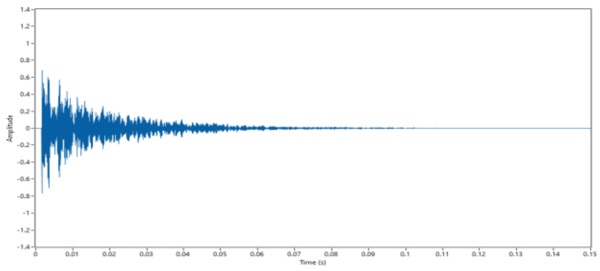
g) Crack-S4-C1	
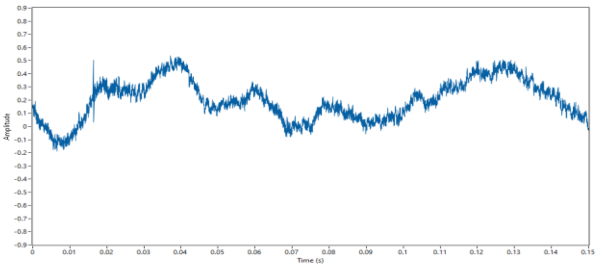	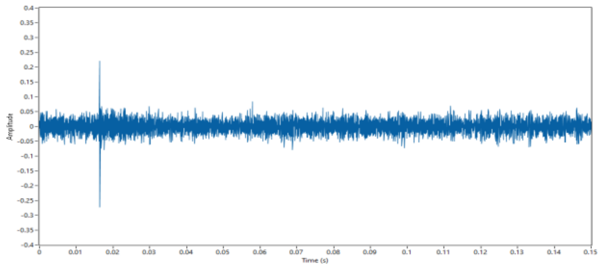

Figure 46: Unfiltered (left) and filtered (right) time-domain AE signals of the cantilever, crack-S1-C1 (a), crack-S1-C2 (b), crack-S3-C1 (c), crack-S3-C2 (d), and crack-S4-C1 (e)

Cracks which occurred during the build phase, i.e. while the laser was scanning and the recirculating fan was running, are shown in Figure 46 (a), (e), and (g). Cracks were difficult to identify and locate in the unfiltered time-domain signal due to the machine-related noise present within the signal. These cracks were only noticed by the slight spike in the amplitude as in the crack signal, which occurred initially to specimen 1 (crack-S1-C1) in Figure 46 (a) left, which can be seen occurring at 0.03 seconds for a very short duration. The crack signal profiles of the cracking cantilevers, which occurred during the cool-down phase when the laser was not scanning, are seen in Figure 46 (b), (d), and (f). These types of cracks were easily identified by the sudden burst in the amplitude intensity which decreased with time. The crack signal profile of these cracks before and after applying the high-pass filter was similar, apart from the peak amplitude intensities. The crack which occurred initially in specimen 2 in Figure 46 (c) had a noticeable increase in energy compared to the other cracks which occurred in similar conditions. As already mentioned, this was the last specimen to fail during the build process which would have prompted the build-up of additional residual stresses.

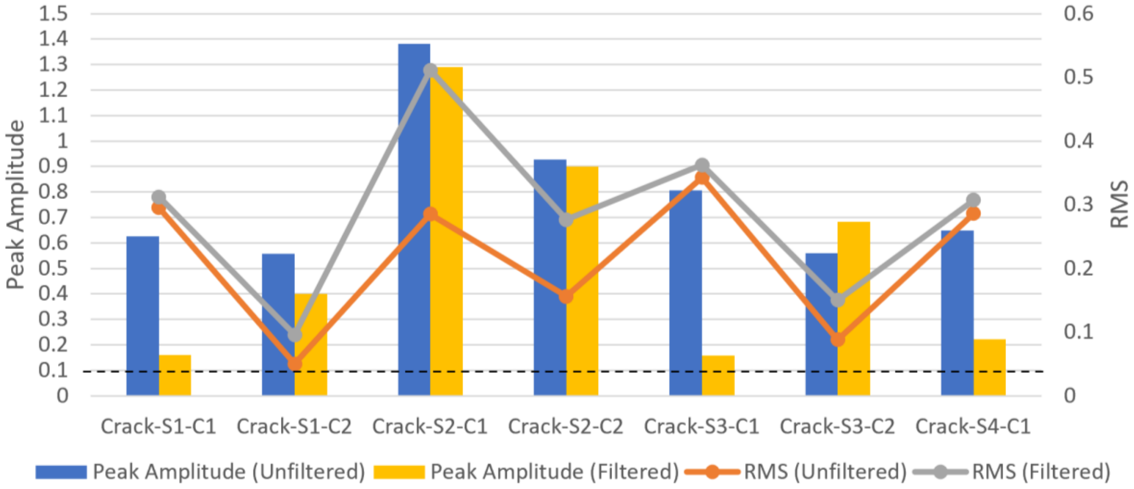

Figure 47: Time-domain AE features of cantilever cracks with dotted lines indicating the highest noise-peak amplitude after filtering

The crack signal which had the lowest amplitude after applying the high-pass filter was that of specimen 3 (crack-S3-C1), with a peak amplitude of 0.16 V. The highest peak amplitude from the machine noise section was that of the laser scanning with a peak amplitude of 0.0999 V (indicated by dotted lines in Figure 47). Subtracting the loudest noise signal peak amplitude from the softest crack peak amplitude gave a difference of only 0.057 V. Therefore, a voltage threshold of 0.13 V would be sufficient to be able to detect all the cantilever cracks which were characterised during the experiments and distinguish them from the machine noise signals. In

Figure *48*, the application of the 0.13 V voltage threshold to the filtered time-domain AE signal of Figure 39 (which had the machine noise signals and the two cracks that occurred in the cool-down phase) yielded the results shown.

All the machine noise which occurred in the first 45 seconds in the time domain was omitted from the current time-domain graph due to their peak amplitudes being lower than the selected voltage threshold. Only the crack signals which occurred in the cool-down phase of specimen 2 (crack-S2-C2) and specimen 3 (crack-S3-C2) are noticed. In the enlarged representation of these two cracks in the time domain of

Figure *48*(b), each point above the indicated voltage threshold is clearly recorded with the crack profile and duration of the cracks observed. The voltage threshold approach can be used by constantly monitoring the L-BPF process during the build and flagging any timestamp that exceeds the set threshold with pre-calibrated machine noise signals.

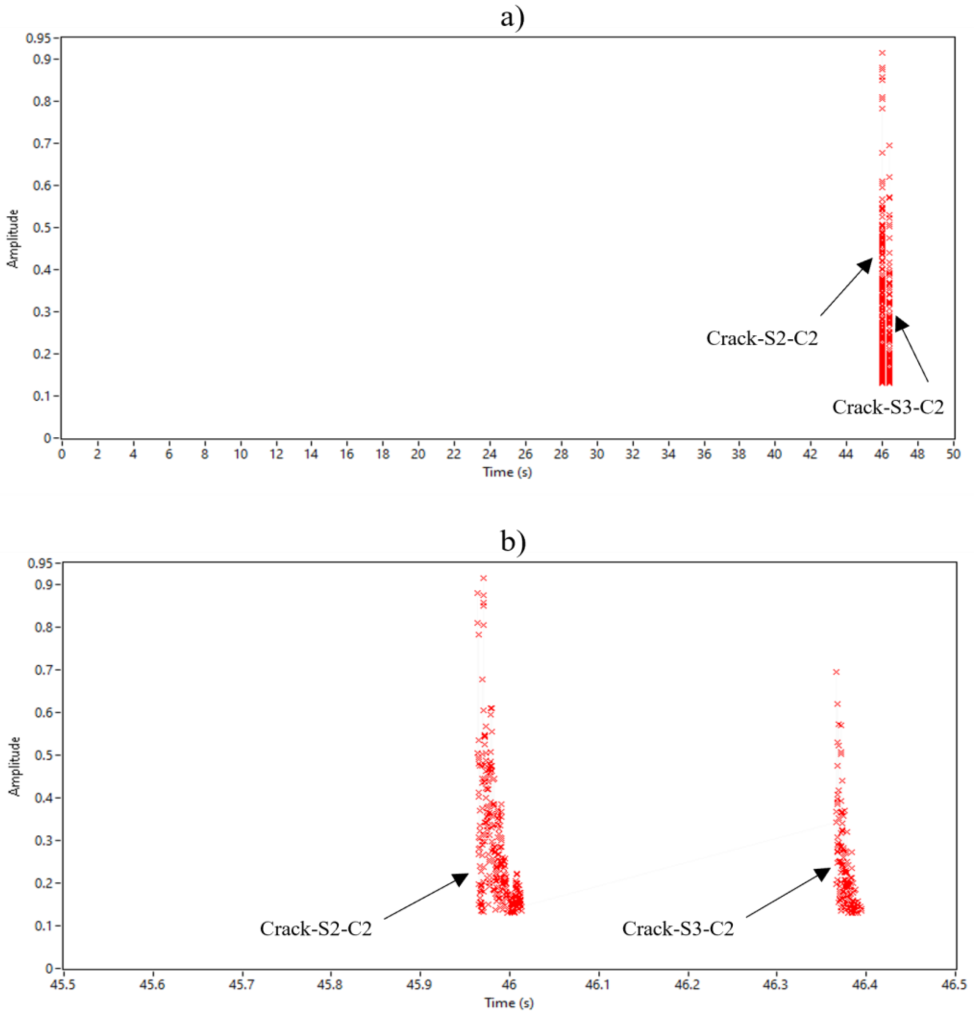

Figure 48: Amplitude-time graph of cantilever cracks with voltage threshold response of (a) (crack-S2-C2) and (crack-S3-C2), (b) one-second window of the same cracks

4.5. Summary of cantilever crack signals

The initial failure heights of all the cracking cantilevers which occurred during the build phase were similar. The crack profile and duration of the cracks which occurred during the build phase while the laser was scanning were different to those which occurred in the cool-down phase when the build process had been stopped. The SNR of all cantilever cracks was above 0 dB, indicating that the signal of the cracks exceeded that of the characterised noise. The cantilever cracks which occurred while the laser was scanning were difficult to identify and locate in the unfiltered time-domain signal and even in the frequency-time domain because of the machine-related noise present within the signal. These cracks could only be clearly identified and located after applying the 2 kHz high-pass filter and voltage threshold. All the crack signals could be detected and distinguished by using the time-domain features of the AE signal and the application of the voltage threshold of 0.13V.

Chapter 5: Conclusions

L-PBF is an AM technique which involves a layer-by-layer build process, where high-temperature gradients result from the interaction of the laser beam with the powder material on the build plate. This build phenomenon induces residual stresses in the parts being built and, at times, causes them to fail during/post-process due to defects such as the formation of cracks, pores, and deformations. These defects affect the quality assurance of the L-PBF built parts in still being suitable for their intended use in application. Currently implemented quality control measures mostly occur post-process, with methods such as CT scanning being used in some cases. These post process methods further add to the cost and time of production of the L-PBF parts. Therefore, contributing to a need for quality control measure which can monitor the build process in situ in detail during the build.

Design and development of the cracking cantilever sample:

In the current study, a cantilever sample which would fail in an anticipated manner was designed and developed with a predictable failure height using known residual stress phenomena with the aid of simulation techniques. The initial design height of the cracking cantilever sample was chosen with the intent to save as much material as possible while also keeping in mind to prompt the build-up of residual stresses within the layers for a sample that would fail in a reasonable time for in situ monitoring. To determine the possible failure height of the designed cantilever, eight different CAD models with varying heights were simulated using the inherent strain method. The simulation results indicated that as the height of the cantilever was increased, so did the effective stress and strain at the first strut (the point at which failure was expected to initiate). During the validation phase of the cracking cantilever samples on the EOS M290, the samples of the first build were seen to fail simultaneously at a height close to the predicted failure height, indicating the effectiveness of the simulation results, while on the second build, the cantilever samples failed at slightly different heights. This slight deviation in the second build could probably be due to the dynamics of the gas flow in the chamber, slight cracking at the struts, which caused local plastic deformation and, in turn, a reduction in stresses or the thermal complexity of the L-PBF process.

AE monitoring of the build process and cantilever samples:

The second phase of the experiments included the AE monitoring of the build process using the EOS M280. The entire build process of the cantilever samples was recorded until all cantilevers had failed with the build plate using a simple and cost-effective gas-borne AE setup with an ICP microphone. The cool-down process of the cantilevers was also recorded after the build process had been stopped. To characterise the machine "noise" of the EOS M280, pre-recordings of the machine AE signals such as that of the recirculating fan running and the recoater arm movement were conducted prior to commencement of the build process in the build chamber. After evaluating the machine AE "noise" of the EOS M280, the cracking cantilevers were manufactured. It was found when analysing the AE results that attempting to use only the amplitudes of the recorded AE signal in the unfiltered time domain to detect the cracks proved difficult due to the machine-related noise, which overpowered that of the crack signals. Only after considering the frequencies present within the STFT and the application of the 2 kHz high-pass filter could the different AE events within the signal be located and distinguished in the time domain and their crack signal profiles determined. The FFT of the recorded AE signals indicated the frequencies present within the signals and assisted in selecting the appropriate high pass filter. The SNR and percentage decrease of the RMS values in the time domain were used as a measure to indicate the effectiveness of the applied filter. The RMS values of the recorded AE signals indicated the average loudness of the signals, with the loudest noise signal after applying the 2 kHz high-pass filter being that of the recoater arm movement, while all the crack signals could be distinguished while the laser was scanning.

Proposed real-time AE monitoring method:

A proposed real time AE method to detect cracks is to use a voltage threshold on the filtered time-domain signal. The peak voltage amplitudes in the time domain were analysed to assist in selecting an appropriate voltage threshold value that would be able to distinguish the crack signals from that of the noise signals. The noise signals in the time domain which were identified as signals of concern after applying the 2 kHz high-pass filter were that of the build platform moving up/down, the recoater arm movement, the recirculating fan running, and the laser scanning. When carefully analysing the filtered time-domain peak amplitudes of all the noise signals, it was found that a voltage threshold which was not below 0.1 V would be sufficient in supressing all the noise signals which were characterised during this work. When analysing the crack signal with the lowest peak amplitude, it was shown that a voltage threshold value of 0.13 V would be sufficient for the detection of the crack signals. For all investigated crack cases, the crack signals could be detected and identified by using the time-domain voltage threshold value of 0.13 V. The developed cracking cantilever sample can be further used to reduce the time and cost of other online monitoring research and development by producing predictable and repeatable deformations that can be monitored by different methods during the L-PBF process.

Future work

Future work includes: Placing a set of microphones at different positions in the build chamber to localise the cracks. Building the designed cantilevers with different materials and process parameters to investigate the effect on AE signals. Finding the minimum crack sizes that could be detected. Using an accelerometer placed underneath the build plate along with a microphone to see the difference between the cracks detected by gas-borne and structure-borne AE. Lastly, attempting to integrate the proposed method with machine-learning techniques and optical methods.

REFERENCES

Ali, H., Ma, L., Ghadbeigi, H., and Mumtaz, K., 2017. In-situ residual stress reduction, martensitic decomposition and mechanical properties enhancement through high temperature powder bed pre-heating of Selective Laser Melted Ti6Al4V. Materials Science and Engineering A, 695, pp 211–220. https://doi.org/10.1016/j.msea.2017.04.033

Bartlett, J. L., Croom, B. P., Burdick, J., Henkel, D., and Li, X., 2018. Revealing mechanisms of residual stress development in additive manufacturing via digital image correlation. Additive Manufacturing, 22, pp 1–12. https://doi.org/10.1016/j.addma.2018.04.025

Böhm, C., Werz, M., Weihe, S., 2022. Practical approach to eliminate solidification cracks by supplementing almg4.5mn0.7 with AlSi10Mg powder in laser powder bed fusion. Materials, *15*(2). https://doi.org/10.3390/ma15020572

Boyes, W., 2009. Instrumentation Reference Book, Butterworth-Heinemann, 4, pp 1–928.

Brüel and Kjær,1977. Various condenser microphones and microphone preamplifiers. Theory and Application Handbook.

Chen, L., Yao, X., Tan, C., He, W., Su, J., Weng, F., Moon, S. K., 2023. In-situ crack and keyhole pore detection in laser directed energy deposition through acoustic signal and deep learning, Additive Manufacturing, 69, pp 1–18. https://doi:10.1016/j.addma.2023.103547

Chen, S., Gao, H., Zhang, Y., Wu, Q., Gao, Z., Zhou, X., 2022. Review on residual stresses in metal additive manufacturing: formation mechanisms, parameter dependencies, prediction and control approaches. Journal of Materials Research and Technology, 17, pp 2950–2974. https://doi.org/10.1016/J.JMRT.2022.02.054

Cobbinah, P. V., Nzeukou, R. A., Onawale, O. T., and Matizamhuka, W. R., 2021. Laser powder bed fusion of potential superalloys: A review. Metals, MDPI AG, 11 (1), pp 1–37. https://doi.org/10.3390/met11010058

Dal, M., Gunenthiram, V., Fabbro, R., Koutiri, I., Coste, F., Peyre, P., and Schneider, M., 2017. Experimental analysis of spatter generation and melt-pool behavior during the powder bed laser beam melting process, J. Mater. Process. Technol. 251. pp 376–386.

De Beer, D., du Preez, W., Greyling, H., Prinsloo, F., Sciammarella, F., Trollip, N., Vermeulen, M., and Wohlers, T., 2016. A South African additive manufacturing strategy. (Online) Available from: https://www.dst.gov.za/index.php/resource-center/strategies-and-reports/2629-a-south-african-additive-manufacturing-strategy (Accessed: February 21, 2023).

Dewesoft, 2022. What is signal processing? Available at: https://dewesoft.com/daq/what-is-signal-processing (Accessed: July 20, 2022).

Du Plessis, A., MacDonald, E., Waller, J. M., and Berto, F., 2021. Non-destructive testing of parts produced by laser powder bed fusion, Fundamentals of Laser Powder Bed Fusion of Metals. Elsevier Ltd, pp 278–299. https://doi.org/10.1016/b978-0-12-824090-8.00014-7

Eargle, J., 2005. The Microphone Handbook. Second Edition. Elsevier Ltd, pp 1–391.

EOS GmbH., 2022. Additive Manufacturing (Online). Available at: https://www.eos.info/ (Accessed: June 20, 2022).

Eschner, N., Weiser, L., Häfner, B., and Lanza, G., 2018. Development of an acoustic process monitoring system for the selective laser melting (SLM). 29th Annual International Solid Freeform Fabrication Symposium, Austin, TX, USA.

Eschner, N., Weiser, L., Häfner, B., and Lanza, G., 2020. Classification of specimen density in laser powder bed fusion (L-PBF) using in-process structure-borne acoustic process emissions. Additive Manufacturing, 34, pp 1–11.

Everton, S. K., Hirsch, M., Stavroulakis, P. I., Leach, R. K., and Clare, A.T., 2016. Review of in-situ process monitoring and in-situ metrology for metal additive manufacturing. Materials and Design, Elsevier Ltd. 95, pp 431–445. https://doi.org/10.1016/j.matdes.2016.01.099

Fang, Z. C., Wu, Z. L., Huang, C. G., and Wu, C. W., 2020. Review on residual stress in selective laser melting additive manufacturing of alloy parts. Optics and Laser Technology, Elsevier Ltd, 129, pp 1–15. https://doi.org/10.1016/j.optlastec.2020.106283

Fedina, T., 2021. Laser beam-material interaction in powder bed fusion. Doctoral dissertation, Luleå University of Technology. pp 1–22. Available at: www.ltu.se.

Francis, M., Kemper, N., Maghdouri-White, Y., and Thayer, N., 2018. Additive manufacturing for advanced manufacturing. Additive Manufacturing, 9, p 4.

Fu, Y., Downey, A. R. J., Yuan, L., Zhang, T., Pratt, A., and Balogun, Y., 2022. Machine learning algorithms for defect detection in metal laser-based additive manufacturing: A review. Journal of Manufacturing Processes, 75, pp 693–710.
https://doi.org/10.1016/j.jmapro.2021.12.061

Furumoto, T., Ueda, T., Abdul Aziz, M., Hosokawa, A., and Tanaka, R., 2010. Study on reduction of residual stress induced during rapid tooling process: Influence of heating conditions on residual stress. Key Engineering Materials, 447–448, pp 785–789.

Ghayoomi, M., 2021. Acoustic emission monitoring of the powder bed fusion process with machine learning approach. Master’s thesis, McMaster University, pp 44.

Gögelein, A., Ladewig, A., Zenzinger, G., and Bamberg, J., 2018. Process monitoring of additive manufacturing by using optical tomography. 14th Quantitative InfraRed Thermography Conference, 25–29 June 2018, Berlin-Germany, pp 266–272. https://doi.org/10.21611/qirt.2018.004

Grosse, C. U., and Ohtsu, M., 2008. Acoustic emission testing: Basics for research applications in civil engineering. Acoustic Emission Testing: Basics for Research-Applications in Civil Engineering. Springer Berlin Heidelberg. https://doi.org/10.1007/978-3-540-69972-9

ISO/ASTM 52900:2021. Additive manufacturing — General principles — Fundamentals and vocabulary. ASTM International, 2021.

Jamil, M., Khan, A. M., Hegab, H., Sarfraz, S., Sharma, N., Mia, M., Gupta, M. K., and Zhao, G., 2019. Internal cracks and non-metallic inclusions as root causes of casting failure in sugar mill roller shafts, Materials, 12 (15), pp 1–22. https://doi.org/10.3390/ma12152474

Jhabvala, J., Boillat, E., Antignac, T., and Glardon, R., 2010. On the effect of scanning strategies in the selective laser melting process. Virtual and Physical Prototyping, 5(2), pp 99–109. https://doi.org/10.1080/17452751003688368

Jolly, W. D., 1969. The use of acoustic emission as a weld quality monitor. BNWL-SA-2727, Pacific Northwest Laboratories, Richland, Washington, September 1969, pp 2-22. https://doi.org/10.2172/4072855

Karimi, J., Suryanarayana, C., Okulov, I., and Prashanth, K. G., 2021. Selective laser melting of Ti6Al4V: Effect of laser re-melting, Materials Science and Engineering A, 805. https://doi.org/10.1016/j.msea.2020.140558

Keller, N., and Ploshikhin, V., 2014. New method for fast predictions of residual stress and distortions of AM parts. Solid Freeform Fabrication Symposium, Austin, University of Texas at Austin.

Köhler, H., Jayaraman, V., Brosch., Hutter, F., and Seefeld, T., 2013. A novel thermal sensor applied for laser materials processing. Physics Procedia 41, pp 502–508.

Kouprianoff, D., 2021. Investigation of acoustic emission signal during laser powder bed fusion at different operating modes. South African Journal of Industrial Engineering, 32: 3, pp 279–283. https://doi.org/10.7166/32-3-2663

Kouprianoff, D., and du Preez, W., 2023. Reducing time and cost of the heat treatment post-processing of additively manufactured Ti6Al4V. Materials Today Communications, 35. https://doi.org/10.1016/j.mtcomm.2023.106186

Kouprianoff, D., Luwes, N., Yadroitsava, I., and Yadroitsev, I., 2018. Acoustic emission technique for online detection of fusion defects for single tracks during metal laser powder bed fusion. Solid Freeform Fabrication Symposium, University of Texas at Austin, 2018.

Kouprianoff, D., Yadroitsava, I., du Plessis, A., Luwes, N., and Yadroitsev, I., 2021. Monitoring of laser powder bed fusion by acoustic emission: Investigation of single tracks and layers. Frontiers in Mechanical Engineering, 7. pp 1–17. https://doi:10.3389/fmech.2021.678076

Krauss, H., Eschey, C., and Zaeh, M. H., 2012. Thermography for monitoring the selective laser melting process. Institute for Machine Tools and Industrial Management (IWB), Technische Universitaet Muenchen, Germany. pp 999–1014.

Kruth, J. P., Deckers, J., Yasa, E., and Wauthle, R., 2012. Assessing and comparing influencing factors of residual stresses in selective laser melting using a novel analysis method, Proceedings of the Institution of Mechanical Engineers, Part B: Journal of Engineering Manufacture, 226(6), pp 980–991.

Leuders, S., Thöne, M., Riemer, A., Niendorf, T., Tröster, T., Richard, H. A., and Maier, H. J., 2013. On the mechanical behaviour of titanium alloy TiAl6V4 manufactured by selective laser melting, Fatigue resistance and crack growth performance, International Journal of Fatigue, 48, pp 300–307.

Leung, C. L. A., Marussi, S., and Towrie, M., 2018. Laser-matter interactions in additive manufacturing of stainless steel SS316L and 13-93 bioactive glass revealed by in situ X-ray imaging. Additive Manufacturing, 24, pp 647–657.

Levkulich, N. C., Semiatin, S. L., Gockel, J. E., Middendorf, J. R., DeWald, A. T., and Klingbeil, N. W., 2019. The effect of process parameters on residual stress evolution and distortion in the laser powder bed fusion of Ti-6Al-4V. Additive Manufacturing, 28, pp 475–484. https://doi.org/10.1016/j.addma.2019.05.015

Lewis, J., 2012. Analog Dialogue 46-05 Back Burner, April (2012). Available at: www.analog.com/analogdialogue (Accessed: June 20, 2022).

Li, C., Liu, J. F., and Guo, Y. B., 2016. Efficient multiscale prediction of cantilever distortion by selective laser melting. 27th Annual International Solid Freeform Fabrication Symposium, Austin, TX, USA. pp 236–246.

Li, C., Liu, J. F., and Guo, Y. B., 2016. Prediction of residual stress and part distortion in selective laser melting. Procedia CIRP, 45, pp 171–174. https://doi.org/10.1016/j.procir.2016.02.058

Li, J. F., Li, L., and Stott, F. H., 2004. Thermal stresses and their implication on cracking during laser melting of ceramic materials. Acta Materialia, 52,14, pp 4385–4398. https://doi.org/10.1016/j.actamat.2004.06.005

Linde, A. M., 2018. Role of gases in AM. Making our world more productive. pp1–12. (Online) Available from: https://static.prd.echannel.linde.com/wcsstore/NO_REN_Industrial_Gas_Store/pdf/EN/Article-Role of gases in AM.pdf (Accessed: April 16, 2023).

Lu, X., Lin, X., Chiumenti, M., Cervera, M., Hu, Y., Ji, X., Ma, L., and Huang, W., 2019. In situ measurements and thermo-mechanical simulation of Ti–6Al–4V laser solid forming processes. International Journal of Mechanical Sciences, 153–154, pp 119–130. https://doi.org/10.1016/j.ijmecsci.2019.01.043

Ly, S., Rubenchik, A. M., Khairallah, S. A., Guss, G., and Matthews, M. J., 2017. Metal vapor micro-jet controls material redistribution in laser powder bed fusion additive manufacturing, Scientific Reports. 7, pp 1–12. https://doi.org/10.1038/s41598-017-04237-z

Martin, A. A., Calta, N. P., Hammons, J. A., Khairallah, S. A., Nielsen, M. H., Shuttlesworth, R. M., Sinclair, N., Matthews, M. J., Jeffries, J. R., Willey, T. M., and Lee, J. R. I., 2019. Ultrafast dynamics of laser-metal interactions in additive manufacturing alloys captured by in situ X-ray imaging. Mater, Today Adv, 1. https://doi.org/10.1016/j.mtadv.2019.01.001

Matthews, M. J., Guss, G., Khairallah, S. A., Rubenchik, A. M., Depond, P. J., and King, W.E., 2017. Denudation of metal powder layers in laser powder-bed fusion processes, Additive Manufacturing Handbook. Product Development for the Defence Industry. 114. pp 677–693. https://doi.org/10.1201/9781315119106

Mercelis, P., and Kruth, J., 2006. Residual stresses in selective laser sintering and selective laser melting. Rapid Prototyping Journal, 12(5), pp. 254–265.

http://www.scopus.com/inward/record.url?eid=2-s2.0-33750146493&partnerID=40&md5=7eebf030e96fa24df272aff5aea8f2cc

Mugwagwa, L., and Dimitrov, D., 2019. Investigation and management of residual stresses in selective laser melting of maraging steel. Available at: https://scholar.sun.ac.za.

Mugwagwa, L., Yadroitsava, I., Makoana, N. W., and Yadroitsev, I., 2021. Residual stress in laser powder bed fusion, Fundamentals of laser powder bed fusion of metals. Elsevier Ltd, pp 245–276. Available at: https://doi.org/10.1016/b978-0-12-824090-8.00014-7

Mutke, C., Geenen, K., Röttger, A., and Werner, W., 2018. Interaction between laser radiation and metallic powder of 316L austenitic steel during selective laser melting. Materials Characterization, 145, pp 337–346. https://doi.org/10.1016/j.matchar.2018.08.061

NASA Science, 2022. What is a laser, NASA Space Place. Available at: https://spaceplace.nasa.gov/laser/en/ (Accessed: April 13, 2022).

National Institute of Standards and Technology., 2023. AMB2018-01 Description. Available at: https://www.nist.gov/ambench/amb2018-01-description (Accessed: August 15, 2023).

National Instruments Corporation., 2022. Signal conditioning (Online). Available at: https://www.ni.com/en/shop/data-acquisition/sensor-fundamentals/measuring-sound-with-microphones.html (Accessed: August 20, 2022).

NSTF, 2023. About the awards. Available at: https://nstf.org.za/about-the-nstf-awards/ (Accessed: June 14, 2023).

OptoSigma, 2022. Laser, Available at: https://www.optosigma.com/. (Accessed: June 13, 2022).

Papadakis, L., Loizou, A., Risse, J., Bremen, S., and Schrage, J., 2014. A computational reduction model for appraising structural effects in selective laser melting manufacturing: a methodical model reduction proposed for time-efficient finite element analysis of larger components in selective laser melting. Virtual and Physical Prototyping, 9(1), pp 17–25.

PCB Piezotronics., 2023. Accelerometers. Available at: https://www.pcb.com/resources/technical-information/introduction-to-accelerometers (Accessed: July 10, 2023).

Platl, J., Bodner, S., Hofer, C., Landefeld, A., Leitner, H., Turk, C., Nielsen, M. A., Demir, A. G., Previtali, B., Keckes, J., and Schnitzer, R., 2022. Cracking mechanism in a laser powder bed fused cold-work tool steel: The role of residual stresses, microstructure and local elemental concentrations. Acta Materialia, 225. https://doi.org/10.1016/j.actamat.2021.117570

Purtonen, T., Kalliosaari, A., and Salminen, A., 2014. Monitoring and adaptive control of laser processes. Physics Procedia, 56(C), pp 1218–1231. https://doi.org/10.1016/j.phpro.2014.08.038

RapidDMLS., 2022. Home, Available at: https://www.rapiddmls.com/metal-3d-printing/. (Accessed: May 25, 2022).

Raylase, 2022. Focusshifter digital II, Available at:
https://www.raylase.de/en/products/focusshifter/focusshifter-digital-ii.html.
(Accessed: July 25, 2022).

Schumacher, T., Schechinger, B., & Vogel, T., 2022. AE Monitoring of Real Structures: Applications, Strengths, and Limitations, Springer Tracts in Civil Engineering. pp 731–752. https://doi.org/10.1007/978-3-030-67936-1_24.

Seleznev, M., Gustmann, T., Friebel, J. M., Peuker, U. A., Kühn, U., Hufenbach, J. K., Biermann, H., and Weidner, A., 2022. In situ detection of cracks during laser powder bed fusion using acoustic emission monitoring. Additive Manufacturing Letters, 3.
https://doi.org/10.1016/j.addlet.2022.100099

Shevchik, S.A., Kenel, C., Leinenbach, C., Wasmer, K., 2018. Acoustic emission for in situ quality monitoring in additive manufacturing using spectral convolutional neural networks, Additive Manufacturing. 21, pp 598–604.

Shrestha, S., and Chou, K., 2018. Single track scanning experiment in laser powder bed fusion process, Procedia Manufacturing, 26, pp 857–864.
https://doi.org/10.1016/j.promfg.2018.07.110

Soundararajan, B., Sofia, D., Barletta, D., and Poletto, M., 2021. Review on modeling techniques for powder bed fusion processes based on physical principles, Additive Manufacturing., 47. https://doi.org/10.1016/j.addma.2021.102336

Strantza, M., Van Hemelrijck, D., Guillaume, P., and Aggelis, D. G., 2017. Acoustic emission monitoring of crack propagation in additively manufactured and conventional titanium components. Mechanics Research Communications, 84, pp 8–13.
https://doi.org/10.1016/J.MECHRESCOM.2017.05.009

Sun, A., Kannatey-Asibu Jr, E., and Gartner, M., 1999. Sensor systems for real-time monitoring of laser weld quality. Journal of Laser Applications, 11(4), pp 153–168.

TechTarget., 2023. Machine learning. Available at:
https://www.techtarget.com/searchenterpriseai/definition/machine-learning-ML.
(Accessed: July 24, 2023).

TechTerms., 2022. Microphone. Available at:
https://www.techterms.com/definition/microphone. (Accessed: August 21, 2022).

Teixeira, Ó., Silva, F. J. G., Ferreira, L. P., and Atzeni, E., 2020. A review of heat treatments on improving the quality and residual stresses of the Ti–6Al–4V parts produced by additive manufacturing. Metals, MDPI AG, 10:8, pp 1–24. https://doi.org/10.3390/met10081006

Tempelman, J. R., Wachtor, A. J., Flynn, E. B., Depond, P. J., Forien, J.-B., Guss, G. M., Calta, N. P., and Matthews, M. J., 2022. Detection of keyhole pore formations in laser powder-bed fusion using acoustic process monitoring measurements, Additive Manufacturing, 55. https://doi: 10.1016/j.addma.2022.102735

Van Zyl, I., Yadroitsau, I., and Yadroitsava, I., 2016. Residual stress of Ti6Al4V (ELI) parts manufactured by direct metal laser sintering. Central University of Technology, Free State. pp 1-159.

Vrancken, B., Cain, V., Knutsen, R. and Van Humbeeck, J., 2014. Residual stress via the contour method in compact tension specimens produced via selective laser melting. Scripta Materialia, 87, pp. 29–32.

Wasmer, K., Kenel, C., Leinenbach, C., and Shevchik, S. A., 2017. In situ and real-time monitoring of powder-bed AM by combining acoustic emission and artificial intelligence. International Conference on Additive Manufacturing in Products and Applications, Springer.

Wasmer, K., Le-Quang, T., Meylan, B., Olbinado, M. P., Rack, A., and Shevchik, S. A., 2018. Laser processing quality monitoring by combining acoustic emission and machine learning: a high-speed X-ray imaging approach, Procedia CIRP, 74, pp 654–658. https://doi: 10.1016/j.procir.2018.08.054

Wischeropp, T., Emmelmann, C., Brandt, M., and Pateras, A., 2019. Measurement of actual powder layer height and packing density in a single layer in selective laser melting. Additive Manufacturing, 28, pp 176–183.

Xing, W., Ouyang, D., Li, N., and Liu, L., 2018. Estimation of residual stress in selective laser melting of a Zr-based amorphous alloy. Materials, 11(8). https://doi.org/10.3390/MA11081480

Yadroitsava, I., and Yadroitsev, I., 2015. Residual stress in metal specimens produced by direct metal laser sintering. pp 614 – 625.

Yadroitsava, I., Els, J., Booysen, G., and Yadroitsev, I., 2015. Peculiarities of single-track formation from TI6AL4V alloy at different laser power densities by selective laser melting, South African Journal of Industrial Engineering, 26(3), pp 86–95. https://doi.org/10.7166/26-3-1185

Yadroitsev, I., 2009. Selective laser melting: Direct manufacturing of 3D-objects by selective laser melting of metal powders. LAP LAMBERT Academic Publishing. ISBN: 3838317947.

Yadroitsev, I., Bertrand, P. H., and Smurov, I., 2007. Parametric analysis of the selective laser melting process. Applied Surface Science, 253, pp. 8064-69. https://doi.org/10.1016/j.apsusc.2007.02.088

Yadroitsev, I., Gusarov, A., Yadroitsava, I., and Smurov, I., 2010. Single track formation in selective laser melting of metal powders. Journal of Materials Processing Technology 210 (12), pp. 1624–1631. https://doi.org/10.1016/j.jmatprotec.2010.05.010

Yadroitsev, I., Krakhmalev, P., and Yadroitsava, I., 2015. Hierarchical design principles of selective laser melting for high-quality metallic objects, Additive Manufacturing, 7, pp 45–56. https://doi.org/10.1016/j.addma.2014.12.007

Yadroitsev, I., Yadroitsava, I., Bertrand, P., and Smurov, I., 2012. Factor analysis of selective laser melting process parameters and geometrical characteristics of synthesized single tracks. Rapid Prototype,18:201–8.

Yadroitsev, I., Yadroitsava, I., du Plessis, A., and Macdonald, E., 2021. Process monitoring of laser powder bed fusion, Fundamentals of Laser Powder Bed Fusion of Metals. Elsevier Ltd, pp 309. https://doi.org/10.1016/b978-0-12-824090-8.00014-7

Yadroitsev, I., Yadroitsava, I., du Plessis, A., and Macdonald, E., 2021. Residual stress in laser powder bed fusion. Fundamentals of Laser Powder Bed Fusion of Metals, Elsevier Ltd, pp 245–269.

Ye, D., Hong, G., Zhang, Y., Zhu, K., and Fuh, J., 2018. Defect detection in selective laser melting technology by acoustic signals with deep belief networks. The International Journal of Advanced Manufacturing Technology, 96(5), pp 2791–2801.

Zaeh, M., and Branner, G., 2010. Investigations on residual stresses and deformations in selective laser melting. Production Engineering, 4(1), pp 35– 45.

Zhang, K., Liua, W., and Shanga, X., 2007. Research on the processing experiments of laser metal deposition shaping. Optics and Laser Technology, 39, pp 549–557.

Zhang, Y., Wu, L., Guo, X., Kane, S., Deng, Y., Jung, Y. G., Lee, J. H., and Zhang, J., 2018. Additive manufacturing of metallic materials: A review. Journal of Materials Engineering and Performance, 27:1. https://doi.org/10.1007/s11665-017-2747-y

Zhou, G., Kou, J., Li, Y., Zhu, W., Chen, K., and Tamura, N., 2018. Quantitative scanning Laue diffraction microscopy: Application to the study of 3D printed nickel-based superalloys. Quantum Beam Science, MDPI, 2(2), pp 1–17. https://doi.org/10.3390/qubs2020013

Appendix

A1. Data from AE recordings

A1.1. Machine in idle

<table>
<tr><td>Filtered FFT of machine in idle</td><td>Filtered STFT of machine in idle</td></tr>
<tr><td>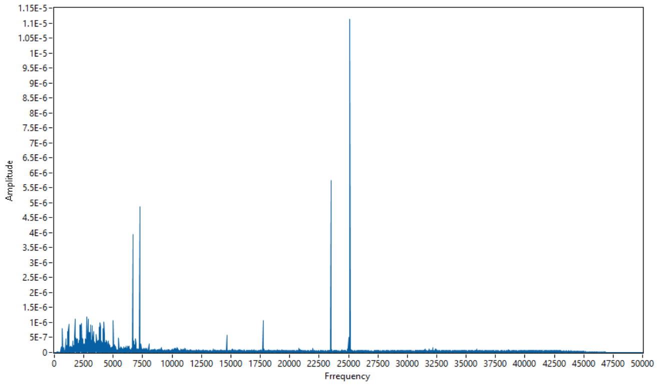
</td><td>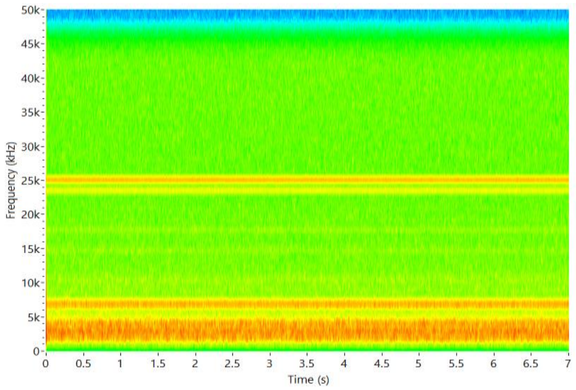
</td></tr>
<tr><td>Unfiltered time-domain AE signal of machine in idle</td><td>Filtered time-domain AE signal of machine in idle</td></tr>
<tr><td>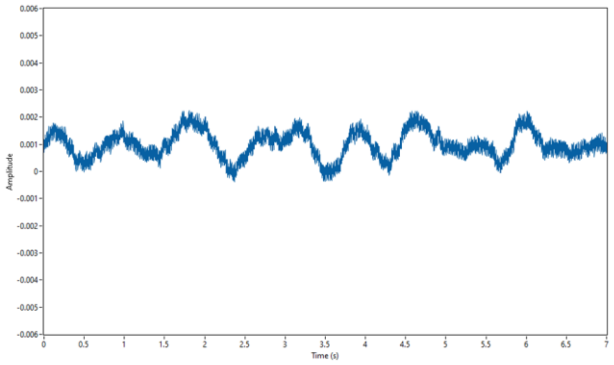
</td><td>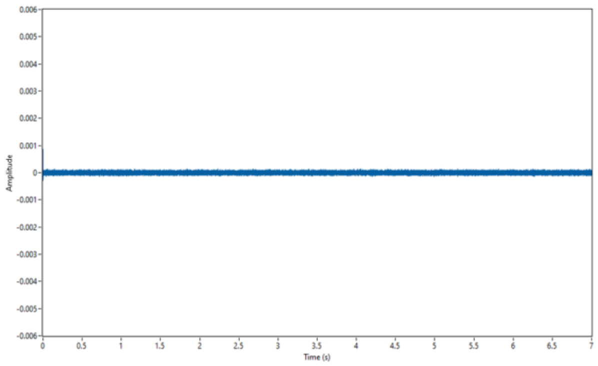
</td></tr>
</table>

A1.2 Dispenser moved down by 0.05 µm

Filtered FFT of dispenser moved down	Filtered STFT of dispenser moved down
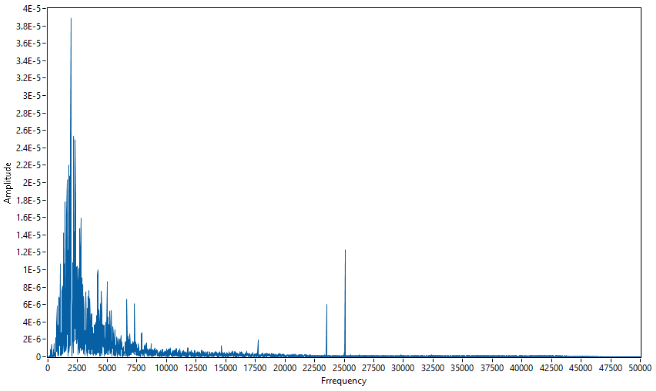	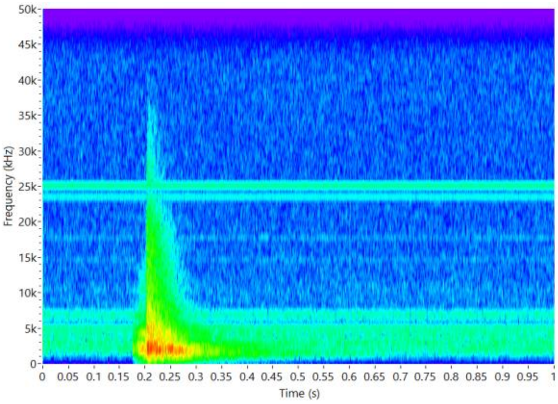
Unfiltered time-domain AE signal of dispenser moved down	Filtered time-domain AE signal of dispenser moved down
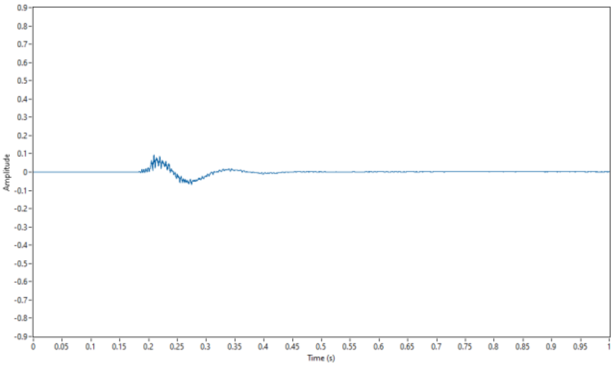	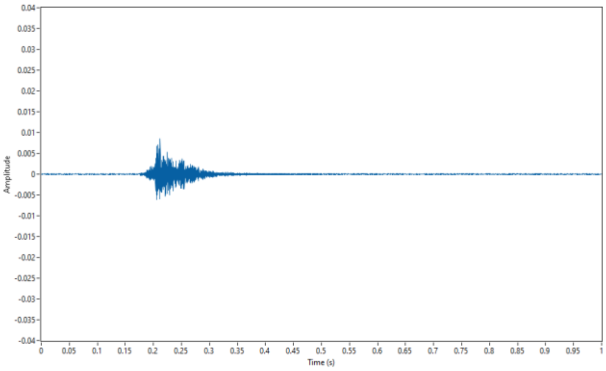

A1.3. Flooding valve opening

Filtered FFT of flooding valve opening	Filtered STFT of flooding valve opening
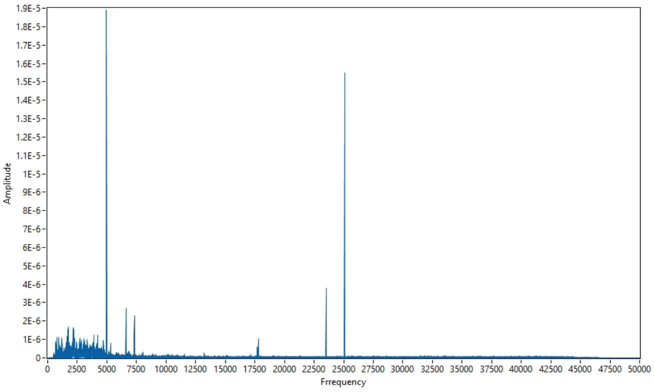	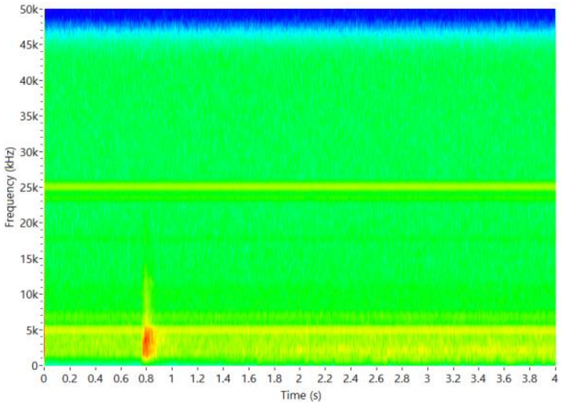
Unfiltered time-domain AE signal of flooding valve opening	Filtered time-domain AE signal of flooding valve opening
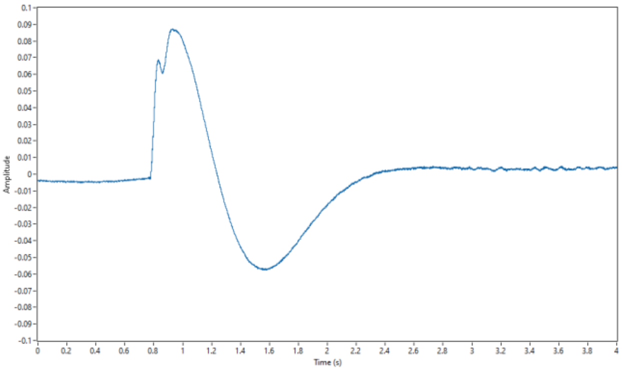	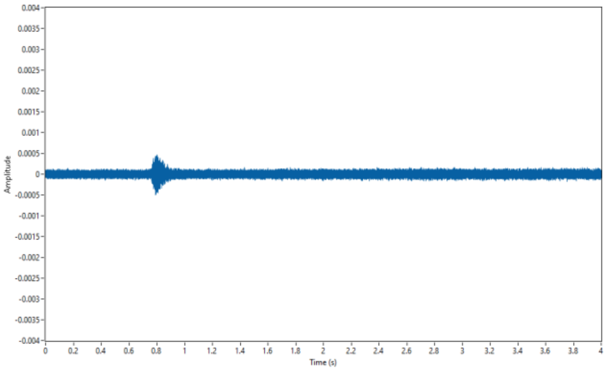

A1.4. Flooding

Filtered FFT of flooding	Filtered STFT of flooding
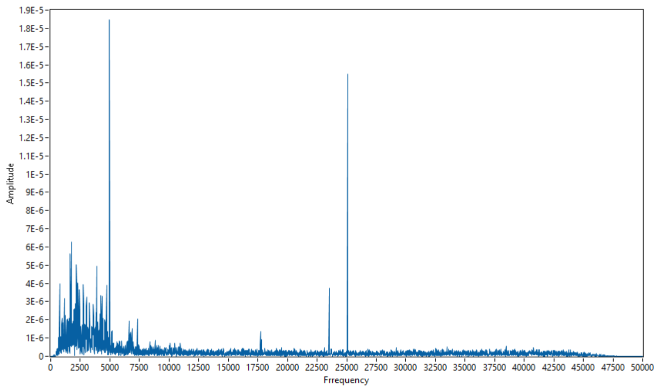	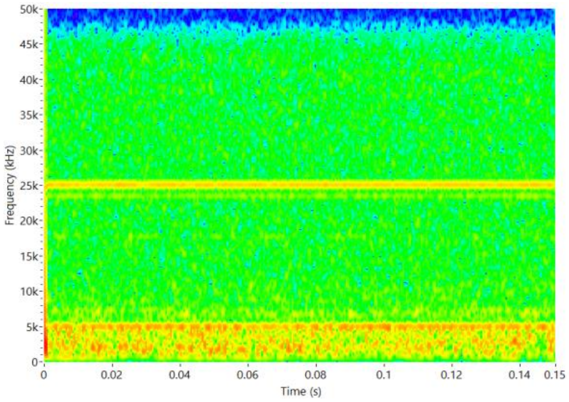
Unfiltered time-domain AE signal of flooding	**Filtered time-domain AE signal of flooding**
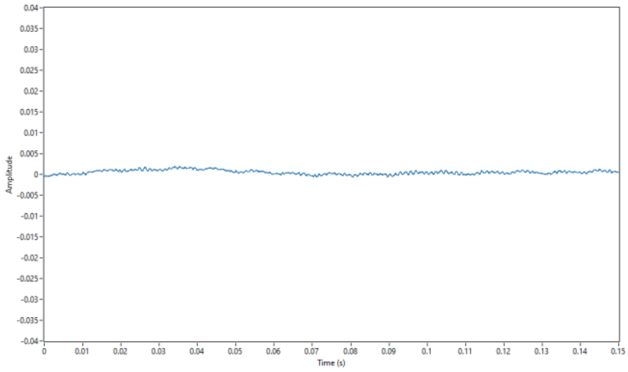	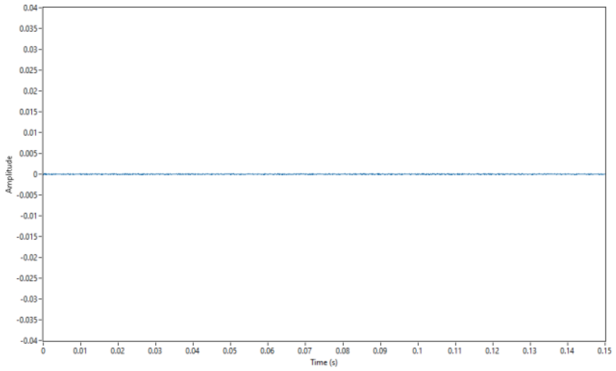

A1.5. Flooding valve closing

Filtered FFT of flooding valve closing	Filtered STFT of flooding valve closing
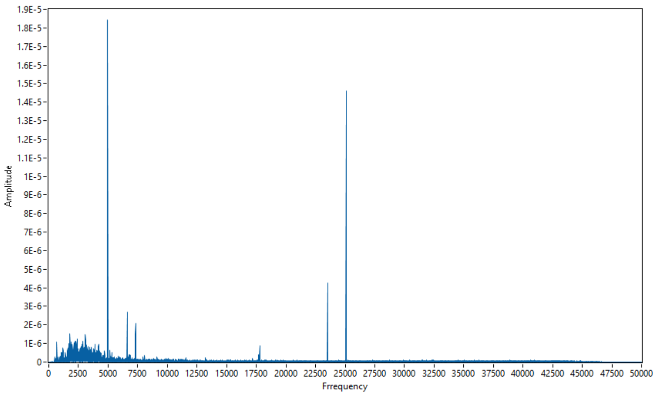	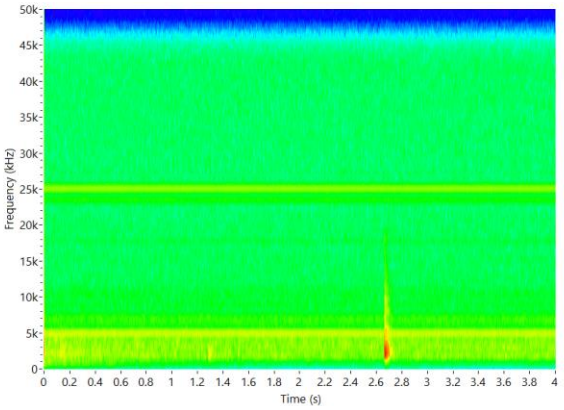
Unfiltered time-domain AE signal of flooding valve closing	Filtered time-domain AE signal of flooding valve closing
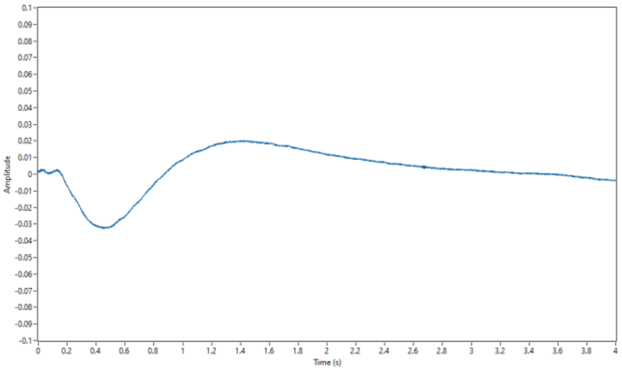	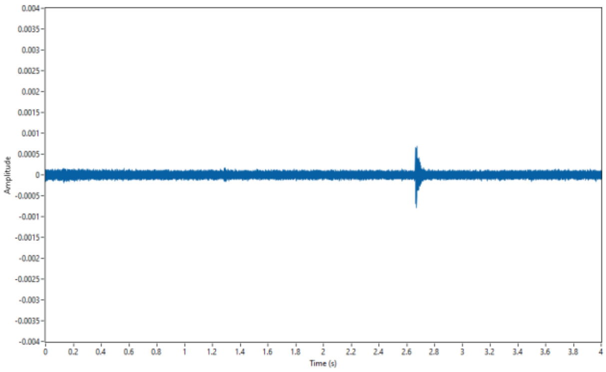

A1.6. Build platform moved down by 1 mm

Filtered FFT of build platform moved down	Filtered STFT of build platform moved down
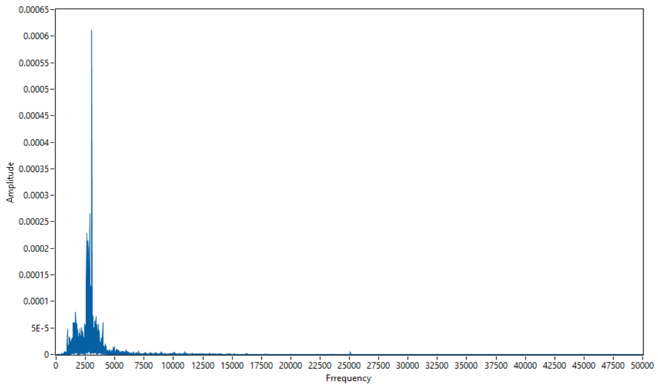	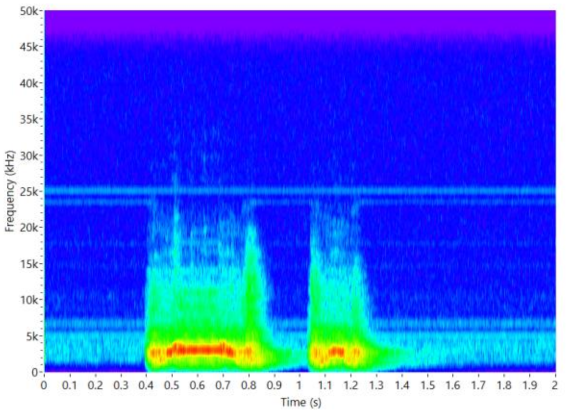
Unfiltered time-domain AE signal of build platform moved down	Filtered time-domain AE signal of build platform moved down
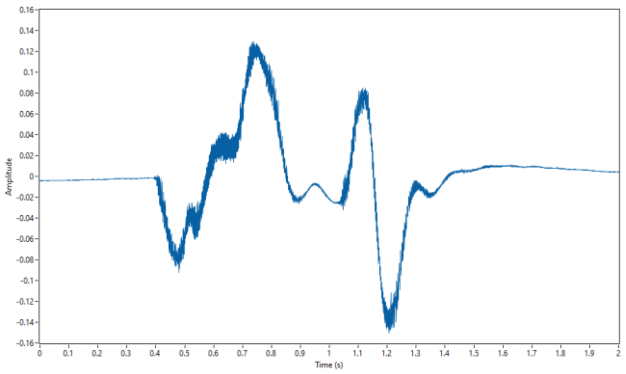	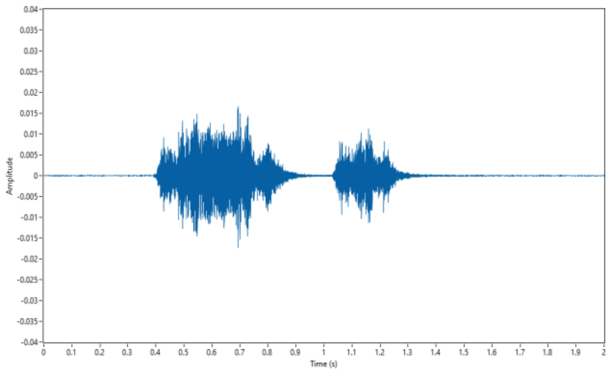

A1.7. Build platform moved up by 1 mm

Filtered FFT of build platform moved up	Filtered STFT of build platform moved up
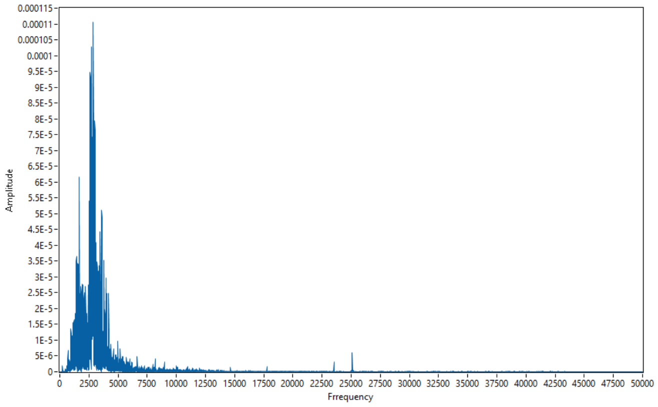	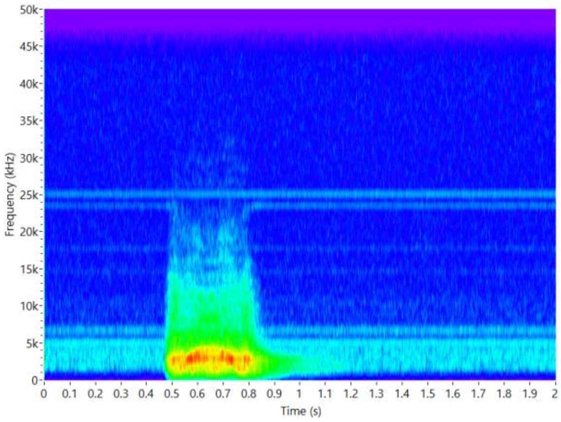
Unfiltered time-domain AE signal of build platform moved up	Filtered time-domain AE signal of build platform moved up
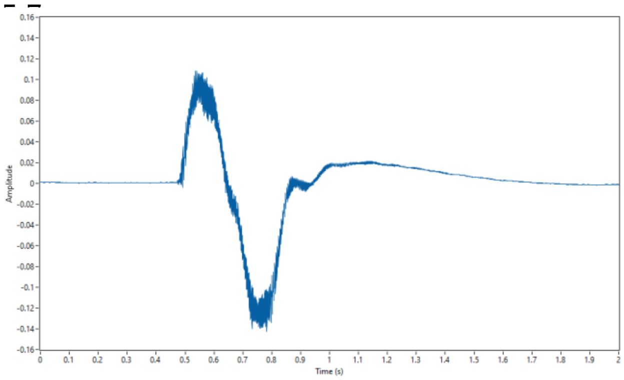	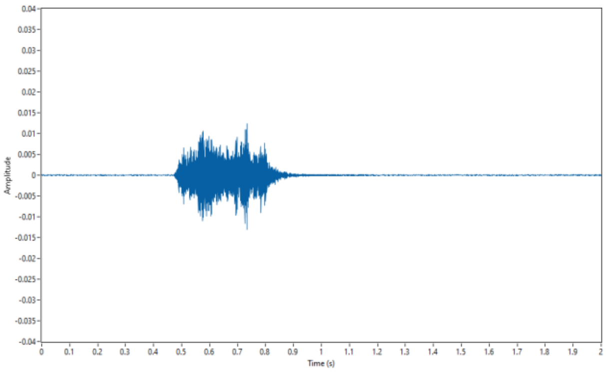

A1.8. Recoater arm moved left

Filtered FFT of recoater moved left	Filtered STFT of recoater moved left
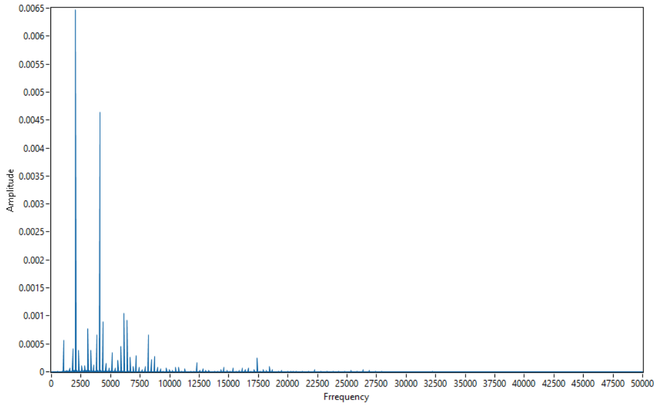	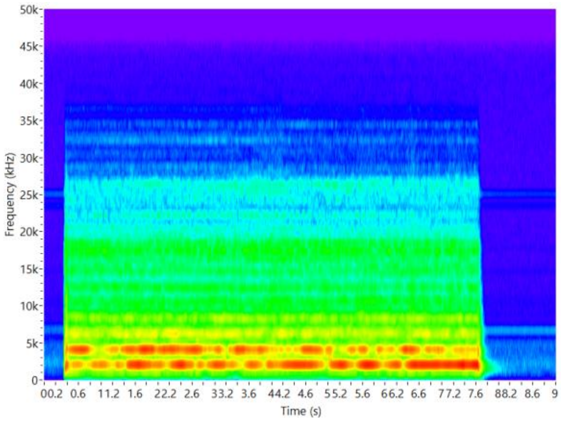
Unfiltered time-domain AE signal of recoater moved left	Filtered time-domain AE signal of recoater moved left
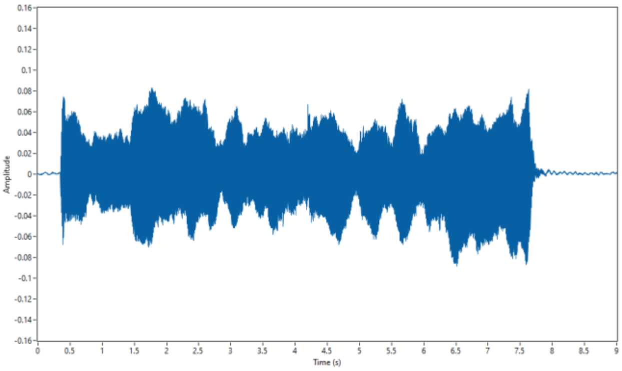	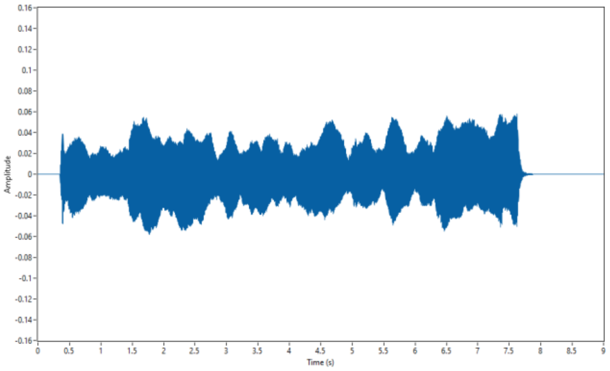

A1.9. Recoater arm moved right

Filtered FFT of recoater moved right	Filtered STFT of recoater moved right
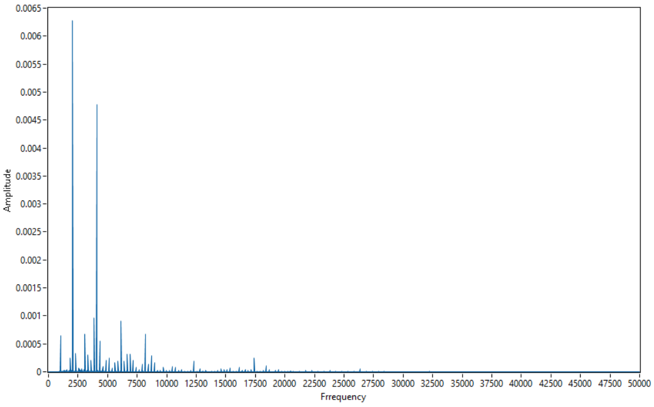	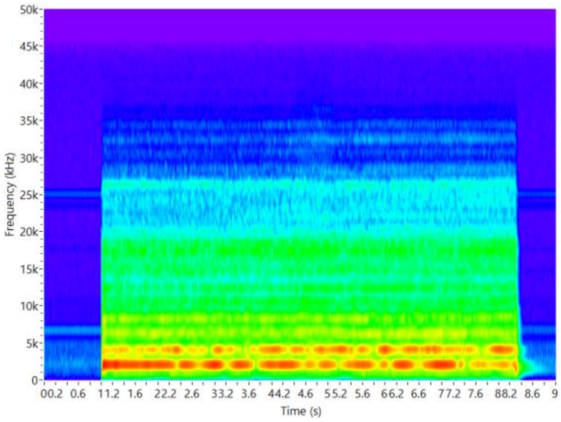
Unfiltered time-domain AE signal of recoater moved right	Filtered time-domain AE signal of recoater moved right
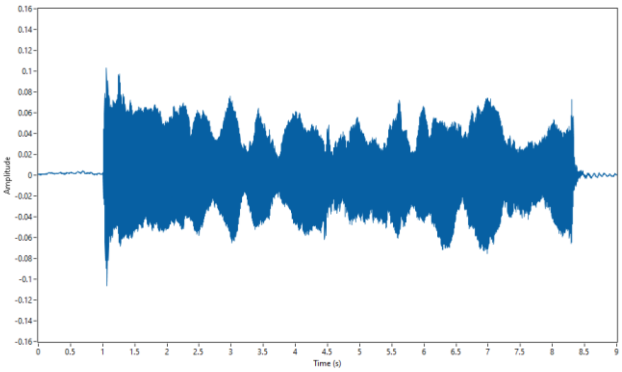	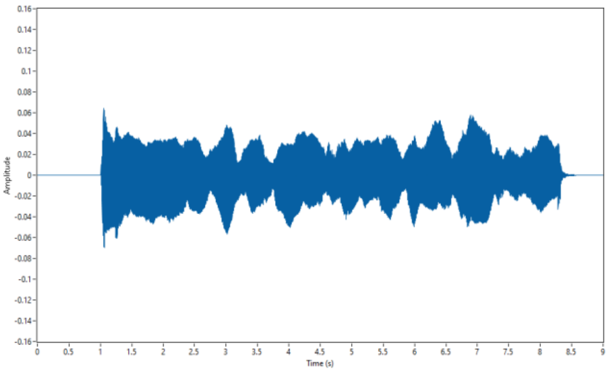

A1.10. Recirculating fan

Filtered FFT of the recirculating fan	Filtered STFT of the recirculating fan
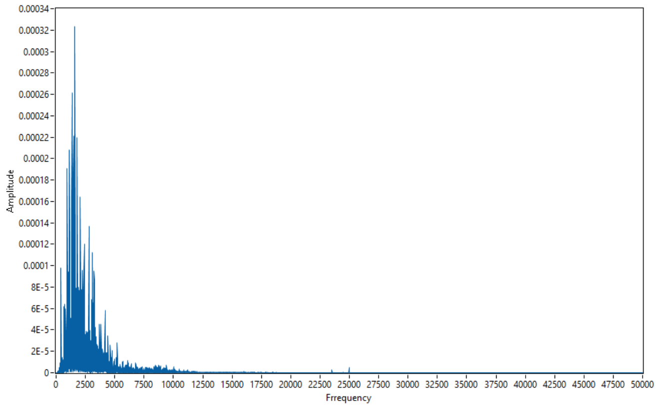	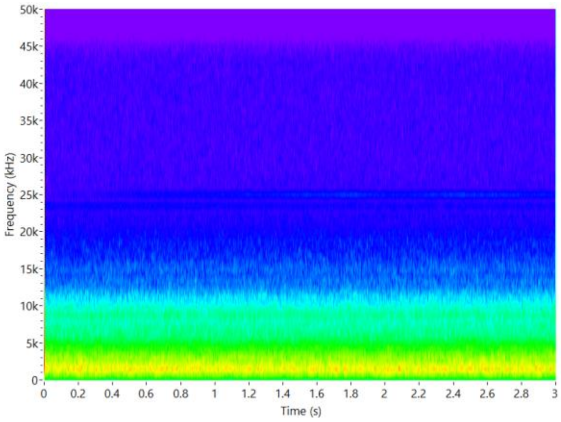
Unfiltered time-domain AE signal of the recirculating fan	Filtered time-domain AE signal of the recirculating fan
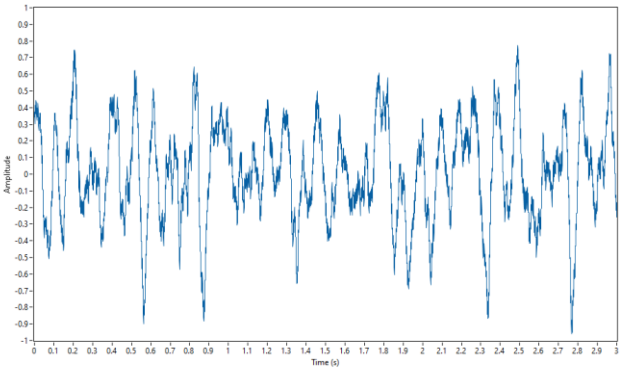	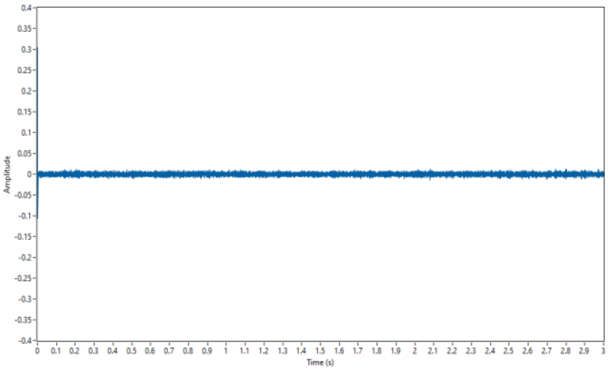

A1.11. Laser scanning

Filtered FFT of the laser scanning	Filtered STFT of the laser scanning
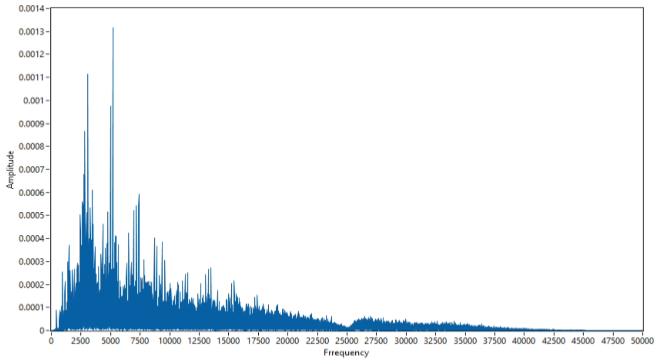	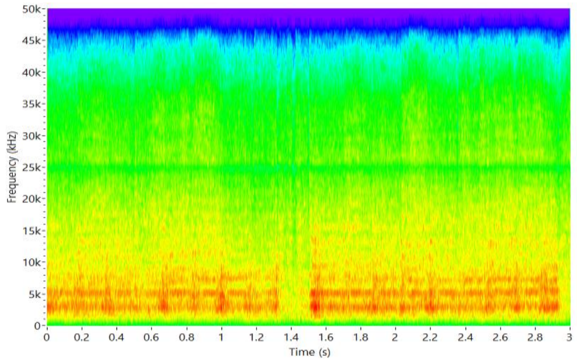
Unfiltered time-domain AE signal of the laser scanning	Filtered time-domain AE signal of the laser scanning
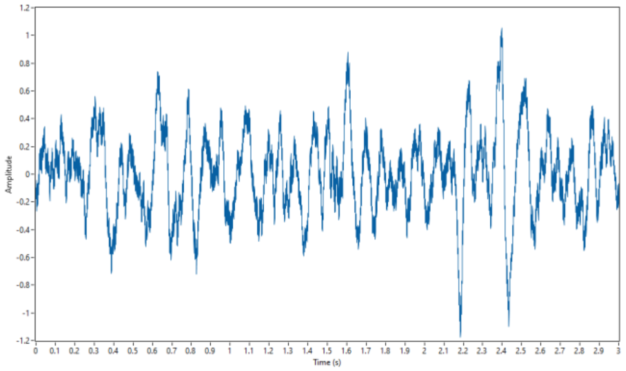	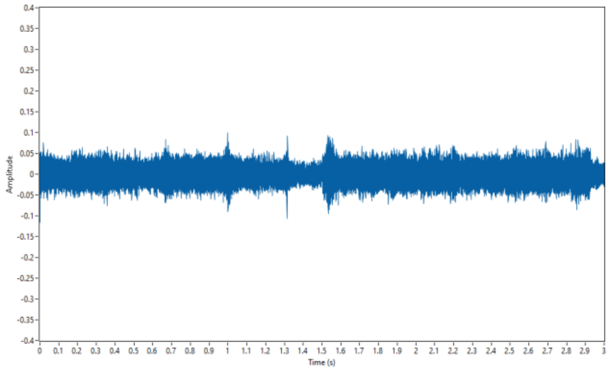

A2. Machine noise AE signals

AE noise signal	RMS of unfiltered noise signal	Peak amplitude of unfiltered noise signal (V)	RMS of filtered noise signal	Peak amplitude of filtered noise signal (V)	Signal-to-noise ratio (dB)
Machine in idle	0.0011	0.0022	0.00003	0.00015	-30.4866
Dispenser moved down by 0.05µm	0.0140	0.0935	0.0005	0.0086	-29.8429
Flooding valve opening	0.028	0.0874	0.00005	0.0012	-55.9176
Build chamber flooding	0.0013	0.0024	0.00005	0.0010	-24.9590
Flooding valve closing	0.0129	0.0202	0.00004	0.0014	-49.6297
Build platform moved down by 1mm	0.0415	0.1296	0.0022	0.0167	-25.4654
Build platform moved up by 1 mm	0.0349	0.1083	0.0012	0.0124	-29.5511
Recoater moved left	0.0221	0.0835	0.0165	0.0578	-2.5289
Recoater moved right	0.0219	0.103	0.0158	0.0646	-2.8124
Recirculating fan	0.2940	0.7762	0.0031	0.3051	-39.1721
Laser scanning	0.2903	1.0535	0.0164	0.0999	-24.9283

A3. Signal-to-noise ratio of cantilever cracks against noise signals (dB)

	Crack-S1-C1	Crack-S1-C2	Crack-S2-C1	Crack-S2-C2	Crack-S3-C1	Crack-S3-C2	Crack-S4-C1
Machine in idle	55.02	63.60	77.55	72.11	56.43	66.29	56.78
Dispenser moved down by 0.05 µm	30.58	39.16	53.11	47.68	32.00	41.85	32.34
Flooding valve opening	50.58	59.16	73.11	67.68	52.00	61.85	52.34
Build chamber flooding	50.58	59.16	73.11	67.68	52.00	61.85	52.34
Flooding valve closing	52.52	61.10	75.05	69.61	53.94	63.79	54.28
Build platform moved down by 1 mm	17.71	26.29	40.25	34.81	19.13	28.99	19.47
Build platform moved up by 1 mm	22.97	31.56	45.51	40.07	24.39	34.25	24.74
Recoater moved left	0.21	8.79	22.74	17.31	1.63	11.48	1.97
Recoater moved right	0.58	9.17	23.12	17.68	2.00	11.86	2.35
Recirculating fan	14.73	23.31	37.27	31.83	16.15	26.01	16.49
Laser scanning	0.26	8.84	22.80	17.36	1.68	11.54	2.02

A4. Peak amplitudes of cantilever cracks AE signals

Noise Signal	Unfiltered crack signal peak amplitude (V)	Filtered crack signal peak amplitude (V)	Decrease in percentage of peak amplitude
Crack-S1-C1	0.627	0.160	74.5%
Crack-S1-C2	0.558	0.399	28.4%
Crack-S2-C1	1.383	1.291	6.7%
Crack-S2-C2	0.927	0.899	2.9%
Crack-S3-C1	0.806	0.157	80.1%
Crack-S3-C2	0.559	0.684	-21.7%
Crack-S4-C1	0.648	0.221	66.1%

A5. Technical drawing of cracking cantilever specimen